FROM SOFT TO HARD SPHERE BEHAVIOR: THE ROLE OF SINGLE PARTICLE ELASTICITY OVER THE PHASE BEHAVIOR OF MICROGEL SUSPENSIONS

A Thesis
Presented to
The Academic Faculty

by

Juan José Liétor-Santos

In Partial Fulfillment
of the Requirements for the Degree
Doctor of Philosophy in the
School of Physics

Georgia Institute of Technology
December 2010

FROM SOFT TO HARD SPHERE BEHAVIOR: THE ROLE OF SINGLE PARTICLE ELASTICITY OVER THE PHASE BEHAVIOR OF MICROGEL SUSPENSIONS

Approved by:

Professor Alberto Fernández-Nieves,
Advisor
School of Physics
Georgia Institute of Technology

Professor Mohan Srinivarao
School of Material Science and
Engineering
Georgia Institute of Technology

Professor L. Andrew Lyon
School of Chemistry
Georgia Institute of Technology

Professor Toan T. Nguyen
School of Physics
Georgia Institute of Technology

Professor Andrew Zangwill
School of Physics
Georgia Institute of Technology

Date Approved: 8 November 2010

ACKNOWLEDGEMENTS

As the end of this period approaches, I am glad to acknowledge those whose indebted help have allowed this to be possible.

First and foremost, I would like to thank my advisor, Alberto Fernandez-Nieves for everything he has done for me in the last 7 years. Since we started in Spain, through Boston and now in Atlanta, my journey has been linked to his and I would not trade it for any other. Day after day, I have had laid in front of me a continuous lesson on how a scientist should behave, in terms of honesty, brilliance, passion and hard working ethic. Having that example to look up to is a privilege that everybody ought to experience once in a lifetime and, thus I cannot be anything other than honored to have had his trust and been by his side all this time.

Words cannot probably begin to describe how thankful I am to Benjamin Sierra-Martin, who has been an enormous influence on this Thesis. With his experience, knowledge, patience and strenuous work, he is an integral part of what this has become. Out of the lab, he has been a loyal friend, both in Spain and then in Atlanta, and his presence has been a continuous incentive to carry on even in the darkest times.

I would also like to thank all the other individuals that are or have been part of the Soft Condensed Matter Lab. Each and everyone of them left their indelible contribution to a better work environment and without any one of them, things would have been certainly different.

Over the course of this Thesis, I have had the pleasure to interact, first over electronic mail and then in person, with Dr. Urs Gasser in Paul Scherrer Institute in Switzerland and I would like to thank him for his help with the Neutron Scattering

part of my work. I hope that this collaboration turns out to be fruitful and continues to be so for a long time.

Also, I would like to thank Prof. Z.B. Hu from University of North Texas for gratefully providing some of the experimental systems used in this work and the members of the committee for critically reading the manuscript and pointing out ways of improvement.

I would like to acknowledge my family. I know this has not been easy for them and I may not have made it any easier but I have always known that I could count on them when needed and I greatly appreciate that.

Finally, we all know that after all, the pyramids were built brick by brick. Although I do not mean to compare this work with a pyramid, I do want to express my sincere thanks to everybody that had or have had anything to do with the work exposed in this Thesis. Irrespective on how big was their help, they all have contributed to make it happen and for that, once again, I thank them.

TABLE OF CONTENTS

LIST OF TABLES

LIST OF FIGURES

SUMMARY

The goal of this thesis is to study the role of single particle elasticity in the overall behavior of particulate systems. For this purpose, we use microgel particles, which are crosslinked polymer networks immersed in a solvent. In these systems, the amount of cross-linker determines their elasticity and ultimately the stiffness of the particle. For a system of hard spheres, the phase behavior is solely determined by the volume fraction occupied by the particles. Based on the volume fraction, liquid, crystal and glassy phases are observed. Interestingly, microgel particles display a richer and fascinating set of different behaviors depending on the particle stiffness. Previous results obtained in our group show that for highly cross-linked microgels, the glass phase disappears and there are only liquid and crystalline phases. By contrast, preliminary measurements indicate that for ultrasoft microgel particles the system does not show any signature of crystalline or glassy phases. The system seems to remain liquid irrespective of volume fractions. In this Thesis, we will address this striking result using light scattering as well as rheology, in order to access both static and dynamic properties in a wide range of length and time scales. In addition, we will also perform additional studies using very stiff microgels and use their swelling capabilities to change the volume fraction. We will use hydrostatic pressure to change the miscibility of the polymer network and thus change the microgel size; the use of this external variable allows fast equilibration times and homogeneous changes throughout the sample. By using neutron scattering techniques, we study the structural and dynamical properties of the system in its different phases involved.

CHAPTER I

INTRODUCTION

Soft materials comprise a wealth of different states and mixtures whose physical behavior cannot be directly inferred from their atomic or molecular components [1]. Their characteristic length scales are larger than the atom size and typically result in a low elastic modulus. An example of a soft material is commercial shaving cream. It is formed by trapping a gas into a liquid. While none of these components are solid, the mixture exhibits solid behavior: it has a specific shape and responds elastically to an applied stress. Additionally, it can also be permanently deformed if the applied force is above certain threshold. Soft materials can thus exhibit typical behavior of both solids and liquids.

Many of these materials are present in every aspect of our life. In fact, they even are fundamental systems in the sustain of life itself since our blood is a colloidal suspension of red and white blood cells in a sea of water enriched with proteins and other components, which is another example of a soft material. Commercially, they are widely used for paintings and coatings [2], controlled drug-release [3], food and cosmetic industry [4, 5] and water purification [6].

Many soft materials are particulate systems composed of large solute particles and a continuous phase. This size asymmetry between constituents clearly differentiates such materials from chemical mixtures, which are mainly composed by species having similar characteristic sizes.

Among all soft materials, colloidal suspensions are particularly useful model systems with which scientists have tackled profound questions in condensed matter physics. They are formed by a liquid continuous phase and a solid dispersed phase.

Milk, for instance, is an example of a colloidal suspensions where the fatty acids and micelles are dispersed in an aqueous media enriched with minerals and hydrocarbons.

Colloids are widely used in basic and applied science because of the possibilities for tuning their shapes and superficial properties [7]. Irrespective of the details of the solute, colloidal systems are characterized by experiencing Brownian motion. At any given instant, each of the solid particles is subjected to elastic collisions with the molecules of the solvent. Since the number of collisions is not even throughout the particle surface, the colloidal particle exhibits a net displacement that is random in time; the particle jiggles around a certain position inducing macroscopic uniformity since all the inhomogeneities in the sample are diffused away in time. This phenomenon was first noticed by the Romans when observing dust in air and was brought forward as one of the proofs of the Democritus atomistic theory of matter [8]. However, the first systematic study of this random motion was reported by Robert Brown in 1827 when observing pollen grains in water solution [9]. In 1905, independently Einstein [10] and Smoluchowski [11] brought this problem to the general physics audience and used it as a definite proof of the existence of atoms.

Energetically, the diffusion of particles in a solvent is on the order of $k_b\,T$, with k_b the Boltzman constant and T the temperature; increasing the temperature increases the average velocity of the solvent molecules and, ultimately, the probability for collision. At room temperature, T=298K, $E_{thermal} \approx 4 \cdot 10^{-21}$J. In contrast, the gravitational energy to lift a 200nm polystyrene particle ($\rho = 1050$ kg/m^3) immersed in water ($\rho_w = 1000$ kg/m^3) its own size is $E_{grav} = m\,g\,h = \frac{4}{3}\pi\Delta\rho g a^4 \approx 6 \cdot 10^{-24} J$. Thus, clearly $E_{thermal} >> E_{grav}$ for colloidal particles. As the particle size increases, the gravitational term becomes increasingly dominant, due to the a^4 dependence, eventually entering into the granular limit [12, 13]. Therefore, we can conclude that the dynamics of colloidal systems is mainly dominated by diffusion. This feature has important consequences in their behavior since it allows the system to effectively

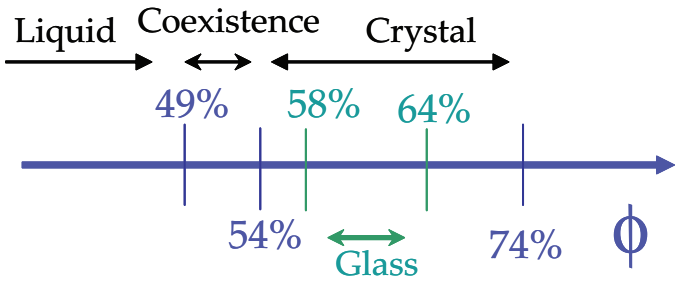

Figure 1: Phase diagram for a system of hard spheres.

explore phase space and, in some cases, self-organize into mesoscopic structures. One example of this are opals, which are regular lattice packings of silica spheres with sizes ranging from 100nm to 400 nm. The quality of the opal is determined by the distribution of different lattice distances and different particle sizes within one opal. Since the lattice constant of opals and, in general, of any colloidal crystals is comparable to visible wavelengths, they Bragg-diffract light as atomic crystals Bragg-diffract x-rays.

The analogy between atomic and colloidal systems can be further extended by establishing an analogy between the interatomic and interparticle potential. As a result, colloidal particles can be used as models for studying atomic systems. However, whereas single atoms are *hard* to observe, the size -on the order of four orders of magnitude larger- and dynamics -around 8 orders of magnitude smaller- of colloidal particles allows direct measurements with optical microscopy. This has been extensively exploited to elucidate the formation, growth and structure of crystalline phases [14, 15], to study of defects [16, 17], to gain insight on the liquid-glass transition [18, 19, 20] and, more generally, to study phase transitions [21, 22, 23].

Among colloidal systems, those based on hard spheres are the simplest [24]. The interactions are spherically symmetric, non-existent for particle-particle distances larger than the particle diameter and are effectively infinity for distances smaller than the particle diameter. In spite of their inherent simplicity, hard sphere systems display a rich phase and non-equilibrium behavior, as shown in Fig.1.

Very much like atomic systems with decreasing temperature, hard spheres have fluid, crystalline and glassy phases with increasing the volume fraction, $\phi = \frac{N}{V} V_{1p}$, with N the number of particles, V the total accessible volume and V_{1p} the volume of an individual particle. At low volume fractions, the system behaves essentially as a non-interacting gas with no structural features. As ϕ increases, the system behaves as a liquid showing local-order correlations. This extends up to $\phi = 0.495$, where a phase coexistence between a crystalline phase and a liquid phase appears. At $\phi = 0.545$, the system becomes fully crystalline and, as the volume fraction is further increased, the crystallites becomes increasingly compact up to $\phi = 0.74$, which represents the maximum sphere packing [22]. All these different phases are equilibrium configurations and thus, minimum states of the free energy of the system. However, the system can become kinetically trapped in local minima and exhibit non-equilibrium phases. In fact, hard spheres exhibit a glass phase from $\phi = 0.58$ to $\phi = 0.64$, which correspond to random close packing [25].

Relaxing some of the conditions of the hard sphere model gives rise to a fascinating range of different behaviors. For instance, if the particles are rods, the system can exhibit isotropic, liquid crystal and crystal phases depending on the particle density and the aspect ratio of the cylinders [26]. The presence of charge in the surface of the particles can give rise to electrostatic interactions between particles of either repulsive [27] or attractive nature [28], which can induce the formation of structures like the LS_8 with no counterpart in atomic systems [29]. There are other types of interaction that are not related to electrostatic interactions like deplexion, which has an entropic origin and results from the presence of species smaller than the colloidal particles but larger than the solvent molecules. These create an osmotic pressure that is balanced everywhere around the colloidal particles. However, when the particles approach to a distance smaller than the average size of the depletants, the osmotic pressure cannot be balanced and thus, an attractive interaction is induced. Depending on the volume

fraction of colloidal particles, the size ratio between those and the depletants and their concentration, this attraction can result in the formation of a liquid phase, in formation of solid phases [30, 31] and can drive gas-liquid spinodal phase separation [32].

Microgel particles are a particular class of colloid. They are cross-linked polymer networks immersed in a fluid. As their macroscopic counterparts, they experience reversible changes in volume triggered by changes in properties such as temperature, pH, electromagnetic radiation, solvent composition, ionic concentration or the presence of a non-negligible amount of polymer or surfactants. However, they do so in a considerably shorter timescale [33, 34], a fact that has been extensively exploited in several technological applications [35, 36, 37], including drug delivery [38, 39], water purification technologies [40], artificial muscle fabrication [41], optical switching [42, 43], microfluidic devices [44] and oil recovery [45, 46]. Thermodynamically, their swelling equilibrium can be described by considering a balance between the osmotic pressure arising from the miscibility of the polymer and the solvent and an elastic osmotic pressure that is dependent on the number of chains within the network [47]. The presence of non-adsorbing polymer [48, 49] or of fixed charge on the polymer [50] also contributes to the net osmotic pressure, thus, influencing the swelling behavior of the system.

Microgel suspensions have been observed to behave as hard spheres in many circumstances. Their swelling behavior has thus been used as an elegant way to tune the colloidal volume fraction without changing the particle concentration. By exploiting this possibility, they have been used to address fundamental questions related to phase transitions [51, 52, 53, 54, 55, 56]. Interestingly, there are several experimental and numerical studies that suggest that microgel suspensions can have a richer behavior than colloidal hard spheres. For instance, it has been recently shown that microgel

suspensions show self-healing behavior [57]. Colloidal crystals made of microgel particles are able to deswell larger alien microgels due to the osmotic pressure induced by the crystalline structure accommodating the deswollen particles into the crystal. Similarly, ionic microgels sensitive to pH have been shown to progressively differ from hard sphere behavior as the microgel network increasingly charges; the crystal phase range becomes shifted to higher volume fractions and progressively shrinks, eventually disappearing and giving rise to a liquid-glass transition [55]. Also, theoretical predictions seem to show that for weakly cross-linked ionic microgels the phase behavior is markedly different from that of hard spheres; for low charge the crystal phase disappears and, as the particle charge is increased, crystalline phases different from the usual BCC and FCC observed for hard spheres appear [58, 59]. The key to this richness may result from the unique properties of microgel particles, which are compressible and deformable [53]. Qualitatively, for volume fractions larger than 0.64, in the absence of crystallization, the particles will touch with each other and deform, a behavior reminiscent of compressed emulsions [60, 61]. However, the ability of microgels to interpenetrate and compress allows the achievement of higher volume fractions. We quantify this using a generalized volume fraction, $\zeta = nV_0$, with n the particle density and V_0 the volume of the particle in the dilute state. By definition, ζ can take values higher than 1 since the particles can compress and interpenetrate after filling space. We emphasize that for low particle concentrations, ζ is equal to the suspension volume fraction.

In this Thesis we will focus on how the single particle elasticity affects the phase behavior of colloidal particles. We will try to elucidate whether the stiffness of the individual entities that form a colloidal system has any influence in the overall, macroscopic behavior of the suspension. In order to carry out this investigation, we will use microgels as model deformable particles.

In Chapter 2, we study the behavior of weakly crosslinked microgels using rheology and light scattering. Surprisingly, when the particles are swollen, the system only shows liquid-like phases at all the experimentally available ζ, in marked contrast with the behavior of hard spheres. Moreover, the viscosity of the suspension increases exponentially with ζ, a behavior which is reminiscent of how some molecular glasses approach their glass transition. We also observe that the structural relaxation time, which we determine using oscillatory rheology and dynamic light scattering, follows the same trend with ζ. Our interpretation of this similarity is based on considering that the local elasticity of the system remains constant as ζ increases and that this local elasticity is the ultimate responsible governing the relaxation and the flow behavior of the material. We show that the interpenetration of the polyelectrolyte chains at the periphery of the particles plays a crucial role in this behavior.

In Chapter 3, we will address whether particle shrinking can take place before $\zeta = 1$, as it is sometimes claimed in the literature. Since deswelling can only happen if the bulk modulus of the particle becomes comparable to the osmotic pressure of the suspension, we independently measure the osmotic pressure of a microgel suspension as a function of ζ and the individual particle bulk modulus. Our results suggest that only when $\zeta \approx 1$, these two quantities match.

In Chapter 4, we will explore the effects of a previously unexplored variable, hydrostatic pressure, to induce deswelling of microgel particles. We find that the effects of pressure are similar to the effects of temperature and by comparing both we are able to determine the dependence of the solvency parameter with hydrostatic pressure for the first time for the case of microgel particles. It increases with hydrostatic pressure, consistent with particle deswelling and with the temperature behavior. Despite this, the changes in particle size are smoother when achieved with hydrostatic pressure as compared to temperature.

In Chapter 5, we will study the phase behavior of stiffer microgels using Small

Angle Neutron Scattering (SANS). The scattered intensity depends on the particularities of the individual particle, through the form factor, and on the correlations between different particles through the structure factor. We thus determine the form factor of the microgel particles at different temperatures and hydrostatic pressures using SANS in dilute solutions and use a core-shell model to describe our results. By visual inspection, we determine the ζ ranges corresponding to liquid, crystal and glassy phases and find they are close to the corresponding boundaries in hard sphere suspensions. For crystal samples, we measure the scattered intensity, normalize it with the particle form factor and fit the resulting structure factor to several lattice models. We are able to describe the results but unable to elucidate the crystal structure. We also study the nucleation and growth of the crystals as well as their behavior under the influence of hydrostatic pressure. For glassy samples, we find unexpected structure factors when compared to those of corresponding hard sphere suspensions. We interpret this dissimilarity eluding to polydispersity changes mediated by particle softness and fit the data by incorporating, somehow, this idea into the model. Despite only moderate agreement is obtained, the results and the analysis suggest that the softness of the particle could affect the suspension polydispersity to allow the system to exhibit a phase behavior that is reminiscent of hard sphere suspensions.

CHAPTER II

ARRHENIUS BEHAVIOR OF WEAKLY CROSSLINKED MICROGELS

2.1 Introduction

Colloidal systems have been extensively used to study fundamental problems [14, 15, 16, 17, 18, 19] based on their size and time scales; they are large and slow and thus easy to visualize and follow. One of these problems is the glass transition [18, 19, 20, 62, 63, 64]. It is experimentally found that the viscosity and the structural relaxation time of a colloidal suspensions slowly increases for low volume fractions, ϕ. By contrast, when ϕ increases above $\phi \approx 0.53$, the viscosity starts to increase significantly to eventually diverge at $\phi_g = 0.58$. At this volume fraction, the large number of particles in the system greatly restricts their motion with the consequent increase in the structural relaxation time. The system becomes kinetically arrested in what is usually called the *glass state*.

An analogous phenomenon is observed in supercooled liquids in terms of the inverse temperature [65]. As 1/T increases, the structural relaxation time appreciable increases on the approach of the glass transition temperature. Interestingly, this approach can vary greatly depending on the glass former, as shown in Fig.2a, where we show the dependence of the structural relaxation time with the inverse temperature normalized by the inverse glass transition temperature, which is defined here as the temperature for which $< \tau >= 100$s [66].

For some glass formers, the structural relaxation time follows an Arrhenius behavior:

$$< \tau > \sim e^{E_a/T} \tag{1}$$

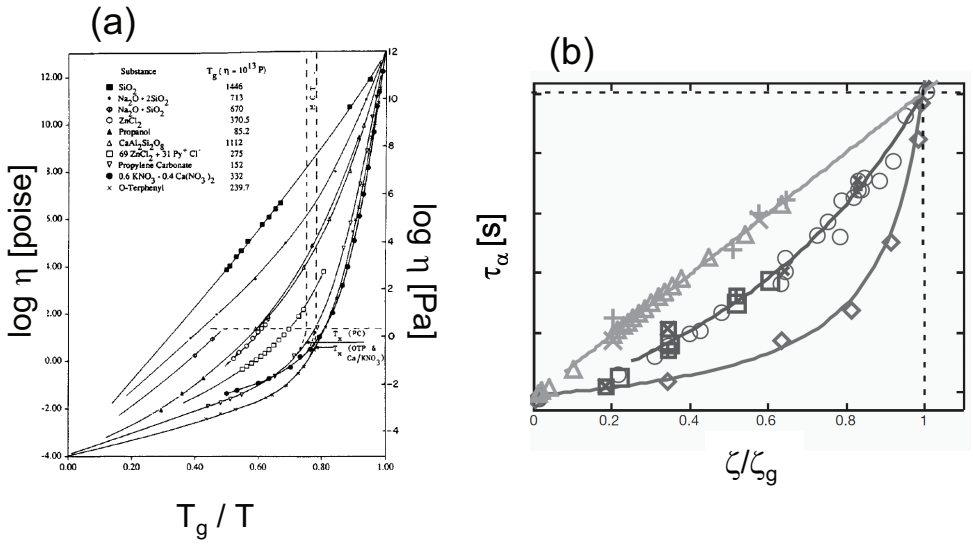

Figure 2: a) Normalized relaxation time versus normalized inverse temperature for different molecular glass-formers. Taken from [66]; b) Analogous plot for colloidal systems of different stiffness: ($\Diamond$) Hard Spheres, ($\circ$, $\Box$) Intermediate, ($\triangle$,+) Strong. The role of the inverse temperature is played by the system volume fraction, ζ. Taken from [20]

with E_a an activation energy. An example of a strong molecular glass-former is silica. By contrast, other glass formers exhibit variations from an Arrhenius behavior. These deviations are described by the so-called fragility, m, defined as the slope of the $\log < \tau >$ versus (T_g/T) plot in the neighborhood of T_g [66]:

$$m = \frac{d \log < \tau >}{d(T_g/T)}|_{T=T_g} \tag{2}$$

Molecular glass formers approaching the glass in an Arrhenius fashion are called strong glass formers, while molecular glass formers with a more abrupt approach to the glass are called fragile. Following this classification, hard spheres are fragile [18, 20, 62, 67] since they become a glass in a very narrow range of volume fractions. Systems with van der Waals, spherically symmetric interactions like $ZnCl_2$ or propanol are fragile also as shown in Fig.2a.

Colloids usually only exhibit fragile behavior, as shown in Fig.2b, where we plot

the structural relaxation time, τ_α, versus ζ/ζ_g, with ζ_g is defined by analogy to molecular glass formers, as the volume fraction for which $\tau_\alpha = 100$s.

Recently, the approach to the glass has been studied using microgel suspensions. Microgels display common features with hard-sphere systems; at low volume fractions they are liquid, while at high volume fractions they can exhibit crystal [51, 54, 68] and glassy phases [52, 53, 69, 70]. However, their phase behavior is greatly influenced by their deformability: the particle volume and shape can change as the system is concentrated. This allows, for instance, to concentrate the system above $\phi_{rcp} = 0.64$. This is achieved at the expense of deforming and shrinking the particles due to steric constraints resulting from the presence of their neighbors.

Their softness enables colloidal suspensions to mimic the fragility spectrum of molecular glassformers. As the particles become softer, the suspension becomes *stronger*, as shown in Fig.2b with microgels with an intermediate stiffness (circles and squares) and with soft microgels (triangles and crosses). In fact, for the softer microgels the structural relaxation time becomes exponential with ζ, reminiscent of the Arrhenius behavior of strong glass formers:

$$\tau_\alpha \sim e^{C\zeta} \tag{3}$$

with C a constant. Despite this remarkable analogy between colloids and molecular glass formers, the physical origin of fragility is still unclear [71]. In this chapter, we will address this question by studying ultrasoft microgels using light scattering and rheology. We will start the chapter by reviewing the fundamental theory behind the experimental techniques that we use. Since the samples will be highly concentrated, we will have to deal with multiple scattering which tampers the classical interpretation of dynamic light scattering data. In order to overcome this limitation, we use cross-correlation techniques that allow us to extract the single scattering information from multiply scattering samples. The microgels we use are based on a weakly-crosslinked network of 2-vinylpyridine, a polymer that ionizes with pH. At high pH, the particles

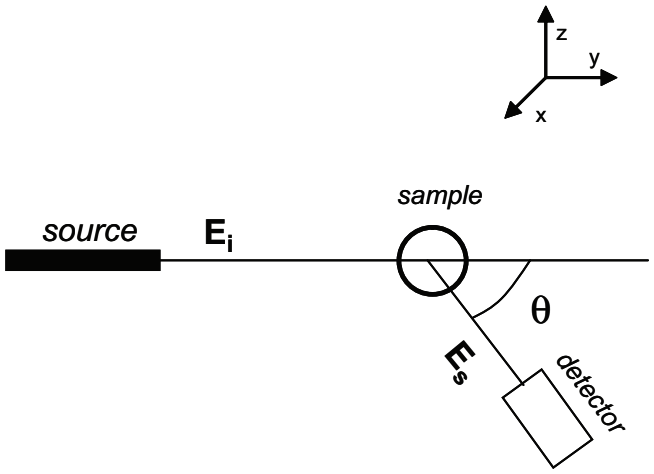

Figure 3: Sketch of a typical light scattering experiment layout.

are deswollen and the system behaves essentially as a system of hard-spheres with liquid and crystal phases. By contrast, at low pH, the particles are swollen and the crystal phase is never reached irrespective of ζ. The system only displays disordered phases. Surprisingly, the system never reaches the glass state either, always remaining liquid-like. Interestingly, the viscosity of the system as a function of ζ follows an Arrhenius behavior. Moreover, over the same range of ζ, we observe an identical behavior of the structural relaxation time, which we determine independently using dynamic light scattering. By correlating these results we conclude that the local elasticity of the system remains constant with ζ enabling a *strong* approach to the glass. We show that the interpenetration of the polymer, in the periphery of the particles is essential for this behavior, emphasizing that it is this side of the softness which ultimately enables the system to be a strong glass former.

2.2 Experimental Techniques

2.2.1 Light Scattering

Fundamentally, any scattering experiment consists of an incident radiation beam, a sample and a detector [72, 73]. Radiation is scattered by the microscopic components of the sample and the resultant intensity is collected in a detector at an scattering

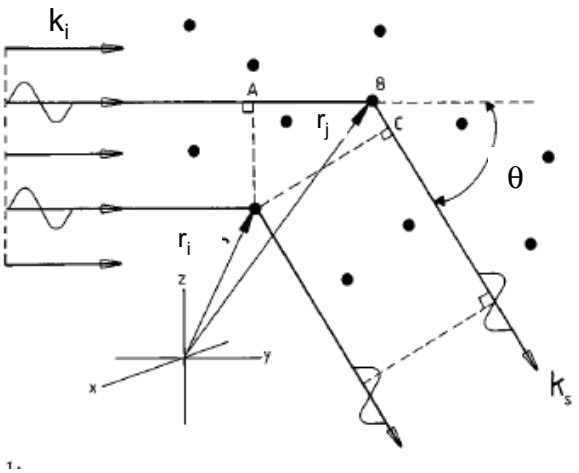

Figure 4: Schematic representation of an scattering experiment by a collection of scatterers. Taken from [72]

angle, θ, defined as the angle between the incident and the scattered beams, as shown in Fig.3.

Consider a monochromatic beam impinging on a collection of scatterers (Fig.4). The total electric field in any position will be the sum of the scattered electric fields resulting from the interaction with each of the scatterers. It is easy to see that the phase difference between these electric fields at any point will be determined by the relative position of the scatterers in space and the position of the detector resulting in certain interference pattern. If the scatterers change location, this interference pattern will change. These changes are closely related to the dynamics of the scatterers. This is only true if the wavelength of the radiation is on the order of the distance between the scatterers. In any other case, changes in position would not significantly alter the interference condition. Let us suppose that an electromagnetic wave is vertically polarized along x and impinges on a spherical scatterer in position $\mathbf{r_i}$. The incident electric field can be written as:

$$\vec{E}(\vec{r},t) = \vec{E}_0 e^{i(\vec{k}_i \cdot \vec{r}_i - \omega t)} \tag{4}$$

with $\mathbf{E}_0$ the amplitude of the electric field, ω the angular frequency and $\mathbf{k}$ the wave vector of the radiation.

The response of the scatterer to this wave is the polarization of its charge distribution. As a result, a dipole moment, $\mathbf{p}_s$, is induced. $\mathbf{p}_s$ is proportional to the incident electric field through the polarizability of the particle, α:

$$\vec{p_s} = \alpha \vec{E} \tag{5}$$

It is important to note that α is, in general, a second-rank tensor. However, in the special case of scatterers whose size is much more smaller than the wavelength of the incident light, the polarizability is a scalar and the scattering is isotropic. This situation corresponds to the so called Rayleigh regime [73].

The oscillation of the dipole causes emission of radiation, with an electric field that is proportional to the acceleration of the charges, $\frac{d^2 p_s}{d^2 t}$, and inversely proportional to the distance to the detector, $\sim 1/r$. Therefore, the scattered field in a time, t, on the yz plane (Fig.4) is:

$$E_s = \frac{1}{4\pi\epsilon_0 c_l^2}\frac{1}{r}\left(\frac{d^2 p_s}{d^2 t}\right)_{t'=t-r/c_l} \tag{6}$$

with $c_l = \frac{\omega}{|k|}$ the group velocity of the emitted radiation and t' the retardation time, which accounts for the fact that the scattered radiation takes a time $\frac{r}{c_l}$ to reach the detector at a distance r away from the origin. Using Eq.4, we obtain :

$$\vec{E}_s = \frac{\pi}{\lambda^2 \epsilon_0 r}\alpha \vec{E}_0 e^{i(\vec{k}_i\cdot(\vec{r}-\vec{r}_i)-\omega(t-|\vec{r}-\vec{r}_i|/c_l))} \tag{7}$$

To obtain the scattered intensity, we take the squared-average of the scattered electric field:

$$I_1 = < \vec{E}_s^*(\vec{r},t)\vec{E}_s(\vec{r},t) > = I_0 \frac{\pi^2\alpha^2}{\lambda^4 \epsilon_0^2 r^2} \tag{8}$$

with $I_0 = |E_o|^2$ the mean incident intensity. Note that shorter wavelengths are scattered more strongly than larger wavelengths [74].

If we have two scatterers in the system, i and j, the total scattered electric field that arrives at the detector is a superposition of both:

$$\vec{E}_s = \vec{E}_i + \vec{E}_j = \vec{E}_i(1 + e^{i\Phi_{ij}}) \tag{9}$$

where $\mathbf{E_i}$ is the scattered field from scatterer i and $\Phi_{ij} = \mathbf{k_i} \cdot (\mathbf{r_i} - \mathbf{r_j}) - \omega(\mathbf{t_i} - \mathbf{t_j})$ is the phase difference between $\mathbf{E}_i$ and $\mathbf{E}_j$. The difference $(t_i - t_j)$ can be written as l_{ij}/c_l, with $l_{ij} = |\mathbf{r_i} - \mathbf{r_j}|$. Recalling the definition of c_l, we can rewrite the phase difference as:

$$\Phi_{ij} = \vec{k_i} \cdot (\vec{r_i} - \vec{r_j}) - \vec{k_s} \cdot (\vec{r_i} - \vec{r_j}) = -\vec{q} \cdot (\vec{r_i} - \vec{r_j}) \tag{10}$$

with $\mathbf{q} = \mathbf{k_s} - \mathbf{k_i}$ the scattering wave vector. Note that the phase difference between both waves is a consequence of the difference in optical path that $\mathbf{E}_i$ and $\mathbf{E}_j$ have to travel. For elastic scattering, $|\mathbf{k_s}| = |\mathbf{k_i}|$, and thus:

$$|\vec{q}| = \frac{4\pi}{\lambda} \sin(\Theta/2) \tag{11}$$

The structures that can be resolved in an scattering experiment must have a length scale of order *1/q*. For visible light, λ is of the order of the characteristic length scale of many soft materials; this is why light scattering is so useful for studying this class of systems. If the characteristic length-scales are somewhat smaller, the scattering wave vector needs to be larger; this is usually achieved by changing the wavelength of the radiation using x-rays or neutrons.

Expression 9 can be generalized for N scatterers by summing over all of them:

$$\vec{E_s} = \vec{E_i} \sum_{j=1}^{N} e^{i\Phi_{ij}} \tag{12}$$

Note that $\mathbf{E}_s$ can be viewed as the electric field scattered by one particle corrected by a factor $\sum_{j=1}^{N} e^{i\Phi_{ij}}$. The total intensity is:

$$I = I_1 \sum_{j=1}^{N} e^{i\Phi_{1j}} \sum_{k=1}^{N} e^{-i\Phi_{1k}} \tag{13}$$

By combining the summation and using Eq.8, we obtain:

$$I = I_0 \frac{\pi^2 \alpha^2}{\lambda^4 \epsilon_0^2 r^2} \sum_{j,k=1}^{N} e^{-i\Phi_{kj}} \tag{14}$$

If the scatterers are immersed in a solvent of dielectric permittivity $\epsilon\epsilon_0$ and index of refraction $n = \sqrt{\epsilon}$, the wavelength of the radiation becomes λ/n and the polarizability must be substituted by an excess polarizability, α_{ex}, which is calculated as the difference between the polarizability of the scatterers and that of the solvent. α_{ex} contains contributions from fluctuations in the position of the scatterers and fluctuation in the concentrations of scatterers. These are related to the change in the local index of refraction, $\Delta n(\mathbf{r})$, by the Clausius-Mossoti equation [76]:

$$d\alpha_{ex}(\vec{r}) = 2\epsilon_0 \Delta n(\vec{r}) d\vec{r} \tag{15}$$

As a result, different parts of the sample will scatter differently. Following the same procedure as before, we can write the total scattered intensity, I_{ex}, as:

$$\begin{aligned} \frac{I_{ex}}{I_0} &= \frac{\pi^2}{\lambda^4 r^2} \int_V \frac{d\alpha_{ex}(\vec{r}_1)}{\epsilon_0} \int_V \frac{d\alpha_{ex}(\vec{r}_2)}{\epsilon_0} e^{-i\vec{q}\cdot(\vec{r}_1-\vec{r}_2)} d\vec{r}_1 d\vec{r}_2 = \\ &= \frac{4\pi^2 n^2}{\lambda^4 r^2} \int_V d\vec{r}_1 \int_V d\vec{r}_2 \Delta_c n(\vec{r}_1) \Delta_c n(\vec{r}_2) e^{-i\vec{q}\cdot(\vec{r}_1-\vec{r}_2)} \end{aligned} \tag{16}$$

with $\Delta_c n(\mathbf{r})$ the fluctuations in the index of refraction caused by local fluctuations in the particle concentration. $\Delta_c n(\mathbf{r})$ can be easily related to concentrations fluctuations [77]:

$$\Delta_c n(\vec{r}) = \frac{dn}{dc} \Delta c(\vec{r}) \tag{17}$$

which allows Eq.16 to be rewritten as:

$$\frac{I_{ex}}{I_0} = \frac{4\pi^2 n^2}{\lambda^4 r^2} (\frac{dn}{dc})^2 f(\vec{q}) \tag{18}$$

where $f(\mathbf{q})$ is the Fourier transform of the correlation function associated to concentration fluctuations, $< \Delta c(\mathbf{r_1}) \mathbf{\Delta c}(\mathbf{r_2}) >$:

$$f(\vec{q}) = \int_V d\vec{r}_1 \int_V d\vec{r}_2 < \Delta c(\vec{r}_1) \Delta c(\vec{r}_2) > e^{-i\vec{q}\cdot(\vec{r}_1-\vec{r}_2)} \tag{19}$$

Note that for:

$$\vec{q} \to 0, f(\vec{q}=0) = V^2 (\Delta c)^2 = \sigma_N^2 \tag{20}$$

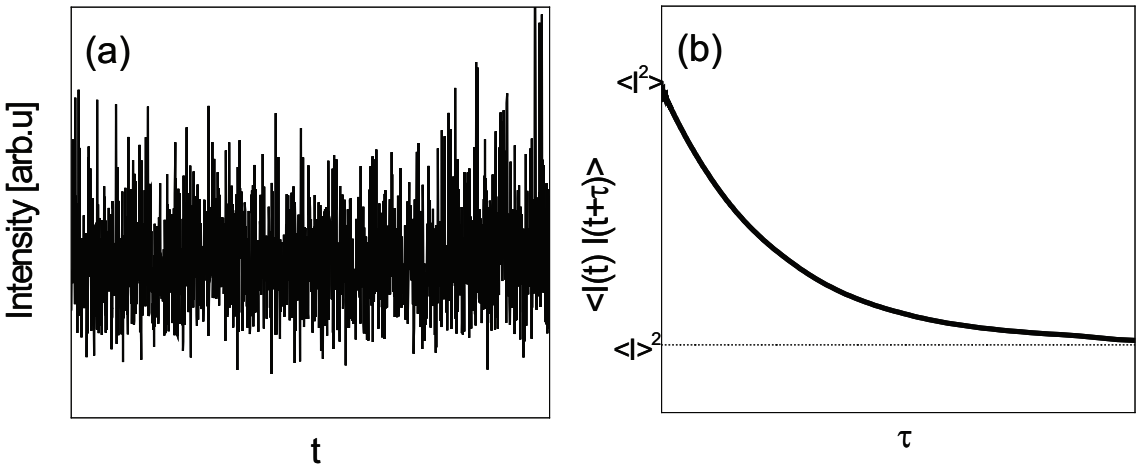

Figure 5: a) Detected intensity as a function of time. The fluctuations are the consequence of the scatterers motion; b) Intensity correlation function as a function of the correlation time.

with $\sigma_N^2 =< N_p^2 > - < N_p >^2$ the fluctuation in the number of particles, which is related to the compressibility of the system, κ_T, as [78]:

$$\sigma_N^2 = k_b T \frac{< N_p >^2}{V} \kappa_T \tag{21}$$

This equation relates a magnitude obtained in an scattering experiment, $f(\mathbf{q})$, to a thermodynamic quantity, κ_T.

The most important feature of Eq.16 or Eq.18 is that it clearly shows that scattering comes from local fluctuations in the index of refraction caused by local particle concentration fluctuations. Particles suspended in a liquid are subjected to Brownian motion. Therefore, the configuration and the amount of particles in the scattering volume change in time. This is manifested in fluctuations in the intensity with time, as shown in Fig.5a for a particular sample.

Since the origin of these fluctuations is related to the dynamics of the scatterers, the correlation function of the signal serves to quantify the dynamics of the sample. Experimentally, we measure the intensity correlation function::

$$< I(t)I(t+\tau) >= \lim_{T\to\infty} \frac{1}{T} \int_t^T I(t')I(t'+\tau)dt' \tag{22}$$

with τ the correlation time. From its definition, $< I(t)I(t+\tau) >=< I^2 >$ for $\tau = 0$ and $< I(t)I(t+\tau) >=< I >^2$ for $\tau \to \infty$. We can further define the intensity correlation function:

$$g_I^{(1)}(q,\tau) = \frac{< I_s(q,t)I_s(q,t+\tau) >}{< |I_s(q,t)|^2 >} \tag{23}$$

and the electric field correlation function:

$$g_E^{(1)}(q,\tau) = \frac{< E_s(q,t)E_s^*(q,t+\tau) >}{< |E_s(q,t)|^2 >} \tag{24}$$

which are related through the Siegert relation [72, 73]:

$$g_I^{(1)}(q,\tau) = 1 + \beta_m |g_E^{(1)}(q,\tau)|^2 \tag{25}$$

whenever the scattered electric field and the scattered intensity are, from a statistical point of view, Gaussian variables, with β_m the coherence factor.

Through the Siegert relation, it is possible to relate scattering information with physical magnitudes: From the time dependence of the scattered intensity, the intensity correlation function can be determined, using a correlator and converted into the electric field correlation function, which we can relate to the dynamic structure factor, $f(q,\tau) = \frac{1}{N}\sum_{i,j=1}^{N} < e^{-i\vec{q}\cdot(\vec{r}_i(0)-\vec{r}_j(\tau))} >$ and the static structure factor, $S(q) = \frac{1}{N}\sum_{i,j=1}^{N} < e^{-i\vec{q}\cdot(\vec{r}_i(0)-\vec{r}_j(0))} >$ using Eq.12 and Eq.24:

$$g_E^{(1)}(q,\tau) = \frac{f(q,\tau)}{S(q)} \tag{26}$$

In the limit of negligible interactions, $S(q) \to 1$ and the dynamic structure factor is a single exponential of the correlation time, τ. Hence:

$$g_E^{(1)}(q,\tau) = f(q,\tau) \sim e^{-Dq^2\tau} \tag{27}$$

where $D = \frac{k_b T}{6\pi\eta a}$ is the diffusion coefficient of the particles with k_b the Boltzmann constant, T the temperature, η the solvent viscosity and a the hydrodynamic radius of the particle.

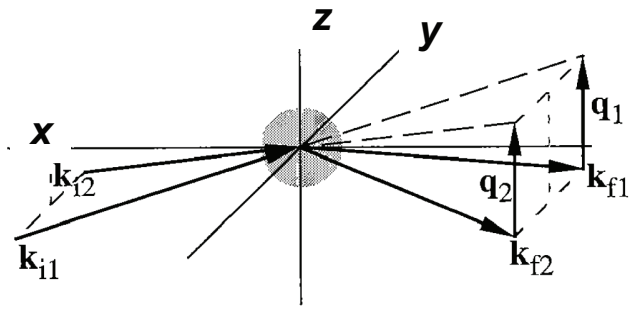

Figure 6: Schematic representation of the q-vector arrangement for a 3-D light scattering configuration. Taken from [80]

Up to this point, we have implicitly assumed that only single scattering events were occurring before the photons reached the detector. Unfortunately, when performing dynamic light scattering measurements on concentrated samples, multiple scattering is the rule rather than the exception. This makes the analysis of the scattering signal much more difficult since there is no characteristic scattering vector, $\mathbf{q}$, anymore. There are, however, techniques to suppress multiple scattering contributions to the intensity correlation function. These are called cross-correlation schemes [79, 80]. We achieve this in our experiments by cross-correlating the signal of two scattering experiments on the same scattering volume. To do so, we use a HeNe laser operating at a wavelength of 632.8 nm. This laser beam is split into two parallel beams that are focused onto the sample. Therefore, the experiment is no longer contained in a single scattering plane. The scattered light is collected and guided, using optical fibers, toward two avalanche photodiodes whose signals are cross-correlated. In this case, the cross-correlation function is:

$$G_{12}(\tau) =< I_1(t)I_2(t+\tau) > \tag{28}$$

where I_1 and I_2 correspond to the intensity detected in detector 1 and 2 respectively.

Since there are two beams and two detectors, $G_{12}(\tau)$ has for contributions:

$$G_{12}(\tau) =< I_{b1d1}(t)I_{b2d2}(t) > + < I_{b1d1}(t)I_{b1d2}(t) > + \\ < I_{b2d1}(t)I_{b1d2}(t) > + < I_{b2d1}(t)I_{b2d2}(t) > \tag{29}$$

where $I_{bidj}(t)$ is the intensity collected in detector j at a time t coming from beam i. Among all contributions, only the first term in Eq.29 contributes to the correlation, as it correlates with identical **q**, as shown in Fig.6; the other three cross-correlate with different **q** vector and thus, only contribute to the background. As a result, the normalized intensity cross-correlation function can be written as:

$$g_I(\tau) = \frac{G_{12}}{< I_1 >< I_2 >} = 1 + \beta|g_E(\tau)|^2 \tag{30}$$

where g_I is the normalized intensity cross-correlation function and $\beta = \frac{1}{4}\beta_M$ since only one out of the four contributions in Eq.29 contributes to the correlation. This intercept is often lower than *0.25* due to slight misalignments of the instrument and in the scattering volume seen by all beams and most importantly due to the presence of multiple scattering in the sample. The first two contributions are instrument dependent and thus, can be accounted for by performing measurements in a dilute sample. By doing so, we always obtain $\beta \approx 0.21$, which is close to the theoretical maximum.

2.2.2 Rheology

There are many ways a material responds to an applied force. For example, the deformation of a spring or a rubber band is directly proportional to the applied force while for water or oil, the applied force is proportional to the deformation rate rather than to the deformation itself. Many other materials, like mayonaisse or paints, exhibit more complex responses. Rheology is concerned with the study of flow and deformation in all these materials [81].

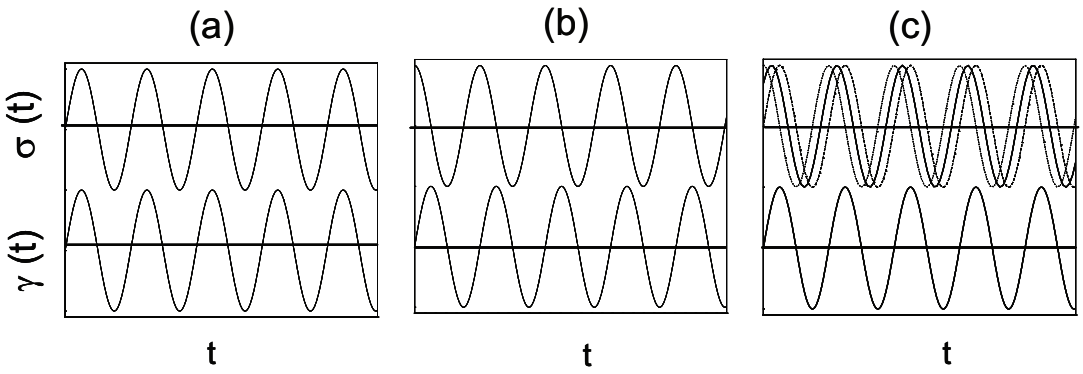

Figure 7: Stress as a function of time for different types of materials. In the bottom part, we represent the applied deformation (strain). a) Solid material; b) Viscous material; c) Viscoelastic material.

In a steady-state rheology test, a probe deformation (or a stress) is applied to the material and its response is measured after achieving steady-state conditions. In oscillatory tests, a sinusoidal deformation of amplitude γ and frequency ω, $\gamma(t) = \gamma e^{i\omega t}$, is typically applied and the corresponding stress response, $\sigma(t)$, is measured. For elastic materials, the stress is directly proportional to the applied deformation:

$$\sigma(t) = G'\gamma(t) \tag{31}$$

where G' is the elastic modulus of the system:

$$G' = \frac{\sigma}{\gamma} \tag{32}$$

with σ the amplitude of the measured stress. There is no phase difference between the applied and the response signals, as shown in Fig.7a.

For a purely viscous material, the stress is linearly related to the shear rate, $\dot{\gamma}(t)$:

$$\sigma(t) = \eta\dot{\gamma} = i\omega\eta\gamma(t) \tag{33}$$

with η the viscosity of the material. In this case, there is a $\pi/2$ phase difference between the strain and the stress, as shown in Fig.7b. The proportionality constant between σ and $\dot{\gamma}$ defines the viscous modulus, $G'' = \omega\eta$.

Most materials, however, are neither purely elastic nor purely viscous. They show what is called 'viscoelastic' behavior, which is characterized by a general equation of the form:

$$\sigma(t) = G^*\gamma \tag{34}$$

where $G^* = G' + iG''$ is the complex modulus of the system. As a result, the stress and the strain have a phase difference, δ, which lies between 0 and $\pi/2$. An example of this is shown in Fig.7c. The phase lag can be calculated as:

$$\delta = \arctan\frac{G''}{G'} \tag{35}$$

Similarly, the stress and the shear rate become related by a complex viscosity, η^*:

$$\sigma(t) = \eta^*\dot{\gamma} \tag{36}$$

with $\eta^* = \eta' - i\eta''$. As a result, $G^* = -i\omega\eta^*$, $\eta' = \frac{G''}{\omega}$ and $\eta'' = \frac{G'}{\omega}$.

Eq.31, 33, 34 and 36 are called constitutive equations and establish simple relations between forces and deformations for different types of materials. Note that the elastic and viscous moduli are constant within certain γ and σ ranges. This range is referred to as the *linear region*. Above certain γ and σ values both G' and G" exhibit a deformation dependence [83]. For the above equations to be significant, we must measure the moduli in the linear regime.

We use a stress-controlled rheometer (Anton Paar Physica MCR 501) [84], which, as any other rheometer of this type, applies a force and measures the deformation. There are other rheometers, called strain-controlled rheometers, which impose a deformation and measure the resultant force. Stress-controlled rheometers can operate as strain-controlled rheometers if the feedback loop by which the applied force is converted into a deformation is fast enough. In this way, the rheometer would apply a force, measure the induced deformation, compare with the wished deformation and rectify the applied force. The time scale associated to this feedback loop limits the

highest frequencies achievable with the instrument in oscillatory measurements. For our rheometer, this time is in the order of milliseconds enabling the equipment to span a frequency range that is comparable to existent strain-controlled rheometers.

The stress is applied using a permanent-magnet synchronous-drive motor located inside an air bearing. The instrument is able to apply and measure torques, which are then converted stress using the particular geometry of the tool in contact with the sample. The strain is measured using an optical encoder. In our experiments, we use a double-Couette geometry and a cone-plate (CP) geometry with cone radius 20mm and angle 2^o. Before the measurement, we perform preliminary tests to quantify the noise associated to the motor and the air bearing; this arises from imperfections in the motor operation, imperfections in the surface of the air bearing and, most importantly, due to turbulence in the effluent air as it flows into the bearing. We measure the stress-strain relationship in the absence of sample. In addition, we also perform measurements without sample to quantify the inertia associated to the tool; we rotate the tool at different constant speeds and in oscillatory mode at different frequencies.

2.2.3 Experimental System

We use microgel particles based on 2-vinylpyridine, a weak base that consequently ionizes at low pH. The synthesis procedure was done following Loxley et al [33]. We use a surfactant-free emulsion polymerization method in which 15.968 g of 2-vinylpyridine monomer and 0.032 g of divinylbenzene, DVB, (0.2 % weight ratio of cross-linker to monomer) were mixed with 1584 mL of deionized water in a three-neck round bottom flask. The solution was deoxygenated by stirring at 300 rpm for 20 min under an inert atmosphere which we achieve by nitrogen bubbling. The reaction was initiated through the addition of 0.64 g of an initiator 2,2-azobis(2-amidinopropane) dihydrochloride (V-50) and carried out for 4 hours at 70 ^{o}C. The final products were

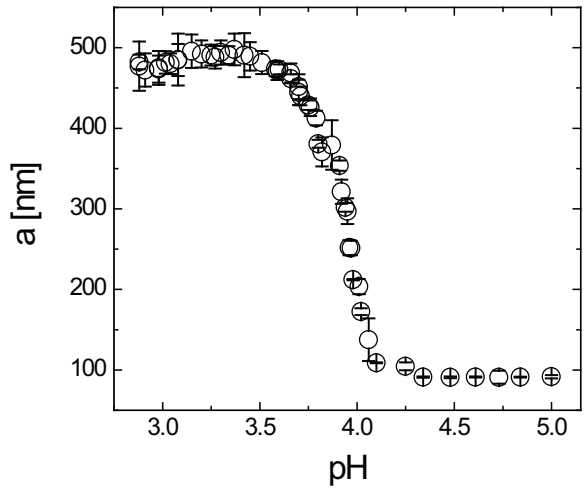

Figure 8: a) 2-VP particle radius as a function of the solution pH. The particle starts swelling for pH<4.2.

filtrated and extensively dialyzed against ultrapure water until the conductivity of the water from the sample was equal to the conductivity of ultrapure water.

The particles are deswollen at high pH and swell as the pH is decreased below pH≈4, as shown in Fig.8; This reflects the ionization of VP groups, which drives the entrance of counterions inside the particle consequently increasing the osmotic pressure and promoting the particle swelling. The equilibrium size of the particles reflects the balance between the ionic osmotic pressure and the entropy associated to the polyelectrolyte network [85].

2.3 Experimental Results

2.3.1 Phase behavior of the system

For deswollen particles, the phase behavior that results from increasing ζ is reminiscent of charged hard spheres. The system exhibits liquid and crystal phases as well as liquid-crystal coexistence, as shown in Fig.9. Note, however, that the volume fractions for melting and freezing are lower than the corresponding volume fractions for hard sphere suspensions (Fig.1). This arises from the surface charge of the microgel particles due to the initiator employed in the synthesis. This charge increases the

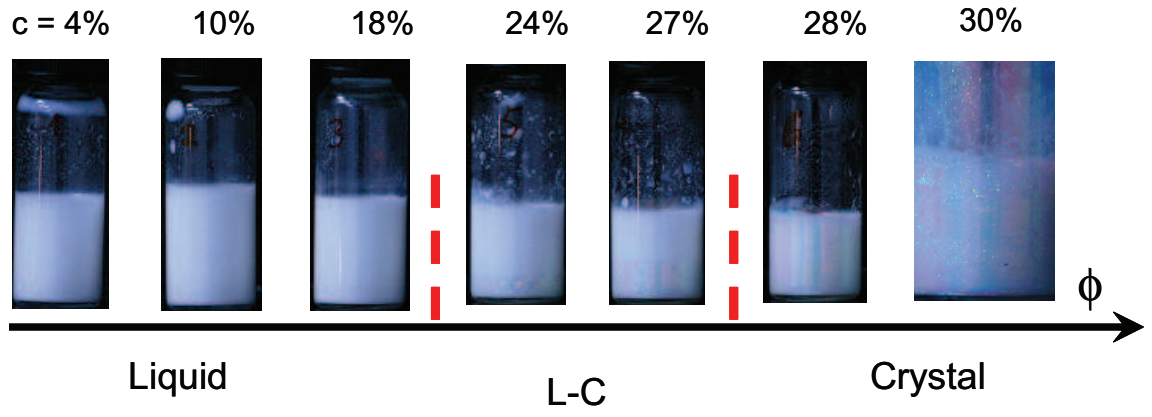

Figure 9: Phase behavior of the 2-VP microgels in a deswollen state. The system behaves as a system of charged hard spheres. The displacement of the crystal and the coexistence region to smaller ϕ is a consequence of the particle surface charge density.

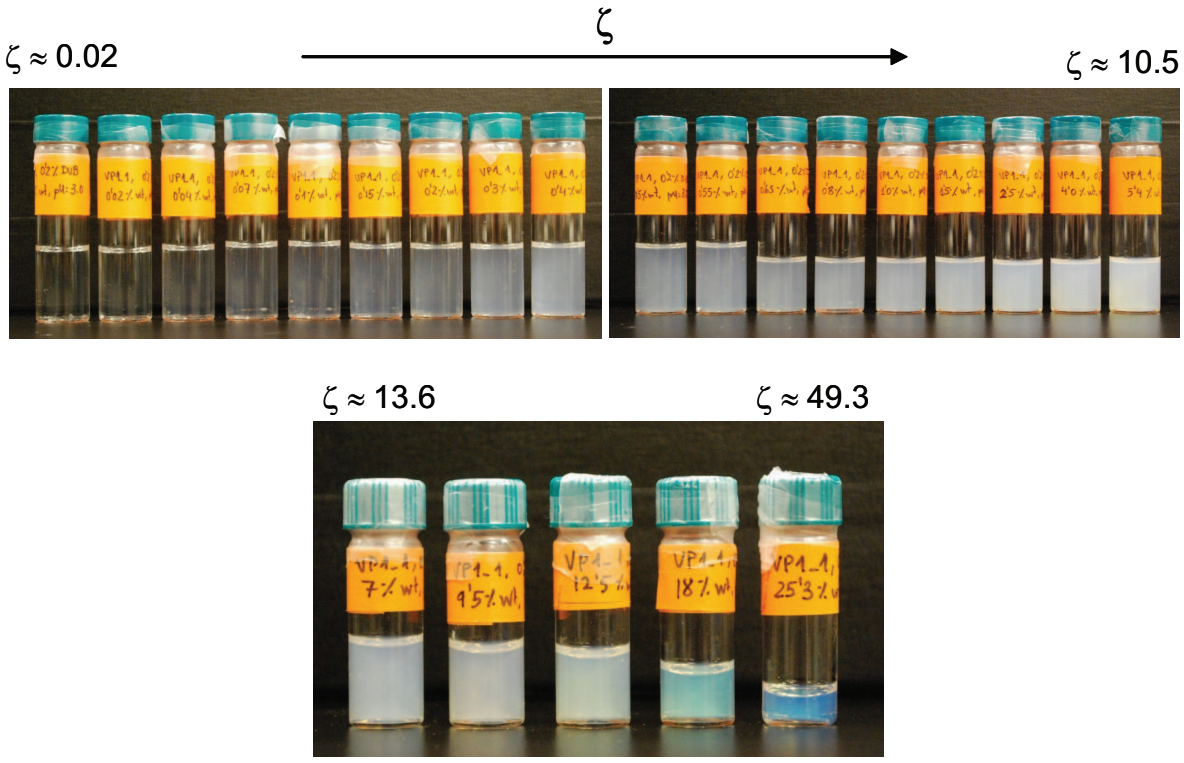

Figure 10: Phase behavior of the system in the swollen state. The system remains a liquid within the whole range of ζ.

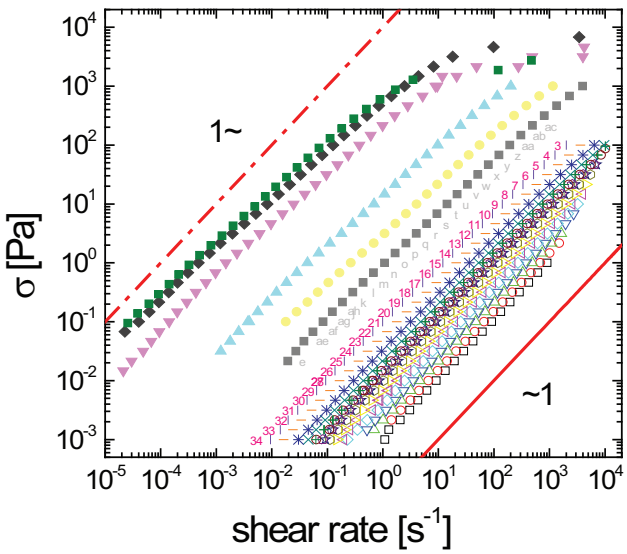

Figure 11: Steady-state response of the 2-VP microgel at different concentrations. The stress varies linearly with the shear rate as expected for purely viscous materials (Eq.33).

effective volume fraction resulting in crystallization at lower ϕ.

By contrast, when particles are fully swollen at pH=3 the phase behavior lacks any crystal phase irrespective of ζ as inferred from the absence of Bragg reflections in the samples (Fig.10).

2.3.2 Steady-state flow behavior

In this experiments, we monitor the strain response of the samples after application of a certain stress. For $\zeta < 10.5$, the measurements were done using a Double-Couette geometry in order to maximize the contact area between the sample and the tool so as to have a sufficient torque in the instrument. For $\zeta > 10.5$, we use a 20mm cone-plate (CP) geometry with a 20μm gap and a tilt of angle 2^o to measure; in this case the viscosity of the samples provided enough torque even for the small contact area provided with this tool [82]. In all measurements, we ensured that the time of the measurement was longer than a full revolution. We find that for all ζ the system exhibits a linear behavior of σ with the shear rate, $\dot{\gamma}$, characteristic of viscous

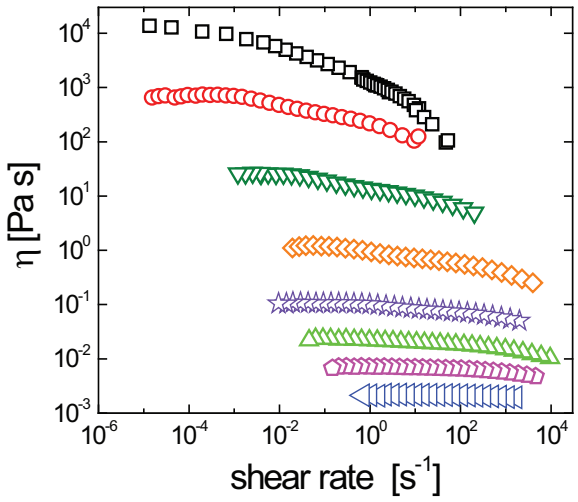

Figure 12: Viscosity as a function of shear rate for: (◁) $\zeta = 0.14$; (○) $\zeta = 0.58$; (△) $\zeta = 19.2$; (⋆) $\zeta = 7.83$; (◇) $\zeta = 24.4$; (◁) $\zeta = 49.3$; (○) $\zeta = 68.2$; (□) ζ =97.5;

materials, as shown in Fig.11. This is true except at the highest ζ we can measure where this linearity is lost for sufficiently large $\dot{\gamma}$. These results confirm the absence of a solid-like phase for these suspensions. Instead, the samples are liquid-like and have a well defined low shear viscosity.

From the data, we calculate the viscosity of the material using Eq.33. As expected for a Newtonian liquid, the viscosity is essentially constant with $\dot{\gamma}$; the system does not display shear thinning. This is true except at the highest ζ we can achieve. For hard colloids, shear thinning occurs when the local structure of the system is perturbed by the flow induced by the shear [81]. Computer simulations [86, 87] and experiments [88] show that in this case the free diffusion of the particles is negligible compared to the imposed hydrodynamic flow. As a result, the particles align themselves in 'string'-like structures somehow aligned by the flow. This relation is quantified by the Peclet number, $Pe = \dot{\gamma} t_d$, with $t_d = a^2/D$ the time required for a particle to diffuse its own radius and D the diffusion coefficient. At low $\dot{\gamma}$, the Peclet number is small and the suspension dynamics are dominated by the Brownian motion of the particles. By contrast, at high $\dot{\gamma}$, the time associated to the flow, $1/\dot{\gamma}$, is much smaller than t_d and

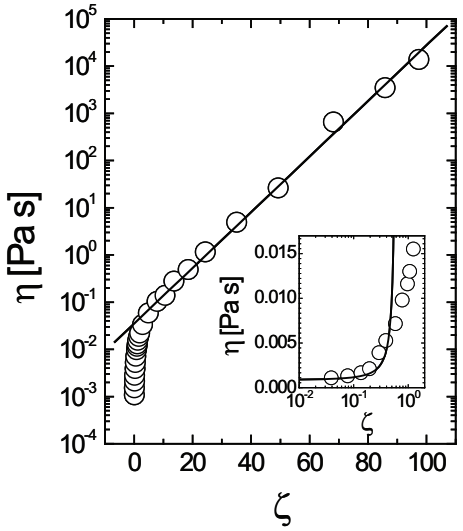

Figure 13: Viscosity as a function of ζ. The viscosity increases exponentially with ζ as shown by the linear fit (solid) line in a log-lin plot. Inset: Blow-up of the Figure at low ζ. The viscosity follows approximately the Krieger-Dougherty equation (Eq.38).

the suspension is affected by the imposed flow. Given our microgel size, $a = 500$ nm, we find that $Pe = 1$ for $\dot{\gamma} = 1.74\text{s}^{-1}$. This shear rate is well within our experimental range. However, we observe no shear thinning in our samples. This could reflect that the suspension at these high packings accommodates the imposed shear by deforming rather than by aligning the particles. The system is able to maintain a disordered structure at the expense of deforming the particles. At the highest ζ we can reach, the system starts exhibiting shear thinning. At these high concentrations, the particles have appreciably deswollen and start to mimic hard sphere behavior.

The viscosity of the system increases as ζ increases, as shown in Fig.13. For any suspension at low concentration, the viscosity is expected to increase with volume fraction as:

$$\eta = \eta_s(1 + [\eta]\phi) \tag{37}$$

where η_s is the viscosity of the solvent and $[\eta] = \lim_{\phi\to 0} \frac{\eta-\eta_s}{\phi\eta_s}$ is the intrinsic viscosity. For hard spheres, $[\eta] = 2.5$, a result due to Einstein [89]. At higher concentrations, Eq.37 does not hold anymore due to particle-particle correlations. At sufficiently

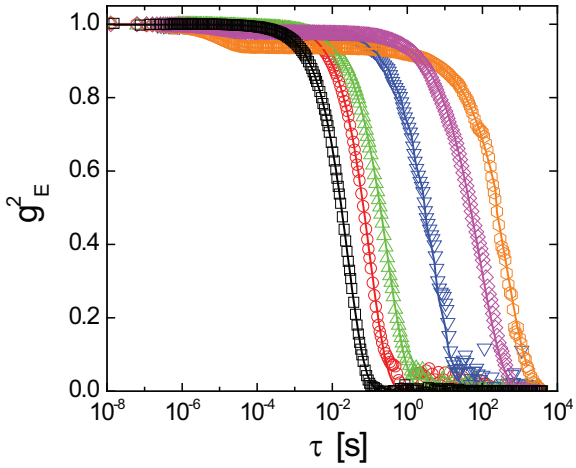

Figure 14: Normalized Electric Field correlation function as a function of time for different ζ: (□) $\zeta = 0.2$; (○) $\zeta = 1$; (△) $\zeta = 19.2$; (▽) $\zeta = 49.3$; (◇) $\zeta = 71.8$; (○) $\zeta = 91.8$. The solid lines represent the best fit following Eq.40

high ϕ, for particulate suspensions the viscosity can be described using the Krieger-Dougherty model [90]:

$$\eta = \eta_s(1 - \frac{\phi}{\phi_m})^{-[\eta]\phi_m} \tag{38}$$

where ϕ_m represents the maximum packing fraction in which the viscosity becomes infinite. Values for ϕ_m and $[\eta]$ have been tabulated for different type of particles in Barnes et al [91]. For hard spheres, $\phi_m = \phi_{rcp} = 0.64$. This model accounts for our experimental results for $\zeta \approx 0.4$, as shown in the inset of Fig.13.

The viscosity of the system for higher values of ζ is, however, markedly different than that predicted by the Krieger-Dougherty model. We observe that η increases exponentially with ζ. This behavior persist up to the highest ζ we can measure spanning five orders of magnitude in viscosity, as shown in Fig.13. By fitting the data to an Arrhenius behavior:

$$\eta \sim e^{C'\zeta} \tag{39}$$

we obtain C'=0.13.

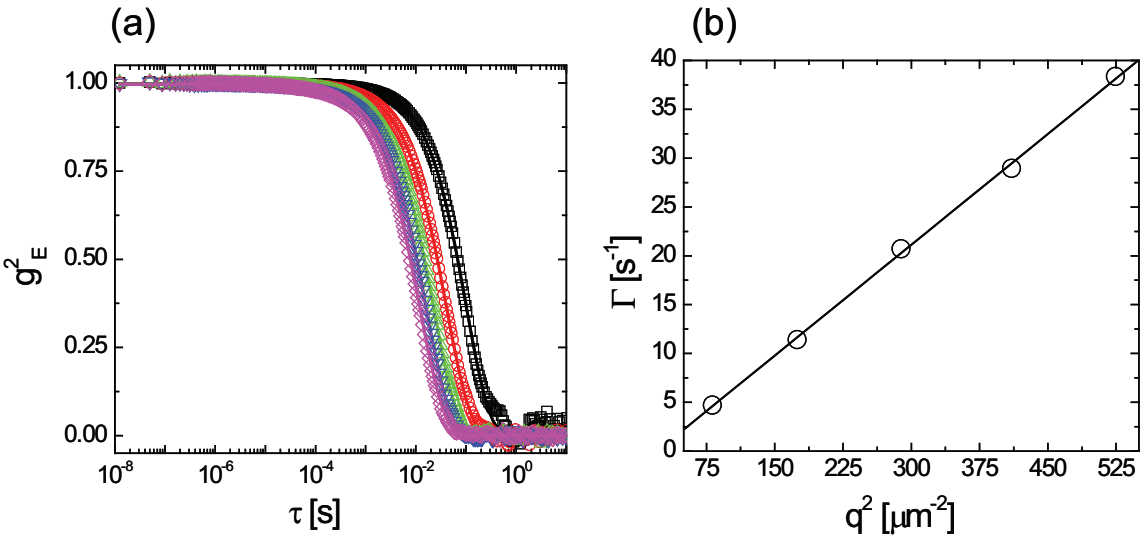

Figure 15: a)Normalized Electric Field correlation function as a function of time at different angles for $\zeta = 0.5$: (□) $\Theta = 40^o$; (○) $\Theta = 60^o$; (△) $\Theta = 80^o$; (▽) $\Theta = 100^o$; (◇) $\Theta = 120^o$. The solid lines represent the best fit following Eq.27. b) Relaxation frequency as a function of q^2. The solid line represents the best linear fit, from which a diffusion coefficient, $D = 7.1 \cdot 10^{-14} \frac{m^2}{s}$, is obtained.

2.3.3 Structural relaxation by Dynamic Light Scattering

A common way to explore the structural relaxation of suspensions is by performing dynamic light scattering measurements to determine the intensity correlation function of the system. We do this for different ζ, as shown in Fig.14 for different ζ. We change the scattering angle to assure that $qa \sim 2$ where we estimate an average particle size for $\zeta > 1$ as $a = a_0 \zeta^{-1/3}$, with a_0 the size measured in dilute suspensions. At low ζ, the system displays a single exponential decay, as shown in Fig.14 and Fig.15a, where we show the angular dependence of the correlation function for $\zeta = 0.5$. From the slope of $\ln(g_E^2)$ versus τ, we determine the relaxation frequency; it increases linearly with q^2, as shown in Fig.15b, and is consistent with diffusive relaxation. From the slope of the graph, we obtain a diffusion coefficient of $D = 7.1 \cdot 10^{-14} \frac{m^2}{s}$, and approximating the viscosity of the solvent as that of the suspension, $\eta = 6 \cdot 10^{-3}$ Pa s, we obtain a particle size of $a = 513$nm, which is in good agreement with the particle size measured in dilute suspensions (Fig.8). However, at larger ζ, the system starts to show a double

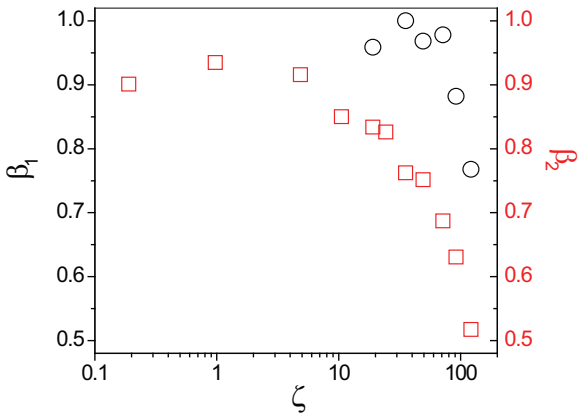

Figure 16: Dependence of β_1 (○) and β_2 (□) with ζ.

decay in which the decays are no longer simple exponentials. This has been previously observed for glass-former liquids [65] and colloidal suspensions [69] in their approach to the glass. Our dynamic structure factor can then be written as:

$$f(q,\tau) = A_1 e^{-(\Gamma_1 \tau)^{\beta_1}} + A_2 e^{-(\Gamma_2 \tau)^{\beta_2}} \tag{40}$$

where A_i, Γ_i and β_i are the amplitude, the relaxation frequency and the exponent of the i-th decay. For most concentrations, $\beta_1 \approx 1$, and decreases at very high ζ, as shown in Fig.16 with black circles. The corresponding relaxation frequency is due to diffusion; it scales linearly with q^2, as shown in Fig.17a for $\zeta = 71.7$ as an example. By fitting the experimental points to a line, we obtain $D = 2.4 \cdot 10^{-10} \frac{m^2}{s}$, which is several orders of magnitude larger than the diffusion coefficient of the particles in dilute suspensions; this mode must thus be associated to the local giggling of the particles in their average location. The relaxation frequency also increases with ζ, as shown in Fig.17b. Larger relaxation frequencies imply shorter time scales and, thus, faster dynamics. As the the particles compress when ζ is increased, this give rise to faster responses.

The second relaxation mode is characterized by a strong dependence of β_2 with ζ, as shown in Fig.16 with red squares. This relaxation is thus non-diffusive for all ζ.

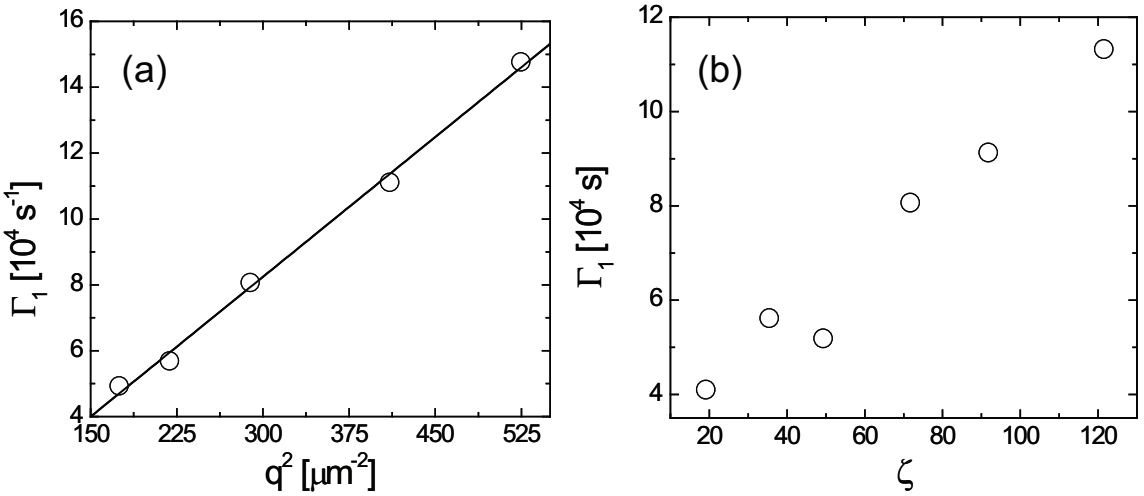

Figure 17: a)Relaxation frequency as a function of q^2 for $\zeta = 71.7$. The solid line represents the best linear fit wit $D = 2.4 \cdot 10^{-10} \frac{m^2}{s}$. b)Relaxation frequency as a function of ζ at qa$\sim$2

To further characterize it, we determined the average structural relaxation time:

$$t_\alpha = \frac{t_2}{\beta_2}\Gamma(1/\beta_2) \tag{41}$$

with $t_2 = \Gamma_2^{-1}$ and $\Gamma(1/\beta_2)$, the value of the Gamma-function in $1/\beta_2$. We find that t_α increases exponentially with ζ, as shown in Fig.18 with black circles. This experimental behavior of t_α is consistent with the exponential behavior of the viscosity, as emphasized in Fig.13. We, thus plot t_α versus η and observe that the structural relaxation time is essentially linear with the viscosity for $\zeta \geq 1$. The slope has dimensions of an inverse elastic modulus, which we find equals $G_p \approx 0.5$Pa. By further considering that the energy required for a structural relaxation in our system is k_bT and that for this to happen a local elastic deformation must occur, we interpret G_p as:

$$G_p \approx \frac{k_bT}{l^3} \tag{42}$$

where l^3 is the volume involved in the elastic deformation. Using G_p, we find $l \approx$ 200nm corresponding to a fraction of the particle size. This indicates the particle needs to deform an amount l to rearrange with respect to other particles, enabling

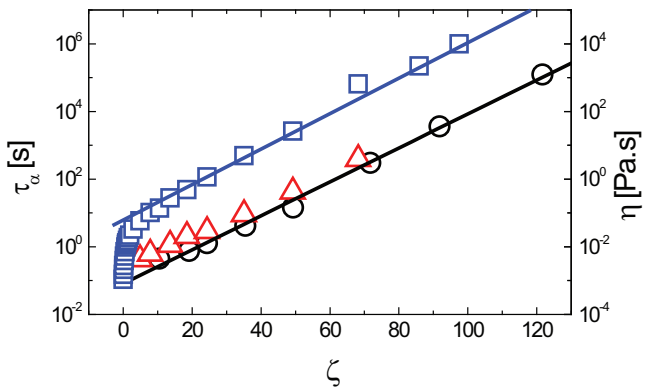

Figure 18: Structural relaxation time as a function of ζ obtained by dynamic light scattering ($\circ$) and oscillatory rheology ($\triangle$). The system presents an Arrhenius-type of relaxation (Eq.3) very similar to the viscosity ($\square$).

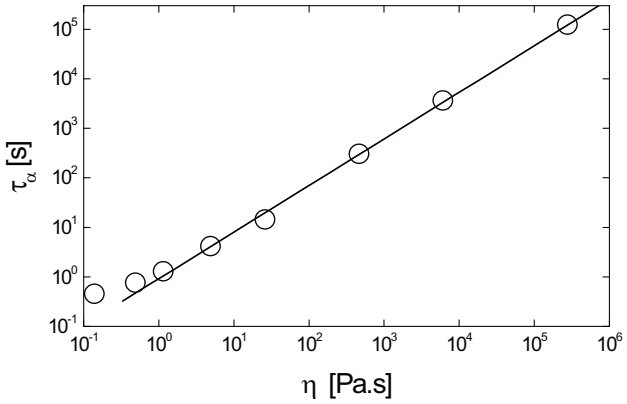

Figure 19: Structural relaxation time as a function of the system viscosity. The solid line represents the best fit to a linear trend, from which we obtain $G_p \approx 0.5$Pa.

the relaxation of the system. We note that the value of G_p is smaller than the bulk or shear modulus of the microgel particle measured in dilute suspension [92]. This results from the inhomogeneous distribution of cross-linker molecules within the microgel particle in which the density of cross-linker decreases towards their periphery [93]. We also note that his structural relaxation enables the system to remain ergodic at all the probed ζ, which further confirms the liquid-like behavior determined by steady-state rheology.

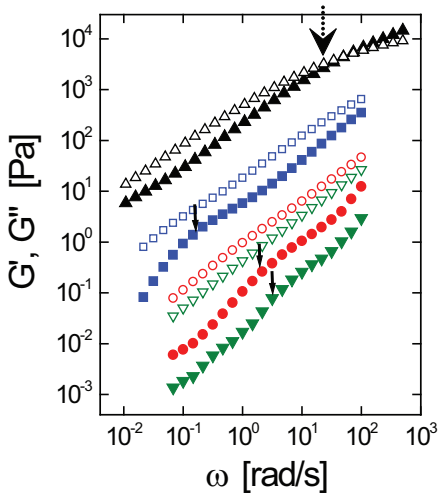

Figure 20: Storage (G' - Closed Symbols) and Loss (G"- Open symbols) for microgel suspensions at different ζ: ($\triangle$) $\zeta = 86.1$, ($\square$) $\zeta = 49.3$, ($\circ$) $\zeta = 24.4$, ($\triangledown$) $\zeta = 18.5$. The solid arrows represent the structural relaxation time of the system whereas the dotted arrow represents a cross-over related to polymer interpenetration.

2.3.4 Structural Relaxation determined by Oscillatory Rheology.

An alternative way to determine the structural relaxation time of the system is by doing oscillatory rheology. In these experiments, we measure the elastic modulus, G', and the storage modulus, G", as a function of the frequency for different ζ. As expected from the liquid-like character of the suspensions G" is larger than G' for all experimentally accessible frequencies. Only for the largest concentration, a cross-over between both moduli is observed as shown in Fig.20. The crossover frequency is, for $\zeta = 86.1$, $\omega_c \approx 70$ rad/s, corresponding to a relaxation time of 0.09 s, which is several orders of magnitude smaller than t_α measured by DLS. This crossover is, thus, not reflective of the structural relaxation we measure with dynamic light scattering. Despite this, we take this crossover as a reference and re-scale the data onto a master curve simply by displacing in frequency the curves, as shown in Fig.21. Whereas the scaling for G" is excellent the scaling for G' is not so convincing. To ascertain why this could be the case, we look closely at the behavior of G' with ω in Fig.20 and observe that at intermediate angular frequencies, there is a change in

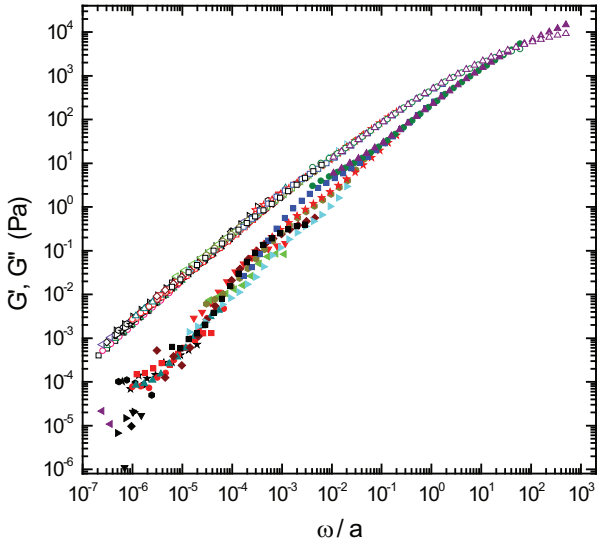

Figure 21: Master curve of G' and G" as a function of the normalized angular frequency. Whereas we obtain a good scaling for G", the scaling for G' is not good due to structural relaxations (Fig.20).

the growing trend of the elastic modulus. We emphasize where this change in ω is observed with arrows. The time scale associated to this kink is calculated for the corresponding angular frequency as $t_k = \frac{2\pi}{\omega_k}$. Remarkably, this time scale agrees with the structural relaxation times measured by Dynamic Light Scattering, thus reflecting the local relaxation associated to a microgel particle rearranging with its neighbors. This rearrangements ultimately control the viscosity of the suspension. The simple model assumed in understanding the master curve in Fig.21 fails as it assumes there is only one structural relaxation in the system, which is not the case. In addition to t_α, there is a faster relaxation indicated by the crossover in G' and G" at high ω. We hypothesize this relaxation is associated to the interpenetration of the outer polyelectrolyte in our microgel particles, which must disentangle before the particles can rearrange with its neighbors as it has been observed for star polymer systems [94].

To test this hypothesis, we measure the oscillatory response of polyelectrolyte

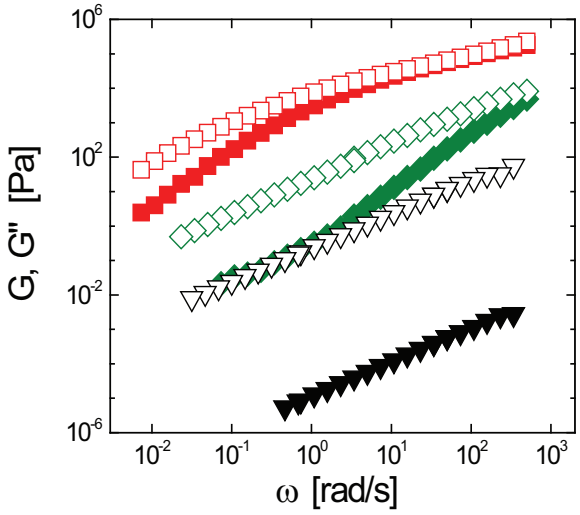

Figure 22: G' (Closed Symbols) and G"(Open symbols) for P4VP solutions at different concentrations: (□) c = 55% wt, (◊) c = 44% wt, (▽) c = 25% wt. At high c, the polymer solution shows a cross-over at high ω.

chains of Polyvinylpyrdine (PVP) with a molecular weight comparable to the molecular weight of the chains in our microgel particles. We estimate this by determining the distance between two cross-link points, $L = n_{x-link}^{-1/3}$, with n_{x-link} the cross-linker concentration inside one particle [95]. We obtain $L \approx 5$nm. In addition, for PVP chains in a Θ-solvent (ideal chains), the radius of gyration, R_g, is related to the molecular weight, M_w, by [77]:

$$R_g[nm] = 0.06\ M_w^{1/2} \tag{43}$$

By taking $L \approx R_g$, we obtain: $M_w \approx 7$ kg/mole. This is an approximate estimate, given that water at pH *approx*3 is a good solvent for PVP. In addition, we are implicitly assuming a homogeneous distribution of cross-linker within the particles, despite we know it most likely decays from the particle center towards its periphery [93]. As a result of these two assumptions, the outer chains are expected to be larger. We thus choose a commercial PVP with M_w=60 kg/mole.

The polyelectrolyte solution is essentially liquid-like, with G"≫G', for low concentrations. By contrast, for higher concentrations the system begins to display a

viscoelasticity and at sufficiently high concentration, we observe a crossover between G' and G", as shown in Fig.22. The origin of this change in behavior is related to the interpenetration of the polyelectrolyte chains [94]. As the concentration increases, the overlap between chains increases and the system develops some elasticity. Entanglements between the polymer chains occur above the entanglement molecular weight, M_e, which for PVP can be calculated as [96]:

$$M_e = \frac{M_{e,0}}{\phi_2} \tag{44}$$

with ϕ_2 the polymer volume fraction and $M_{e,0} = 13.3$kg/mol the entanglement molecular weight for a polymer melt in which $\phi_2 = 1$[97]. The number of entanglements per chain is defined as $n_e = M_w/M_e - 1$, with the minus 1 accounting for the fact that an entanglement involves two chains. For a typical polymer volume fraction we use in the PVP experiments, $\phi_2 \approx 0.45$, we obtain $M_w/M_e \approx 2$, indicating there is approximately one entanglement per chain. Interestingly, the angular frequency range over which the cross-over occurs is very similar to where it occurs for our microgel particles, confirming that entanglements between chains could be at play in the overall relaxation of our suspensions. Nevertheless, this relaxation mechanism is not the only one present in the samples. To emphasize this, we plot the viscosity of the PVP solutions as a function of concentration and compare the result with the viscosity of our microgel suspension. Both the trend and the values of η are very different as shown in Fig.23. This reflects that the viscosity of the microgel solution is not only affected by the entanglement of the polyelectrolyte chains but also by the structural relaxation associated to particle rearrangements with respect to its neighbor. However, this is very different from hard spheres. While in this case, collective rearrangements are the ultimate responsible for the viscosity of the system [18, 19], in our case the Arrhenius behavior of the viscosity reflects that it is controlled by local rearrangements. The constant local elasticity can only result because of interpenetration. Otherwise, the elasticity will increase with ζ and the structural relaxation time will not be linear

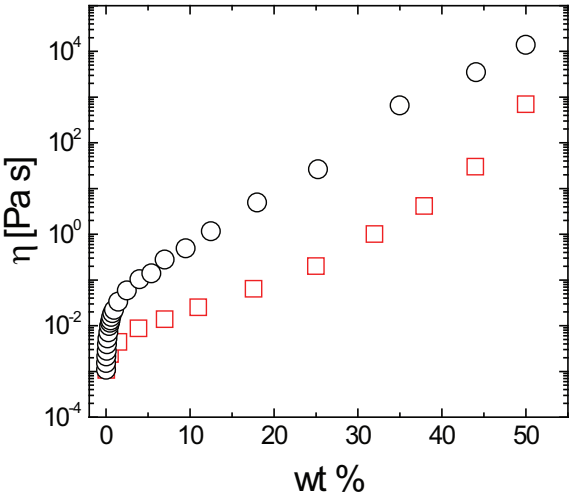

Figure 23: Concentration dependence of the viscosity for the polyelectrolyte solution (□) and the microgel suspension (○).

with the viscosity.

CHAPTER III

OSMOTIC PRESSURE IN MICROGEL SUSPENSIONS

3.1 Introduction

As a result of the intrinsic softness of microgel particles, when the suspension is concentrated over $\zeta = 1$, the particles must interpenetrate and shrink due to the presence of other particles. Recent interpretations of data suggest that this indeed happens, but already at $\phi \approx 0.3$ as a result of the osmotic pressure exerted by the suspension itself. In all works where this is concluded, the data interpretation relies on comparison with hard sphere behavior. For instance, if the viscosity of a microgel suspension, say for $\zeta = 0.5$, is lower than that of a hard sphere system, at $\phi = 0.5$, this is interpreted as evidence for $\zeta \neq \phi$ and for affirming that the actual ϕ for the corresponding ζ must be lower as a result of deswelling induced by the osmotic pressure of the suspension

An alternative scenario based on what we have seen in the previous chapter is that microgels are different than hard spheres and their softness affects the phase behavior in ways that we do not fully understand yet. For deswelling to occur, the osmotic pressure must be comparable to the bulk modulus of the microgel [98, 99]. This condition is reminiscent of what is required to deform an emulsion drop. The osmotic pressure required to do so must be comparable to the Laplace pressure [61]. As it turns out, for emulsion drops, this condition is achieved at $\phi_{rcp} = 0.64$ [61, 100]. In this chapter, we will determine a corresponding condition for microgels to answer whether these particles indeed deswell at volume fractions below ϕ_{rcp}. In order to do so, we will independently measure the osmotic pressure of a microgel suspension as a function of ζ and the bulk modulus of individual particles.

3.2 Determination of the bulk modulus of microgel particles

3.2.1 Preliminaries

Several methods have been proposed to characterize the single-particle elasticity of microgel particles. Most commonly, the elastic behavior of these particles has been accessed using Atomic Force Microscopy (AFM) [101, 102, 103]. In this approach, a dilute microgel suspension is initially spread over a silicon wafer, which is previously pretreated with a polymer solution to ensure microgel attachment. A representative elastic constant of the particle is then obtained from the force/displacement relationship using an AFM tip as a probe. Recently, a novel approach based on microfluidics has been developed [104]. In this alternative approach, a solution of microgel particles is pushed through a tapered capillary by imposing a known pressure difference between the extremes of the capillary. The modulus of the microgel is obtained from the balance of the applied pressure, the normal stresses due to the capillary and the internal stresses of the particle.

An alternative method involves taking advantage of the microgel swelling behavior. Since the equilibrium size of the particle is determined by the absence of an overall osmotic pressure acting on the particle [47], the application of an external osmotic pressure, Π_{ext}, which can be induced by the presence of a suitable non-adsorbing polymer, results in a change in the particle size [48, 49], providing a simple and non-invasive way to determine the particle stiffness. This procedure has been used to study the osmotic de-swelling of ionic microgels [92] and, more recently, to characterize the elastic properties of thermorresponsive microgels [20].

As the stressing polymer, we use dextrans which were previously characterized from a rheological and osmotic point of view. To measure the particle size we use dynamic light scattering (DLS), which is an appropriate technique given that microgels are colloidal particles. However, in order to do so, we must consider the presence of the dextrans; they not only change the viscosity of the continuous phase but, at

sufficiently high concentrations, can also exhibit relaxation processes reflecting dextran/dextran interactions [92]. In this situation, the intensity correlation function used to extract the microgel diffusion coefficient and ultimately its size, can thus contain contributions from the dextrans that can obscure the extraction of the desired information. It is thus essential to know the dynamics of the dextran solutions if they are going to be used to de-swell the microgel particles. With this information at hand, we find that VP microgels de-swell above a threshold Π_{ext}, as expected [98]. In this region, we can determine the particle bulk modulus or inverse compressibility, K, by independently measuring Π_{ext} and the microgel volume V_{1p}, since:

$$K = -V_{1p}(\frac{\partial \Pi_{ext}}{\partial V_{1p}}) \tag{45}$$

3.2.2 Experimental system

We use microgel particles based on VP. They are made by emulsion polymerization, a synthesis method that yields spherical and highly monodisperse particles [105]. The vinylpyridine (VP) microgels are cross-linked with divinylbenzene (DVB). We varied the amount of cross-linker and generated particles with 0.5, 1.3 and 3.5 weight per cent of DVB. Details about the particle preparation can be found elsewhere [33, 85]. All chemicals used are provided by Sigma with a reagent grade and used without further purification. After completing the synthesis, the suspensions were exhaustively dialyzed against deionized water until the conductivity of the dialysate became equal to that of pure water.

For dilute microgel suspensions, the electric field correlation function is an exponential, $e^{-\Gamma\tau}$, with $\Gamma = Dq^2$ the relaxation frequency and D the diffusion coefficient of the particle. We obtain D by performing a linear fit of Γ versus q^2 and use the Stokes-Einstein relation (Eq.27) to determine the particle radius. We find that a changes with pH in the case of the VP microgels, as shown in Fig. 24. The particle swells for pH $\leq$ 4.2, which approximately corresponds to the pKa of the VP groups [85].

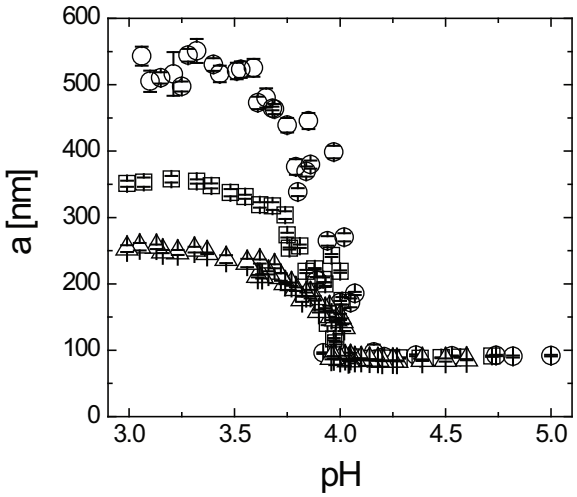

Figure 24: Swelling behavior of VP-DVB microgels as a function of pH for different cross-linker weight concentrations: (○) 0.5%, (□) 1.3%, (△) 3.5%.

Above this pH, the network is essentially neutral and the particles are de-swollen. By contrast, at lower pH, the VP groups charge resulting in increased counterion concentration inside the particle, which in turn causes swelling of the particles. As the amount of crosslink increases, the elastic contribution to the total osmotic pressure increases and the maximum achievable size decreases, as shown in Fig.24

3.2.3 Osmotic pressure and viscosity of dextran solutions

We use dextrans from Sigma $(C_6H_{10}O_5)_n$ with a molecular weight of Mw=150000 g mol^{-1} to induce an external osmotic pressure, Π_{ext}. We determine the Π_{ext} as function of dextran concentration using a commercial membrane osmometer (Wescor 4420). The method to obtain the osmotic pressure relies in determining the osmotic pressure difference between a dextran solution and a reference solution made of NaCl at 0.9 weight per cent. The apparatus uses a pressure transducer for this. Both solutions are in contact through a thin membrane with a low cut-off size in order to prevent the transient of large molecules. After some time, osmotic equilibrium between both sides of the membrane is achieved. The transducer then measures the pressure difference between both sides of the membrane and converts this reading into an electrical signal

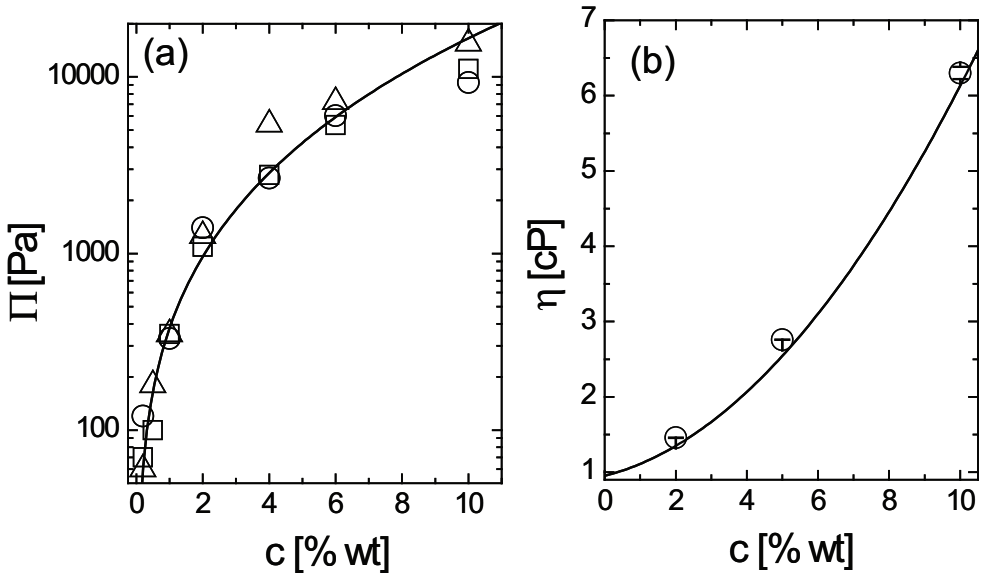

Figure 25: (a) Osmotic pressure as a function of dextran concentration: (□) pH=3.2, (○) pH=4.5 and (△) pH=5.5. The solid line corresponds to Π [Pa] = 286c + 87c^2 + 5c^3, with c expressed in weight %, which was previously determined for the same dextrans [106]. (b) Viscosity versus dextran concentration. The experimental line corresponds to η=0.932+0.119c+0.0399c^2 [92]

which, in turn, is related to a particular Π_{ext} through a previous calibration using an albumin solution of known osmotic pressure. We find that Π_{ext} increases with dextran concentration irrespective of pH, as shown in Fig. 25a. This increase is in excellent agreement with previous results for the same dextran solution [106], as shown by the line in this same figure. In addition, the pH independence is consistent with previous findings [107, 108].

The concentration dependence of the solution viscosity, η, has also been reported for this type of dextrans [92]. It was found that η=0.932+0.119c+0.0399c^2 within the concentration range $1\% < c < 11\%$. We have confirmed this expectation for three dextran solutions using a stress controlled rheometer (Anton Paar MC501), as shown in Fig. 25b.

3.2.4 Light Scattering of dextran solutions

We measure the intensity correlation function of dextran solutions in the range $1\% < c < 10\%$. At low c, the dynamic behavior is characterized by a single decay, while at larger c, there are two distinct decays in $g_E(\tau)$ (Eq.25) at widely separated time scales, as shown in Fig. 26a; this is consistent with previous studies on a similar system [109]. To account for this behavior we consider that $g_E(\tau)$ is determined by the sum of two stretched exponentials [111]:

$$g_E(\tau) = A_{slow} \exp(-(\Gamma_{slow}\tau)^{\beta_{slow}}) + A_{fast} \exp(-(\Gamma_{fast}\tau)^{\beta_{fast}}) \tag{46}$$

where A_{slow} and A_{fast} are the amplitudes of the two relaxation modes, with $A_{slow} + A_{fast} = 1$, β_{slow} and β_{fast} are the corresponding stretched exponents, with $0 < \beta < 1$, and Γ_{slow} and Γ_{fast} are the corresponding relaxation frequencies. Using this model, we fit the experimental $g_E(\tau)$ leaving as free parameters A_{slow}, A_{fast}, β_{slow}, β_{fast}, Γ_{slow} and Γ_{fast}. Good agreement between the model and the data is obtained, as shown in Fig.26a and in its inset, where, as an example, we also show the slow and fast mode contributions for $c = 4\%$. As anticipated, at low c, $g_E(\tau)$ is mainly dominated by the fast mode since A_{slow} is much smaller than A_{fast}. As c increases, the long-time relaxation mode becomes increasingly important and A_{slow} increases while concomitantly A_{fast} decreases with c. For $c \geq 4\%$, the contributions of both modes to $g_E(\tau)$ remain unchanged, as shown in Figs.26b,c.

The fast mode is characterized by a stretched exponent $\beta_{fast} \approx 1$ irrespective of concentration, as shown in Fig. 26d. This indicates that this mode is well described by a purely exponential behavior, suggestive of diffusive behavior. In addition, the relaxation frequency associated to this mode remains essentially constant for $c < 2\%$ and progressively increases for larger c, as shown in Fig. 26f. By contrast, there is an abrupt increase in Γ_{slow} and β_{slow} around $c \approx 2\%$, as shown in Figs. 26e,g. For lower c, both magnitudes are essentially constant, while at larger c, β_{slow} is constant

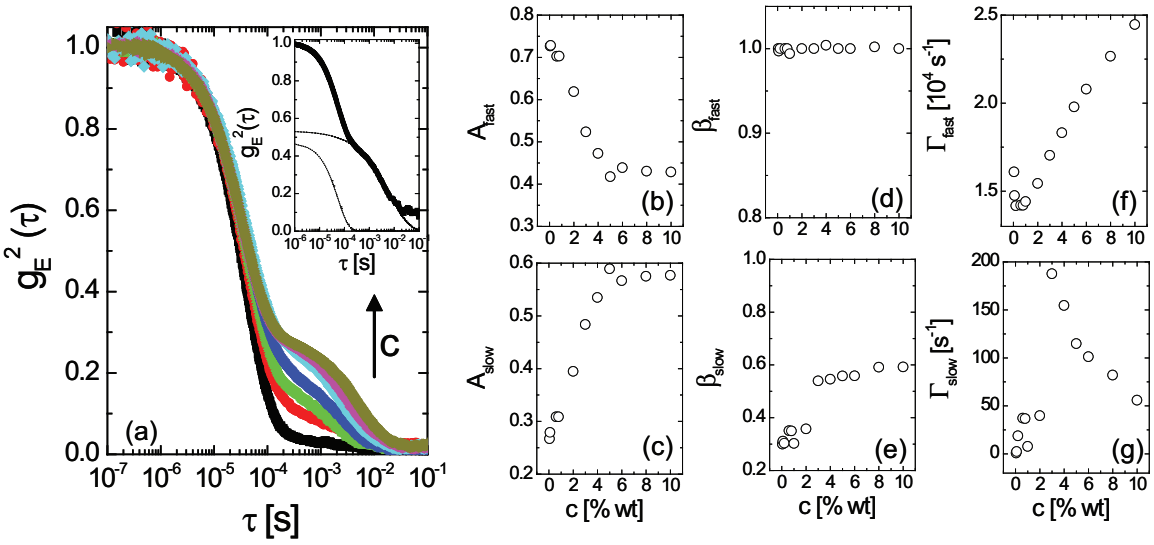

Figure 26: (a) $g_E^2(\tau)$ versus correlation time for various dextran concentrations. From bottom to top, c is 1, 2, 3, 4, 5, 8, 10 weight %. Solid lines indicate fits according to Eq.46. The inset shows the field correlation function for $c = 4\%$; dotted and dashed lines correspond to contributions from fast and slow modes, respectively. (b,c) Amplitudes, (d,e) stretching exponents, and (f, g) relaxation frequencies of the slow and fast relaxation modes as a function of dextran concentration.

and approximately 0.5-0.6, while Γ_{slow} decreases with c. Our data is consistent with previous experiments [106]. At low concentration, $A_{fast} \gg A_{slow}$, $\beta_{fast} \approx 1$ and Γ_{fast} is approximately constant indicating that the dynamics are dominated by diffusion of isolated dextran macromolecules or small dextran clusters. For concentrations larger than 2%, the jump in β_{slow} and Γ_{slow} are indicative of extensive dextran interactions, which could eventually result in formation of a space-spanning network. Concomitantly, the slow relaxation mechanism dominates over the fast mode and Γ_{slow} decreases with c, indicating that relaxations within this network become slower [109].

3.2.5 Light scattering of microgel suspensions in the presence of dextran

We measure the intensity correlation function for microgel/dextran mixtures and use Eq.25 to obtain $g_E(\tau)$. The experiments are performed at pH=3, where the VP microgels are fully swollen, and for dextran concentrations below which depletion-induced

flocculation of the microgel particles does not occur [92]. Within this concentration range, the correlation functions exhibit a two-step relaxation decay, similar to those obtained for the dextran solutions. However, the presence of the microgel to the overall scattering must be accounted for in this case. As a result, we add a contribution due to the microgels to the dextran solution field correlation function:

$$g_E(\tau) = A_{slow}\exp[-(\Gamma_{slow}\tau)^{\beta_{slow}}] + A_{fast}\exp[-(\Gamma_{fast}\tau)^{\beta_{fast}}] + A_{mgel}\exp[-(\Gamma_{mgel}\tau)^{\beta_{mgel}}] \quad (47)$$

where the first two modes correspond to the dextran relaxation modes and the third one corresponds to the microgel relaxation. We fit the experimental with Eq. 47, fixing β_{slow}, β_{fast}, Γ_{slow}, Γ_{fast} and the ratio of the amplitudes corresponding to the slow and fast relaxation modes of the dextran solution, R=A_{slow}/A_{fast}, to the values previously obtained for the dextrans solutions alone. We thus leave as free parameters the relaxation frequency corresponding to the microgels, Γ_{mgel}, and the stretching exponent of the streched exponential associated to this contribution, β_{mgel}. Of the three amplitudes, only one is independent since the ratio of A_{slow} and A_{fast} is known from the isolated dextran measurements and A_{mgel} + A_{fast} (1 + R) = 1. We choose A_{fast} as the independent amplitude in the fits.

The model correctly accounts for the experimental electric field correlation function, as shown in Fig.27a,b for two representative values of c. We also plot the individual contributions to $g_1(\tau)$. It is important to note that β_{mgel} is always ≈1 and that Γ_{mgel} is linear with q^2, as expected for particle diffusion. In addition, A_{mgel} is greater than A_{slow}. This, however, is no longer true for c≥2%, as shown in Fig. 27c. Above this concentration, the contribution to $g_E(\tau)$ coming from the microgel particles is no longer dominant over the contribution to $g_E(\tau)$ coming from the dextran solution possibly due to the reduced refractive-index mismatch between the particles and the dextran solution. In this situation, no reliable information about the microgel

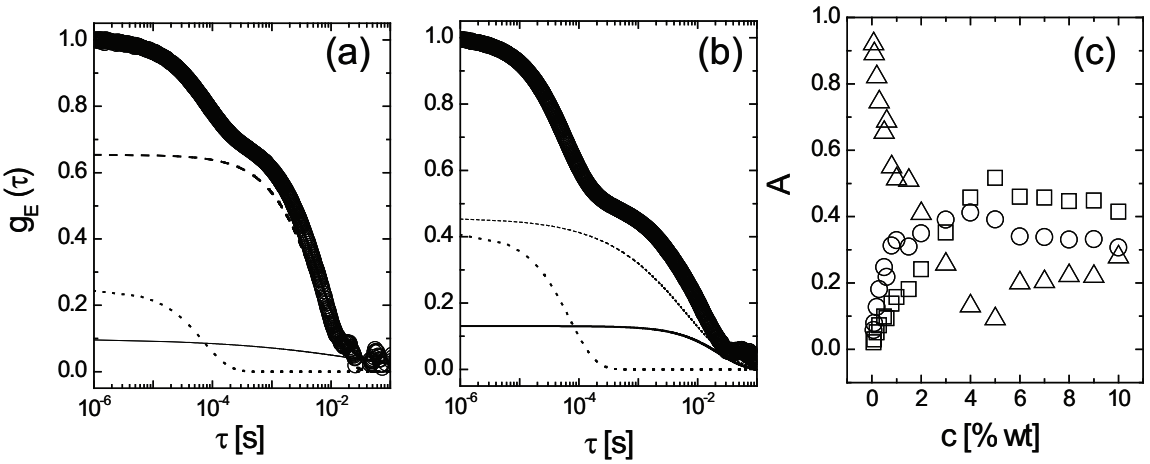

Figure 27: Electric field correlation function for a VP microgel with 0.5 weight% DVB, measured at pH=3.0 in the presence of certain dextran concentration: (a) c=0.5%, (b) c=4%. Experimental fit of the data based on the superposition of three exponential functions (solid line) corresponding to the fast (dot line) and slow (dash line) modes of the dextran solution and to the diffusion of the microgel particles (dash-dot line). (c) Amplitude of the different modes as a function of c: (○) dextran fast mode, (□) dextran slow mode, (△) microgel. Note that for c>2%, the amplitudes corresponding to the dextran modes are higher than that associated to microgel diffusion.

particles can be extracted from the light scattering data.

For particles with higher amount of cross-linker, the maximum dextran concentration below which the microgel contribution to $g_E(\tau)$ is dominant noticeably increases. In these cases, the microgels do not swell as much and the optical contrast of the samples is larger. As a result, $A_{mgel} > A_{slow}$ for all dextran concentrations, as shown in Fig. 28, where we also plot representative $g_1(\tau)$ for c = 2% and c = 10% together with the individual and overall contributions to Eq. 47.

3.2.6 Particle bulk modulus determination

From the relaxation frequencies associated to the microgel mode, Γ_{mgel}, we can determine the diffusion coefficient of the microgel particles and, with Eq. 27, the particle size, as a function of dextran concentration. Since, in addition, we know the osmotic pressure for a given c, we can determine the dependence of the particle size with

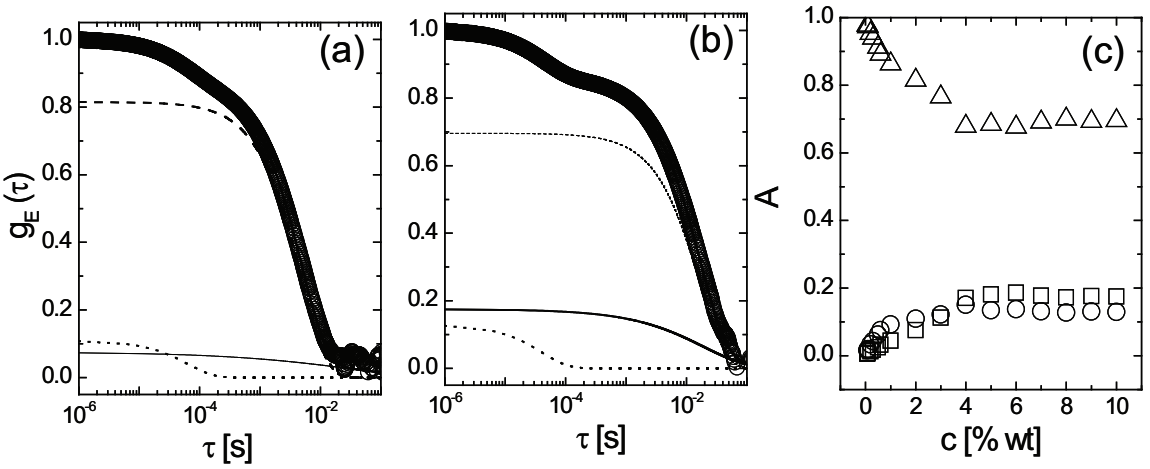

Figure 28: Electric field correlation function for a VP microgel with 1.3 weight% DVB, measured at pH=3.0 in the presence of certain dextran concentration: (a) c=2%, (b) c=10%. Experimental fit of the data based on the superposition of three exponential functions (solid line) corresponding to the fast (dot line) and slow (dash line) modes of the dextran solution and to the diffusion of the microgel particles (dash-dot line). (c) Amplitude of the different modes as a function of c: (∘) dextran fast mode, (□) dextran slow mode, (△) microgel.

osmotic pressure.

For low osmotic pressures, the particle size remains essentially constant with Π_{ext}. This regime corresponds to external osmotic pressures smaller than the particle bulk modulus [92]. However, above a certain Π_{ext}, the particles begin to de-swell, as shown in Fig. 29a. This indicates negligible penetration of dextrans inside the microgel particles. Otherwise no deswelling and even particle swelling would occur [110]. The particular value of Π_{ext} for which this happens depends on the amount of cross-linker; it increases with cross-linker concentration as a result of the corresponding increase in particle stiffness. Note that for the VP microgels with 0.5% DVB, we do not plot data for $c > 2\%$, since for these concentrations the slow mode of the dextrans dominates over the microgel mode preventing the obtention of reliable data for the microgel particles. In addition, we do not consider dextran concentrations above 10%, as in these situations depletion-flocculation of the microgels prevent the determination of the particle size [85].

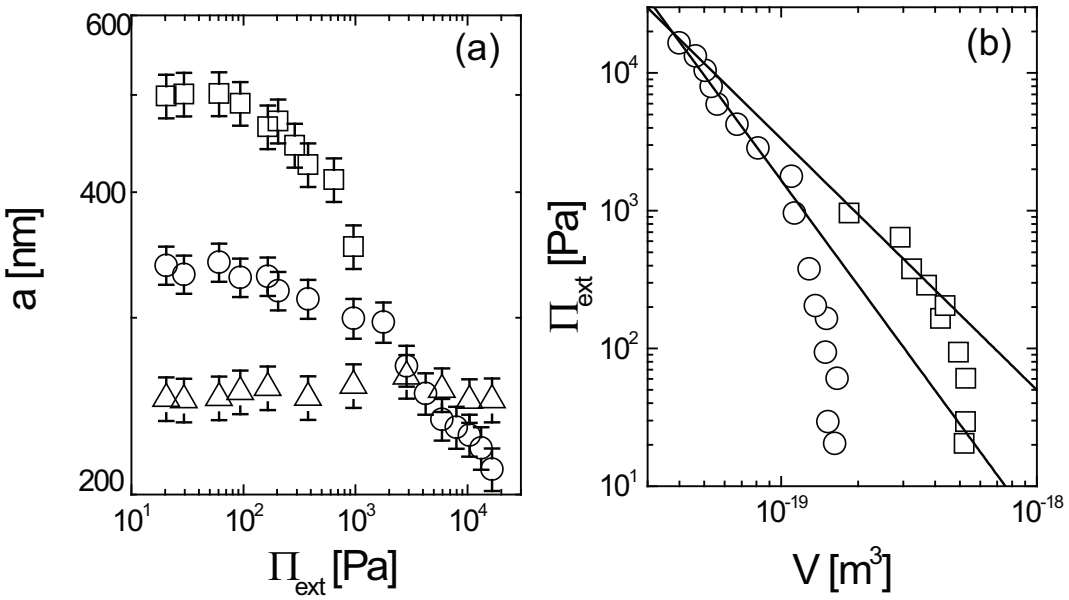

Figure 29: a) Deswelling behavior of VP microgels in terms of the size as a function of the external osmotic pressure: (□) 0.5%, (○) 1.3%, (◊) 3.5%. b) Log-Log plot of osmotic pressure versus particle volume; from the linear region we determine the bulk modulus of the particles

From Fig. 29a we can obtain the bulk modulus of the particles. We replot the data in terms of the particle volume and use the slope of the Π_{ext} - V_{1p} relationship right above the Π_{ext} where osmotic de-swelling begins, as shown in Fig. 29b. We obtain K = (400± 20) Pa for the microgel with 0.5% DVB and K = (1.6± 0.1)·10^3 Pa for the microgel with 1.3% DVB. As expected, increasing the cross-linker concentration results in a higher bulk modulus and thus in a higher resistance to compression. We have also performed experiments with VP microgels with 3.5% of DVB. However, in this case, K is so high that de-swelling does not happen within the dextran concentration range where depletion-flocculation is absent. As a result, the particle size is constant irrespective of Π_{ext}, as shown in Fig. 29a.

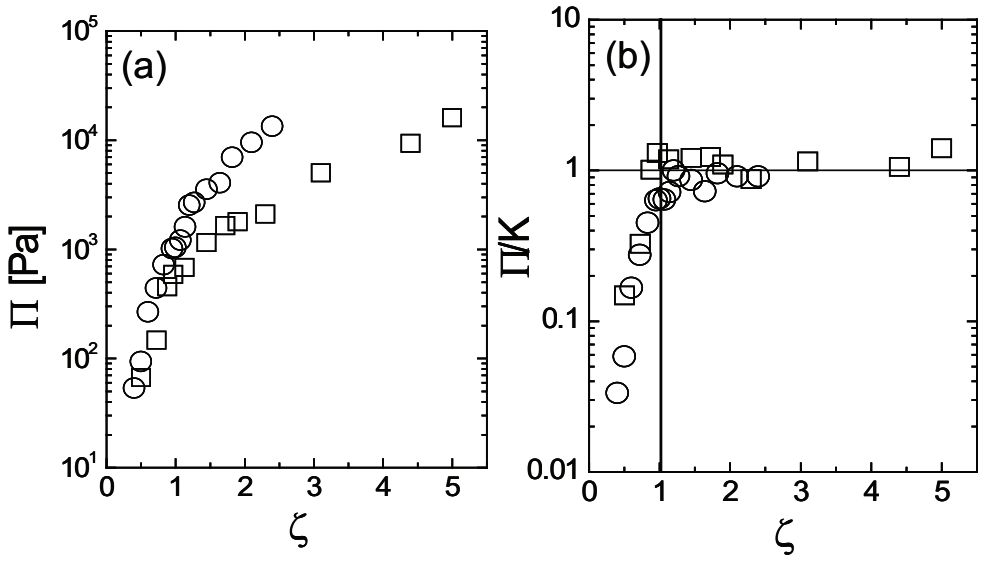

Figure 30: a) Osmotic pressure versus ζ for VP microgels: (□) 0.5%, (○) 1.3%. b) Osmotic pressure normalized by the particle bulk modulus K. When $\zeta \approx 1$, $\Pi/K \approx 1$.

3.3 Osmotic pressure of microgel suspensions.

We measure the suspension osmotic pressure for the microgel with 0.5% DVB and the microgel with 1.3% DVB and find it increases monotonically with ζ, as shown in Fig.30a. We then normalize Π with the particle bulk modulus, and identify $\zeta \approx 1$ as the volume fraction where $\Pi \approx K$, as shown in Fig.30b. This implies that particle deswelling cannot take place before the particles physically start to touch each other, provided ζ is a good measure of the particle volume fraction. To address this, we quantify the phase behavior of the samples and look for the ζ corresponding to the transition from a liquid to a solid phase. For the sample based on microgels with 0.5% DVB, the behavior is similar to that described in Chapter 2 for the microgels with 0.2% DVB; the sample is liquid-like at all accesible ζ. As a result, it is hard to identify the ζ where the particles jam. For the samples based on microgels with 1.3% DVB, the situation is different. As for the other samples, there is no signature of crystal phases. This is inferred by the lack of Bragg reflections in the samples as shown in Fig.31. However, the rheology of this system clearly shows a liquid-to-solid

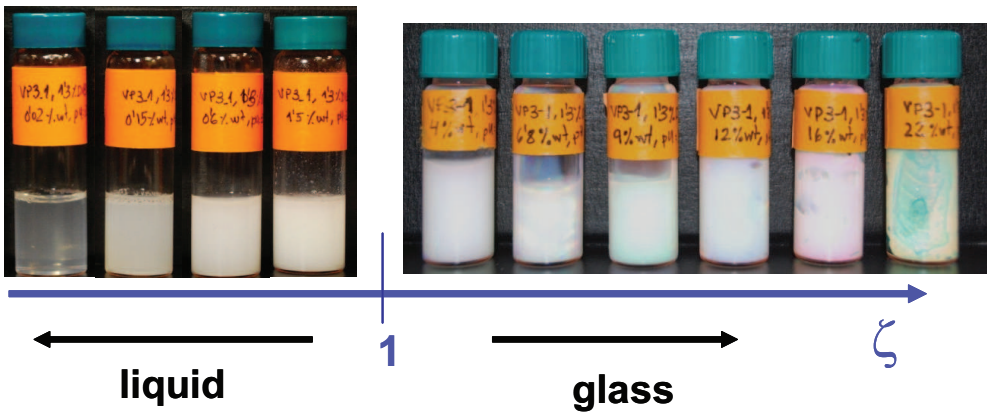

Figure 31: Phase behavior of the VP-1.3% system. The system lacks a crystalline phase: For $\zeta < 1$ it is a liquid whereas for $\zeta > 1$ the system is a glass.

transition at $\zeta \approx 1$. This correspond to the formation of a glass and confirms that no deswelling happens for liquid-like suspensions. As a result, no deswelling is possible at low volume fractions, like $\phi \approx 0.3$, as the suspension osmotic pressure is lower than K in these situations. Similarly to emulsions, only when the particles touch at $\sim \phi_{rcp}$ can deformation begin. While for droplets this reflects in shape changes, for microgels this include both shape and volume changes.

Let us examine the rheology mentioned above carefully. We do this at a pH of 3, for fully swollen particles using a cone-plate geometry operated in oscillatory mode, in the linear regime. For ζ <1, G"$>$G' over the full experimentally accesible range of angular frequencies and $G'' \sim \omega$, as expected for a viscous fluid, as shown in Fig.32a. By contrast, for $\zeta \geq 1$, the behavior dramatically changes. The system clearly exhibits solid behavior with a dominant G' over most of the angular frequency range, as shown in Fig.32b. In fact, as ζ increases, G' becomes almost independent of ω. Concomitantly, G" develops a clear minimum, which is a hallmark of a relaxation process due to structural rearrangements of the particles in a glassy state, as seen in emulsions [61, 100] and other colloidal systems [112].

Interestingly, the dependence of the elastic plateau modulus, G'_p, the minimum of the loss modulus, G''_m and the osmotic pressure, Π with ζ is very similar, as

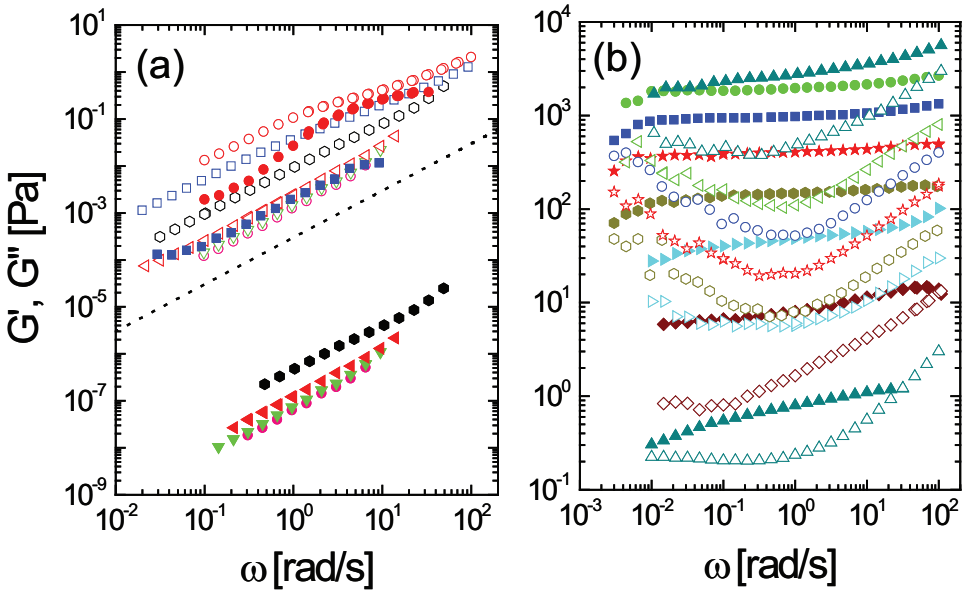

Figure 32: Storage (G' - Closed Symbols) and Loss (G"- Open symbols) moduli for VP suspensions at different ζ: a) ($\circ$) $\zeta = 0.027$, ($\triangledown$) ζ =0.08, ($\triangleleft$) $\zeta = 0.18$,($\circ$) $\zeta = 0.38$, ($\square$) $\zeta = 0.6$, ($\circ$) $\zeta = 0.78$. b)($\triangle$) $\zeta = 1.02$, ($\diamond$) $\zeta = 1.8$, ($\triangleright$) $\zeta = 2.4$, ($\circ$) $\zeta = 4.09$, ($\star$) $\zeta = 5.41$, ($\square$) $\zeta = 7.21$, ($\circ$) $\zeta = 9.61$, ($\triangle$) $\zeta = 18.33$

shown in Fig.33, where we also plot the compressional modulus of the suspension, $K_s = \zeta \frac{d\Pi}{d\zeta}$. We normalize these quantities with the particle bulk modulus, which sets the relevant elastic energy density scale [113]. We observe that the osmotic pressure and the compressional modulus of the suspension normalized by K increase below $\zeta \approx 1$ and remain constant with ζ for $\zeta > 1$. In this region, the suspension develop a measurable G'_p and G''_m, which also remain essentially flat with ζ when normalized by K, consistent with the trend of Π and K_s. Qualitatively, a similar phenomenology has been observed with emulsions at volume fractions larger than ϕ_{rcp} [61]. In this case, the droplets deform and form facets in the contact region between drops. These facets can be thought of as springs that are more or less compressed depending on the deformation of the drops. The compressed emulsion is within this picture equivalent to a network of compressed springs. The application of a shear stress can thus be thought of changing the compression state of these springs. As a result, for emulsions above ϕ_{rcp}, the osmotic pressure coincides with the emulsion elastic plateau modulus.

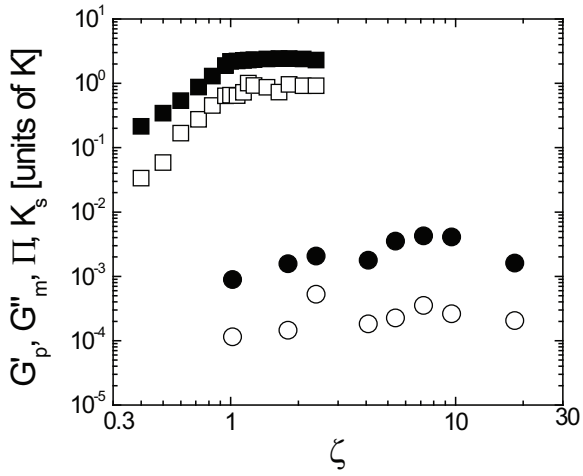

Figure 33: Volume fraction dependence of G'$_p$ (closed circles), G"$_m$ (open circles), Π (open squares) and compressional modulus (closed squares), K_s normalized by the particle bulk modulus, K, for VP-1.3%.

However, for microgels this is not the case. While the normalized osmotic pressure and elastic plateau modulus exhibit the same trend for $\zeta \geq 1$, Π is orders of magnitude larger than G'$_p$. This reflects the differences in response expected for shear or compression of a packed microgel suspension. To account for this difference, we model a microgel by a set of springs that are distributed throughout the particle. All these springs participate against the compression of a packed microgel suspension. However, only those in the periphery of the particles, in contact with other particles, participate against a shear deformation. As a result, $\Pi \gg G'_p$. In emulsions, the liquid drops are essentially incompressible and the number of springs participating in either a compression or a shear deformation is identical. As a result, $\Pi = G'_p$

From the disparity between K_s and G'_p we can estimate the volume of the peripheral region of the particles participating against a shear deformation compared to the microgel volume:

$$\frac{V_{1p}}{V_{1s}} \approx K_s/G'_p \tag{48}$$

where $V_{1s} = \frac{4\pi}{3}(a^3 - a'^3)$ is the volume of the outermost shell in which the springs

contributing to shear concentrate, with a and a' the particle and the void sizes respectively. Since $\mathrm{K}_s/G'_p \sim 550$ from Fig.33, we obtain $a' = 0.9994\ a$. This estimation implicitly assumes that the cross-linker distribution and hence distribution of springs within the particle is uniform. This is, however, not often the case and crosslinker concentration decreases from the center towards the periphery of the particles [93]. For weakly crosslinked VP microgels, this decay was suggested to be exponential [114]. As a result, the effective rim in which the springs concentrate will be larger. Nevertheless, our results confirm that the springs participating against a shear deformation are much less than those participating against compression.

The large difference between K_s and G'_p for packed microgel suspensions results from their internal degrees of freedom, which are absent for emulsions drops or solid particles. However, the proportionality between these two quantities is common to all materials. In fact, the friction force, $\mathbf{f}$, between solid macroscopic objects is proportional to the normal force, $\mathbf{N}$, with the proportionality constant the friction coefficient, μ, which takes values between 0.2 and 0.4 depending on the materials. Despite this, $\mathbf{f} < \mathbf{N}$, reflecting that is harder to compress than to shear. In microgel suspensions, this difference is exaggerated given the large number of internal degrees of freedom of these particles and hence, the larger number of springs participating against compression compared to the number of springs participating against shear.

CHAPTER IV

THE EFFECT OF HYDROSTATIC PRESSURE OVER THE SWELLING EQUILIBRIUM OF MICROGEL PARTICLES

Among microgel particles, those based on N-Isopropylacrilamide are the most widely used perhaps because they are thermo-responsive and temperature changes are usually easy and convenient to achieve by means of a recirculation bath or a peltier plate. Since they were first synthesized by Pelton and Chibante in 1986 [115], they have been used as main systems for a wealth of different applications [35, 36, 37, 39, 40, 42, 43, 45] as well as to elucidate fundamental questions in condensed matter physics [51, 52, 53, 54, 55, 56]. In all these situations, the ability of the microgel particles to change their volume in response to changes in the external temperature is used, in on one or other way. From a physical point of view, this volume phase transition can be seen as a balance between an elastic stress resulting from the presence of cross-link molecules in the microgel network, and a mixing contribution related to the interaction between the polymer and the solvent molecules, with unfavoring mixing in these systems.

An alternative to the use of temperature relies on using of hydrostatic pressure. It has been shown for macroscopic gels [116, 117, 118, 119, 120] that hydrostatic pressure changes the polymer-solvent affinity in a manner similar to temperature. However, hydrostatic pressure changes can be achieved homogeneously and faster than temperature changes, which is very convenient for changing the system volume fraction. In addition to its evident fundamental interest, understanding the effect of hydrostatic pressure could be of interest in applications like oil recovery, where the

microgel particles are used as shear thickeners. Given they are pumped deep into the ground suspended in water, there are large pressures involved that could lead to size changes which should be understood and taken into account.

In this Chapter, we will characterize the size dependence of NIPAM microgel particles as a function of temperature and hydrostatic pressure and show that their effects over particle swelling is very similar. We will start reviewing the fundamental thermodynamic considerations of the volume phase transition in microgel particles. We will explicitly address the mathematic form of the mixing, the elastic and the ionic interactions to the overall swelling behavior of the particles. These contributions can be all summarized into a net osmotic pressure acting over the particle, which is zero in equilibrium. We will then study the influence of temperature over the swelling behavior of the particles. We will rationalize the experimental results using thermodynamics and experimentally measure the dependence of the solvency parameter with temperature. The central part of the chapter will be dedicated to size measurements versus hydrostatic pressure. By establishing that each particle size corresponds to a certain value of the solvency parameter, the dependence of the latter can be obtained as a function of hydrostatic pressure; this has never been done before for this type of systems. We observe that the solvency parameter increases with hydrostatic pressure consistent with the decrease in the particle size. We interpret this behavior in terms of the entropy change of the mixture, which we find increases with pressure, consistent with results for other polymer and gel systems [121, 122, 123, 124]. Interestingly, despite both temperature and pressure equally affect the system by increasing the solvency parameter, they do so in a different way. Changes in particle size are more continuous when achieved with hydrostatic pressure, an interesting fact if a fine tuning of the particle size is desired.

4.1 Swelling Thermodynamics

4.1.1 Free energy of mixing

Thermodynamically, a microgel particle can be treated as a mixture of polymer chains in a solvent. In order to study its miscibility it is useful to invoke a lattice model in which n_2 polymer chains, each made of x segments, are mixed with n_1 solvent molecules in a lattice with a total number of sites $n_0 = n_1 + xn_2$ [47]. The entropy of the mixture depends on the number of configurations (microstates) that the polymer can adopt, Ω_{mix}, through the Boltzman law:

$$S_{mix} = k_b \ \ln \Omega_{mix} \tag{49}$$

By substracting the entropy of the polymer in its pure state, we obtain the change in entropy due to mixing [47, 125]:

$$\Delta S_{mix} = -k_b(n_1 \ \ln \phi_1 + n_2 \ \ln \phi_2) \tag{50}$$

with ϕ_1 and ϕ_2 the volume fraction of solvent and polymer, respectively. Note that ΔS_{mix} is always positive since, by mixing with the solvent, the polymer increases the available number of configurations. Therefore, the process of mixing is always, entropically favored.

However, there are also polymer-solvent molecule interactions that must be considered. The nature of this interaction is typically short-ranged [126, 127] and, thus, only interactions between neighbor sites in the lattice need to be considered.

Mixing implies the break-up of polymer-polymer and solvent-solvent bonds to form polymer-solvent bonds. If we denote e_{pp}, e_{ss} and e_{ps} as the bond energies between two polymer contacts, two solvent contacts and a polymer-solvent contact respectively, the energetic change when a polymer-solvent bond forms is $\Delta e = e_{ps} - \frac{e_{pp}+e_{ss}}{2}$. The change in the internal energy of the polymer solution due to mixing can then be written as $\Delta U_{mix} = P_{12}\Delta e$, with P_{12} the number of possible polymer-solvent contacts,

which depends on the probability of having a polymer chain in contact with a solvent molecule. By evaluating this probability, we obtain [47]:

$$\Delta U_{mix} = k_b T \chi_1 n_1 \phi_2 \tag{51}$$

where χ_1 is called the Flory solvency parameter defined as $\chi_1 = \frac{z\Delta e}{k_b T}$, with z the coordination number of a lattice site. χ_1 can be interpreted as the energy change of a polymer molecule when introduced in a pure solvent solution. Note that Δe also contains an entropic contribution arising from the mixing process that can be taken into account taking Δe as a free energy. In this way, we can rewrite the definition of the Flory parameter as:

$$\chi_1 = \frac{z\Delta e}{k_b T} = \frac{z\Delta e_e}{k_b T} - \frac{z\Delta e_s}{k_b} \tag{52}$$

From ΔU_{mix} and ΔS_{mix}, we calculate the Helmholtz free energy, considering that T is constant during the mixing process [128]:

$$\Delta F_{mix} = \Delta U_{mix} - T\Delta S_{mix} = k_b T(n_1 \ln \phi_1 + n_2 \ln \phi_2 + \chi_1 n_1 \phi_2) \tag{53}$$

However, since the process is usually isobaric and essentially isochoric [125], the change in the Helmholtz free energy equals the change in the Gibbs free energy, $\Delta F_{mix} = \Delta G_{mix}$.

After mixing, if we were to equilibrate the polymer solution with a pure solvent solution an extra pressure would be necessary. This pressure was first noticed by Pfeffer in 1877 doing experiments with sugar solutions [129]. He observed that after putting the solutions in contact with pure water through a permeable membrane, the pressure in the sugar solution rose. He measured the extra pressure, which we call the osmotic pressure, using a mercury barometer.

After equilibration, the chemical potential of a solvent molecule in the polymer solution, $\mu_1(P+\Pi, T)$, equals the chemical potential of a solvent molecule in the pure solvent, $\mu_1(P, T)$:

$$\mu_1^{pure}(P, T) = \mu_1(P + \Pi, T) \tag{54}$$

Using the excess chemical potential, $\Delta\mu_1$ [77]:

$$\mu_1(P+\Pi,T) = \mu_1^{pure}(P+\Pi,T) + \Delta\mu_1 \tag{55}$$

In addition, we can approximate $\mu_1^{pure}(P+\Pi,T)$ by its first order Taylor expansion to obtain:

$$\mu_1^{pure}(P+\Pi,T) = \mu_1^{pure}(P,T) + \int_P^{P+\Pi} \frac{\partial \mu_1^{pure}}{\partial P'} dP' = \mu_1^{pure}(P,T) + v_s\Pi \tag{56}$$

where we have used the Gibbs-Duhem relation $Nd\mu = -SdT + VdP$ and $\frac{\partial\mu}{\partial P} = v_s$, with v_s the volume of a solvent molecule.

By combining the above equations, we obtain the usual definition for the osmotic pressure:

$$\Pi = -\frac{\Delta\mu_1}{v_s} \tag{57}$$

which we can further evaluate using the definition of μ in terms of the Gibbs free energy, $\mu_1 = (\frac{\partial G}{\partial n_1})_{T,P,n_{j\neq 1}}$. The result is:

$$\Pi_{mix} = -\frac{1}{v_s}(\frac{\partial \Delta G}{\partial n_1})_{T,P,n_{j\neq 1}} = \frac{k_bT}{v_s}[\phi_2 + \ln(1-\phi_2) + \chi\phi_2^2] \tag{58}$$

where we have used Eq.53 and 57 and considered that the polymer solution is dilute: $n_1 >> n_2$ and, thus $n_2\ln(\phi_2) < n_1\ln(1-\phi_2)$.

4.1.2 Elastic Free Energy

One of the main characteristic of chemical gels is the presence of randomly distributed crosslinker molecules throughout the network resulting in resistance to deformation. Thus, the elasticity of microgel particles influences their ability to swell under the appropriate circumstances. If a linear deformation, dL, is induced by means of a force f_l applied to a polymer chain, the induced change in the Helmholtz free energy can be written as [128]:

$$dF = SdT + PdV + f_l dL \tag{59}$$

with $f_l = (\frac{\partial F}{\partial L})_{T,V} = [\frac{\partial (U-TS)}{\partial L}]_{T,V} = (\frac{\partial U}{\partial L})_{T,V} - T(\frac{\partial S}{\partial L})_{T,V}$. By measuring the restoring force as a function of temperature and determining the offset and the slope, it is empirically known that the main contribution to the restoring force is of entropic nature [125]. This type of chains are usually called ideal chains

In order to treat the deformation of the whole network, we will consider the affine approximation and assume that each chain is deformed as much as the whole network. We thus model our network as a collection of polymer chains, with a Gaussian-distributed set of end-to-end displacement vectors, $\vec{r}_{c,i}$. This implicity assumes that the chains are flexible and can be described with a random walk model [130].

If a deformation is now imposed on the system, the end-to-end displacement vectors change from $\vec{r}_{c,i}(\frac{x_{c,i}}{\alpha_x}, \frac{y_{c,i}}{\alpha_y}, \frac{z_{c,i}}{\alpha_z})$ to $\vec{r}_{c,i}(x_{c,i}, y_{c,i}, z_{c,i})$, with α_k the deformation ratio along the k-direction. The entropy change is calculated as the difference between the entropy of the deformed state and the entropy of the undeformed state using the Boltzmann formula $S = k_b \ln \Omega_{el}$, with Ω_{el} the number of microstates compatible with the distribution of end-to-end displacement vectors, $\vec{r}_{c,i}$. This calculation was performed by Flory and Rhener [131, 132] and results in:

$$\Delta S_{el} = -\frac{k_b N_c}{2}[\alpha_x^2 + \alpha_y^2 + \alpha_z^2 - 3 - \ln(\alpha_x \alpha_y \alpha_z)] \tag{60}$$

with N_c the number of chains. The undeformed state corresponds to the state of the system when it is synthesized and thus under the presence of no deformation. For microgel particles, this is usually the deswollen state since most microgels are synthesized in these conditions.

The Helmholtz free energy is calculated as $\Delta F_{el} = -T\Delta S_{el}$ since there is no energy term involved. Since, as in the case of mixing, the process is usually isobaric and essentially isochoric [125], the change in the Helmholtz free energy equals the change in the Gibbs free energy, $\Delta F_{el} = \Delta G_{el}$.

In most situations, the swelling of the network occurs homogeneously and thus, $\alpha_x = \alpha_y = \alpha_z = \alpha = (\frac{V}{V_0})^{1/3}$, with V and V_0 the volume in the deformed and

underformed states. Using this result and the definition of the osmotic pressure, Eq. 57; we obtain the elastic osmotic pressure:

$$\Pi_{el} = \frac{-1}{v_s}(\frac{\partial \Delta G_{el}}{\partial \alpha})_{T,P,n_{j\neq 1}}(\frac{\partial \alpha}{\partial n_1})_{T,P,n_{j\neq 1}} = \frac{k_b T N_c}{V_0}[\frac{\phi_2}{2\phi_{2,0}} - (\frac{\phi_2}{\phi_{2,0}})^{1/3}] \qquad (61)$$

where $\phi_{2,0}$ is the polymer volume fraction in the undeformed state.

4.1.3 Ionic contribution

For the case of ionic microgels, the fixed charge of the polymer network can be used to induce swelling. As it turns out, the major role of this charge is to create a Donnan potential inside the particle that affects the ionic distributions. This, in turn, generates an osmotic pressure difference between the inside and outside of the particle, causing either its swelling or de-swelling. Direct electrostatic interactions do not play a major role in this process, provided the distribution of fixed charge within the particle is reasonably homogenous [50]. The main contribution to the osmotic pressure thus results from the confined counterions which are present in the system to preserve electroneutrality. This contribution is usually treated considering the counterions as an ideal gas.

If we define a microgel as a particle of radius R, with N monomers between cross-link points and an average end-to-end distance of the chain, r_c, then the concentration of monomer within the particle is defined as $c = N/r_c^3$. If we now assume that f is the fraction of monomers that are charged, then the number of counterions will be $fcV = fNN_c$, where $V \approx R^3$ is the volume of the particle.

Assuming an ideal gas model for the counterions, there is no spatial correlation between the ionic species and thus, the only contribution to the free energy is of entropic nature, which, in turn, is related to the number of ways, Ω_{ionic}, to distribute fNN_c counterions inside the gel. Since there is no interaction between the counterions, the total number of possibilities to distribute all counterions is equal to the product of the number of possibilities for each counterion and, thus $\Omega_{ionic} \approx V^{fNN_c}$.

Therefore the entropy change associated to the counterions is:

$$\Delta S_{ionic} = k_b \ln \Omega_{ionic} = k_b f N N_c \ln V \tag{62}$$

and the change in the Gibbs free energy is calculated as $\Delta G_{ionic} = -T\Delta S_{ionic} = -k_b T f N N_c \ln V$.

From the Gibbs free energy, the change in the chemical potential of the solvent in a solution with counterions can be calculated in the usual way:

$$\Delta\mu_1 = (\frac{\partial \Delta G_{ionic}}{\partial n_1})_{T,P,n_{j\neq 1}} = -k_b T f N N_c \frac{v_s}{V} \tag{63}$$

where we have implicitly used that v_s is constant and that the particle volume V is the sum of the total volume of solvent, counterions and polymer segments.

Therefore, the additional osmotic pressure due to the ions can be written as:

$$\Pi_{ionic} = -\frac{\Delta\mu_1}{v_s} = k_b T f c \tag{64}$$

This is the Van't Hoff's expression for the osmotic pressure. It appears frequently in the context of solutions when treated ideally and is analogous to the pressure exerted by and ideal gas.

Up to this point, we have implicitly considered that the presence of counterions only arises from the dissociation of the chemical groups in the polyelectrolyte chains. In some situations, however, the solvent contains a finite concentration of salt, n. If we denote n_{in} as the concentration of salt inside the particle, the total concentration of counterions inside the particle is $fc + n_{in}$ while the concentration of coions inside the particle is n_{in}. In order to calculate the osmotic pressure difference between the inside and the outside of the particle, we will treat each specie as ideal gases and use Eq.64 for the osmotic pressure exerted by each specie. Then:

$$\Delta\Pi = \Pi_{in} - \Pi_{out} = k_b T \sum_i (n_i - n_i^o) = k_b T (fc + n_{in} + n_{in} - 2n) \tag{65}$$

where n_i and n_i^o are the concentrations of the i-th ionic specie inside and outside the particle, respectively, and where we have considered that $n^o = 2n$, i.e. the amount of salt that goes inside the particle is small compared with the total salt concentration.

The amount of salt inside the particle can be calculated from considering that, in equilibrium, the sum of the chemical potential of the ionic species should be the same outside and inside the particle. As a result,

$$\mu_{counter,in} + \mu_{coion,in} = \mu_{counter,out} + \mu_{coion,out} \tag{66}$$

where the chemical potential of the ions is calculated using the ideal gas approximation, $\mu_{ion} = (\frac{\partial G_{ionic}}{\partial N_{ion}})_{T,P,n} = k_b T \ln c_{ion} + \mu_0$, with N_{ion} and c_{ion} the number and concentration of the ionic specie. Using Eq.66, we arrive at $n^2 = n_{in}(fc + n_{in})$, which can be rewritten as:

$$n_{in} = \frac{-fc + \sqrt{(fc)^2 + 4n^2}}{2} \tag{67}$$

Substituting this expression into Eq.65, we obtain the osmotic pressure as a function of the counterion concentration and the added salt concentration:

$$\Delta\Pi = k_b T(\sqrt{(fc)^2 + 4n^2} - 2n) \tag{68}$$

This expression can be simplified for $fc << n$. Then, equation 68 becomes:

$$\Delta\Pi = k_b T \frac{f^2 c^2}{4n} \tag{69}$$

which corresponds to the expression often used to describe the ionic contribution to the overall osmotic pressure of charged microgels in the presence of added salt. Note that the osmotic pressure difference between the inside and the outside of the particle decreases as the salt concentration increases. Thus, at high amounts of added salt, the ionic microgel is expected to behave essentially as a neutral microgel with the ionic contribution playing a negligible role.

Summing up all the contributions, we obtain the total osmotic pressure:

$$\Pi = \Pi_{mix} + \Pi_{el} + \Pi_{ionic} = \frac{k_b T}{v_s}[\phi_2 + \ln(1-\phi_2) + \chi\phi_2^2] + \frac{k_b T N_c}{V_0}[\frac{\phi_2}{2\phi_{2,0}} - (\frac{\phi_2}{\phi_{2,0}})^{1/3}] + k_b T f c \quad (70)$$

Interestingly, the osmotic pressure behavior with polymer volume fraction is similar to the pressure behavior with volume in atomic fluids, with the Flory parameter playing the role of temperature. To emphasize this analogy, we consider the virial expansion of Eq.70, which we can derive by Taylor expanding the logarithmic term for small ϕ_2:

$$\Pi = \frac{k_b T N_a}{v_s}[\frac{N_c v s}{V_0 N_a}[(fN + \frac{1}{2})(\frac{\phi_2}{\phi_{2,0}}) - (\frac{\phi_2}{\phi_{2,0}})^{1/3}] + (\frac{1}{2} - \chi)\phi_2^2 + \frac{\phi_2^3}{3} + ...] \quad (71)$$

By further introducing a reduced polymer volume fraction, $\rho = \frac{\phi_2}{\phi_{2,0}}$ and defining $A = \frac{2\Delta S + k_b}{2k_b}$, $\Theta = \frac{2\Delta H}{k_b + 2\Delta S}$ and $\chi = \frac{1}{2} - A(1 - \frac{\Theta}{T})$ we can rewrite this equation as:

$$\Pi = \frac{k_b T N_a}{v_s}[-(\frac{N_c v s}{V_0 N_a}\rho^{1/3}) + \frac{N_c v s}{V_0 N_a}(fN + \frac{1}{2})\rho + A\phi_{2,0}^2(1 - \frac{\Theta}{T})\rho^2 + \frac{\phi_{2,0}^3}{3}\rho^3 + ...] \quad (72)$$

which is analogous to the virial expansion for a Van der Waals fluid:

$$P_r = T_r(\rho_r + \rho_r^2[1 - (\frac{1}{T_r})] + \rho_r^3) \quad (73)$$

where P_r, T_r and ρ_r are the reduced pressure. temperature and density of the fluid, respectively. In this analogy, swollen and deswollen microgel states would correspond to gas and liquid phases of a fluid. It is interesting to note that, for T=Θ, χ=1/2 and the second-virial coefficient vanishes. This temperature is called the Θ-temperature of the polymer-solvent system; it corresponds to the temperature where the chains behave as ideal chains[130].

4.2 Experimental System and Techniques

4.2.1 Experimental System

We use microgel particles based on NIPAM copolymerized with allylamine in water. The presence of allylamine increases the hydrophilicity of the system, hence promoting a better mixing with the solvent, as well as providing binding sites for particle functionalization with fluorescent dyes [133] or further step reactions [134].

The synthesis was carried out by an emulsion polymerization method, in which 3.845g of NIPAM monomer, 0.20g (10 % molar ratio) of allylamine monomer, 0.15g (2.5 % molar ratio) of methylenebis(acrylamide) cross-linker and 0.70g of sodium dodecyl sulfate surfactant were mixed with 230mL of deionized water in three round bottom flask. The solution is stirred at 300 rpm and heated up to 60^oC under an inert atmosphere, which is maintained by nitrogen bubbling. We then add 0.155 g of potassium persulfate to initiate the reaction, which was carried out for 5h at the same temperature. After cooling, the reaction products were filtrated and extensively dyalized against ultrapure water and finally, freeze-dried and redispersed in D_2O.

4.2.2 Experimental Set-up

In order to perform light scattering at high pressures, we use a pressure cell that enable achievement of pressures up to 500 MPa, and an in-house light scattering apparatus [135]. A vertically polarized He-Ne laser operating at a wavelength of 632.8nm impinges on the sample and the scattered light is collected at an angle of 135 degrees to avoid the multiple reflections from the pressure cell. The scattered light is passed through a vertical polarizer that filters out scrambled light from undesired reflections, guided through a single mode fiber to a beam splitter and finally coupled to two avalanche photodiodes that are used as detectors. The light is cross-correlated to avoid the after pulsing of the detectors [136] and an intensity correlation function is obtained. The intensity correlation function can be related to the field correlation

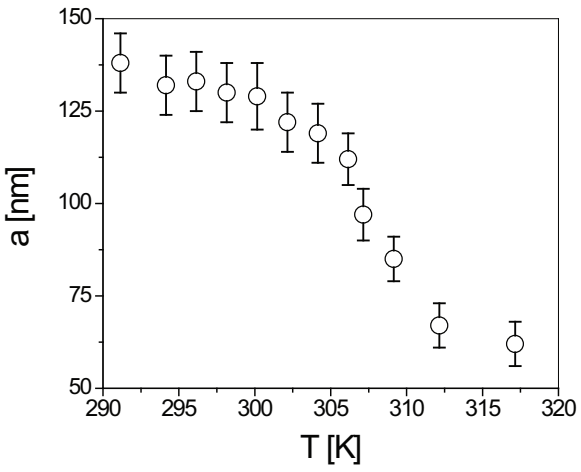

Figure 34: Particle radius dependence with temperature. As temperature increases, the particle deswells since mixing becomes increasingly unfavorable. The deswollen particle size, at high T, is $a_0 = 60$nm

function, which, for dilute samples, is well modeled by a single exponential with a relaxation frequency that depends on the diffusion coefficient of the scatterers. By using the Stokes-Einstein relation, a particle size can be obtained where we have used the the dependence of the viscosity with temperature and hydrostatic pressure. Refer to chapter 2 for further details.

4.3 Results and Discussion

4.3.1 Temperature dependence of the particle size

The swelling behavior of our microgel particles is characteristic of NIPAM-based microgels, which have Lower Critical Solution Temperature [137, 138, 139]. The particle deswells as the temperature is increased up to 312 K, where we reach a deswollen particle size of $a_0 = 60$nm, as shown in Fig. 34. Each point of this curve corresponds to an individual equilibrium state of the system at the particular experimental condition; therefore, the chemical potential inside and outside the particle is the same and, as a consequence, the net osmotic pressure is equal to zero. Since the microgels are neutral the only contributions to the net osmotic pressure results from the polymer-solvent

mixing (Eq.58), and from the presence of cross-linker (Eq.61). Therefore,

$$\Pi_{total} = \Pi_{mix} + \Pi_{el} = \frac{k_b T}{v_s}(\phi_2 + \ln(1-\phi_2) + \chi\phi_2^2) + \frac{k_b T N_c}{V_0}[\frac{\phi_2}{2\phi_{2,0}} - (\frac{\phi_2}{\phi_{2,0}})^{1/3}] \quad (74)$$

The equilibrium size of the particles is mainly determined by χ, provided the rest of the parameters remain constant. χ, in principle, only depends on temperature (Eq.71). However, it is empirically known that χ also displays a polymer concentration dependence, which is usually represented as a linear expansion in powers of ϕ_2 [140]:

$$\chi = \sum_{i=1} \chi_i \phi_2^{i-1} \quad (75)$$

where χ_1 is the Flory solvency parameter defined in Eq.71 and χ_i are empirical coefficients independent of temperature and polymer concentration.

With this consideration, we can fit our experimental results using a rearranged version of Eq.74:

$$T_{\Pi=0} = \frac{A\phi_2^2\Theta}{\frac{v_s N_c}{V_0}[\frac{\phi_2}{2\phi_{2,0}} - (\frac{\phi_2}{\phi_{2,0}})^{1/3}] - \phi_2 - \ln(1-\phi_2) + (A-\frac{1}{2})\phi_2^2 - \phi_2^2(\sum_{i=1}\chi_i\phi_2^{i-1})} \quad (76)$$

where we have used that $\phi_2/\phi_{2,0} = (a_0/a)^3$. Given that the volume fraction of polymer in the deswollen state is unknown we perform different fits for different values of $\phi_{2,0}$, leaving as free parameters N_c, A, Θ and χ_i since v_s is known and corresponds to the the volume of one molecule of D_2O, $3 \cdot 10^{-29}\mathrm{m}^3$. We find that the best fits, which minimize the statistical chi^2 value[141], are obtained when using a linear dependence of χ with $\phi_{2,0}$ in Eq.76. By restricting ourselves to this linear dependence we do not observe great statistical differences in chi^2 for different values of $\phi_{2,0}$. However, the values of the free parameters for each of the fits were markedly different as shown in Table 4.3.1. We thus also select the best fit by comparing the values of the free parameters with their known value, when possible. For instance, we can make an estimation of the number of chains in each microgel particle, recalling that a chain is defined as the amount of polymer between two cross-link molecules. Therefore,

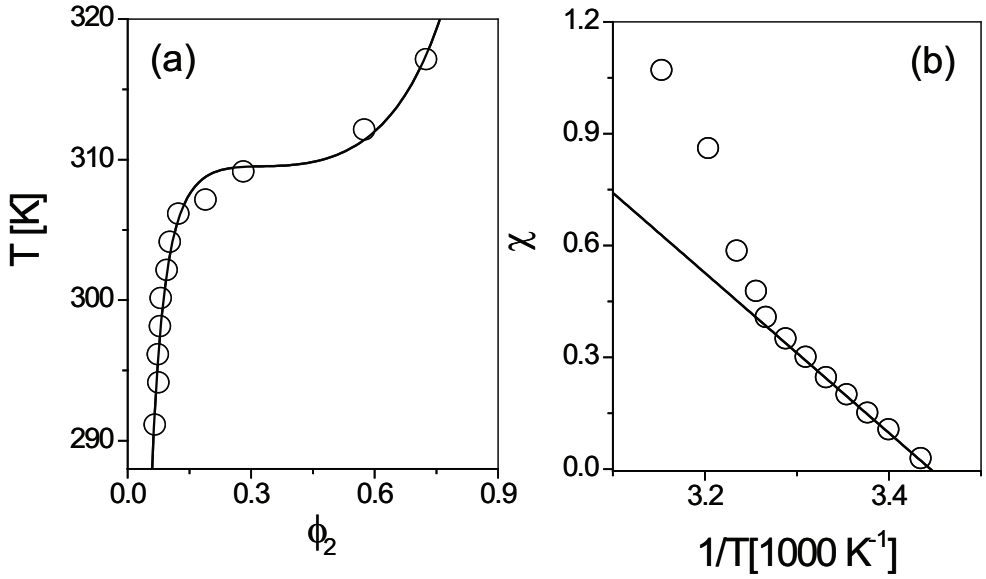

Figure 35: a) Volume phase transition induced by temperature. The solid line corresponds to the best fit with $\phi_{2,0} = 0.8$, $N_c = 1.75 \cdot 10^5$, A=-6.4, $\theta = 315$K and $\chi_1 = 0.72$. b) Dependence of the solvency parameter, χ, with inverse temperature as obtained from the experimental fit.

$N_c = 2N_aV_0c_{xlink}$, with N_a the Avogadro number, and c_{xlink} the concentration of cross-link molecules inside the particle, which we estimate from the particle synthesis. By doing this estimation, we obtain $N_c \approx 2.5\ 10^5$, which is close to the best fits obtained when $\phi_{2,0} = 0.8$ or $\phi_{2,0} = 0.85$, as shown in Table 4.3.1. In addition, the obtained values of ΔS, ΔH and χ_1 are in remarkable agreement with those previously reported for NIPAM-based macrogels [140] and microgel particles [121, 122, 142]. Therefore, the results for $\phi_{2,0} = 0.8$ and $\phi_{2,0} = 0.85$ are reasonable; Eq.76 describes well the experimental data and this is done with reasonable values of all the free parameters.

From the experimental size-temperature dependence and using Eq.75, we can plot the Flory parameter as a function of temperature as shown in Fig.35b. For high values of 1/T, the particles are fully swollen, the polymer volume fraction is very small and therefore, $\chi \approx \chi_1$; this is emphasized by the solid line in Fig.35b. By contrast, for T>Θ this linearity is lost since the ϕ-dependence of χ becomes important.

Table 1: Results of the Size-Temperature fits for different values of $\phi_{2,0}$

$\phi_{2,0}$	N_c	Θ (K)	A	χ_1	ΔS (10^{-23} J/K)	ΔH (10^{-20} J)
0.6	31350	316	-1.9	0.56	-3.36	-0.83
0.65	48838	316	-2.6	0.6	-4.27	-1.13
0.7	75128	315	-3.5	0.63	-5.49	-1.52
0.75	114780	315	-4.7	0.68	-7.16	-2.04
0.8	**175220**	**315**	**-6.4**	**0.72**	**-9.49**	**-2.77**
0.85	**269180**	**314**	**-8.8**	**0.78**	**-12.8**	**-3.82**
0.9	420080	314	-12.4	0.84	-17.8	-5.39
0.95	675730	314	-18.2	0.91	-25.9	-7.89

4.3.2 Dependence with Hydrostatic pressure

Whereas the dependence of the particle size with temperature has been extensively studied for microgels [121, 122, 142], its dependence with hydrostatic pressure has not been addressed so far. We find that the particles deswell with increasing P from a swollen radius of $\sim$ 130nm at P=0 to a deswollen radius of $a_0 = 60$nm at P>400MPa, as shown in Fig.36.

This behavior is qualitatively similar to what we observed for temperature, emphasizing the similar role played by both magnitudes in changing the miscibility of the polymer chains in the solvent. However, the swelling behavior seems more abrupt in the case of temperature as compared to the case of hydrostatic pressure. To quantify the observed similarities we assign a value of the mixing parameter χ at each hydrostatic pressure using the experimental size and the $\chi = \chi(T)$ relation found in the previous section; we identify the size at a certain P and T and assign a χ value using Fig.35b. This assumes none of the other variables change along the volume transition. By doing this, we find that the solvency parameter depends essentially linearly with hydrostatic pressure, as shown in Fig.37a. By performing a linear fit we find:

$$\chi = \chi'_0 + \chi'_1 P \tag{77}$$

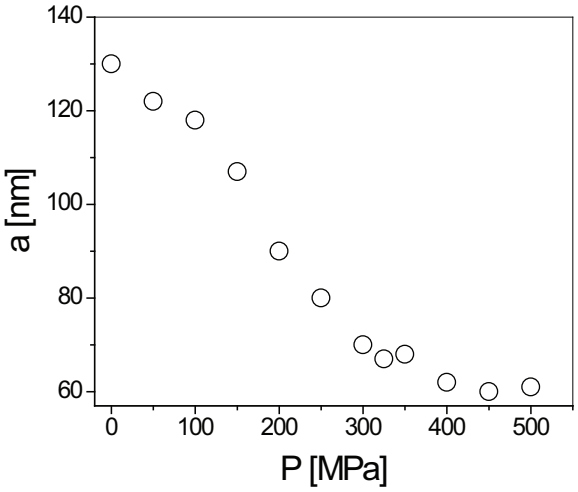

Figure 36: Particle radius as a function of hydrostatic pressure at constant temperature T=298K. Pressure acts in a similar manner as to temperature, deswelling the particle to a deswollen state, $a_0 = 60$nm

with $\chi_0' = 9.32 \cdot 10^{-2}$ and $\chi_1' = 2.29 \cdot 10^{-3}$ 1/MPa. Assuming this linear dependence, we can rearrange the equation of state (Eq.74) to include this $\chi = \chi(P)$ dependence, resulting in:

$$P_{\Pi=0} = \frac{\frac{v_s N_c}{V_0}[\frac{\phi_2}{2\phi_{2,0}} - (\frac{\phi_2}{\phi_{2,0}})^{1/3}] - \phi_2 - \ln(1-\phi_2) - \chi_0'}{\chi_1' \phi_2^2} \tag{78}$$

This equation can be used to fit our experimental data using the previously known values for N_c, v_s and ϕ_0 and leaving as free parameters χ_0' and χ_1' as shown in Fig.37b. Using this procedure, we obtain $\chi_0' = 9.3 \cdot 10^{-2}$ and $\chi_1' = 2.3 \cdot 10^{-3}$1/MPa, which are in good agreement with those obtained from the linear fit of χ with P. Furthermore, by comparing Eq. 77 and Eq.75, we expect that at room temperature, T=298K and zero applied pressure $\chi_0' = \chi_1 + \chi_2\phi_2$. As a result, $\chi_1 + \chi_2\phi_2 = 0.088$ for $\phi_{T=298K} = 0.079$ which is the volume fraction for $a = 130$nm, which is very close to χ_0' asserting the consistency of the experimental data.

To inquire about the χ-P relationship, we equate the Flory parameters given by Eqs.75 and 77 and hypothesize that the observed change in χ with P is related to the entropic change when a solvent-solvent contact is replaced by a polymer-solvent contact, since the enthalpy changes does not appreciable depend on external pressure

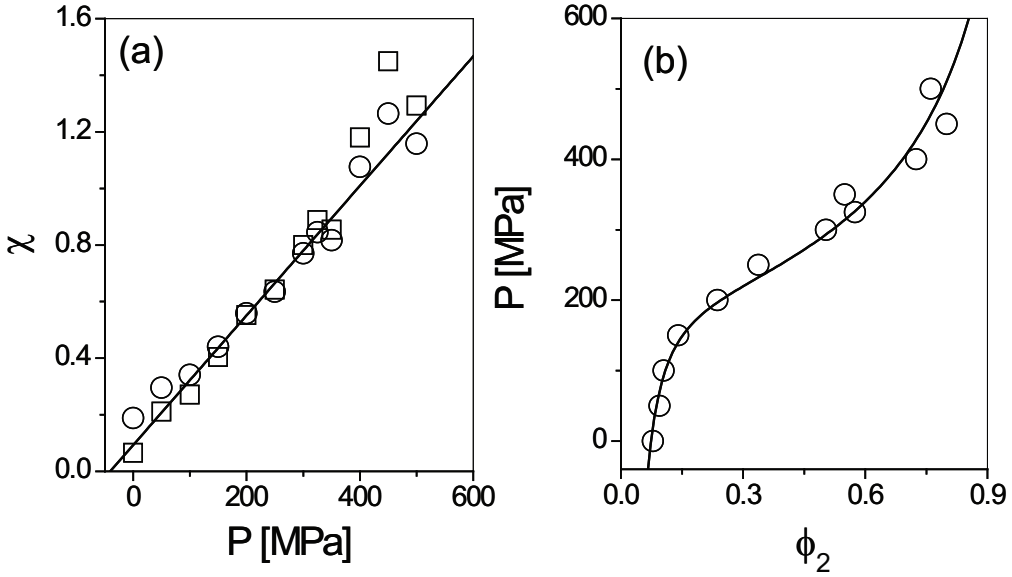

Figure 37: a)Dependence of the Flory parameter with hydrostatic pressure. The different sets of points are obtained using $\phi_0 = 0.8$ (circles) and $\phi_0 = 0.8$ (squares). b) Volume phase transition induced by hydrostatic pressure. The solid line shows the best fit using Eq.78 and values in Table.4.3.1

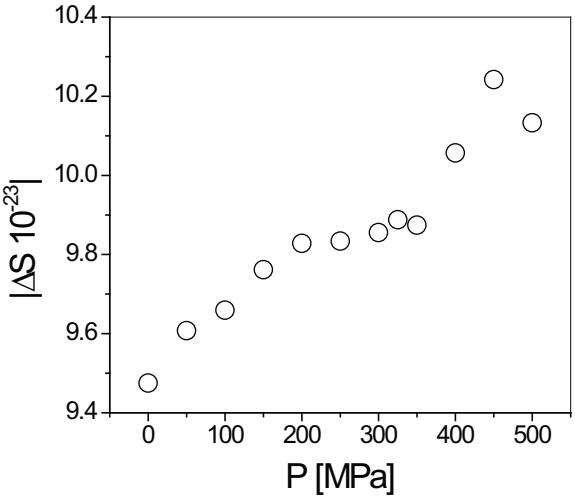

Figure 38: Absolute value of the change in the mixing entropy with hydrostatic pressure. The increase of $|\Delta S|$ as pressure increases reflects the preference of the system to form solvent-solvent and polymer-polymer bonds over polymer-solvent bonds. This induces the expulsion of water from within the particle and its subsequent deswelling.

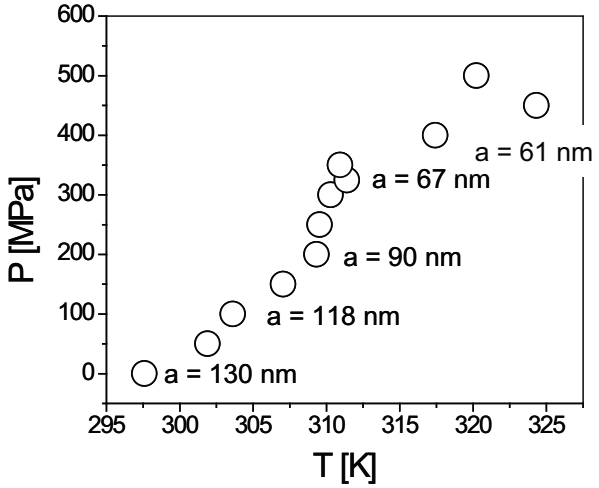

Figure 39: Comparison of the effect of pressure, P, and temperature, T, over the particle size. As can be observed, for intermediate pressures and temperatures, changes in particle size occurs more gradually when achieved with P than with T

[143]. We thus determine the entropy change using:

$$\Delta S = \frac{[\chi(P) - \chi_2\phi_2]k_bT - \Delta H}{T} \tag{79}$$

and obtain that $\Delta S < 0$ indicating that the system decreases its entropy when polymer-polymer and solvent-solvent bonds are replaced by polymer-solvent bonds. We find that the absolute value of the entropy change, $|\Delta S|$ increases; this implies that the entropy associated with a solvent-solvent contact is larger than the entropy associated to a polymer-solvent contact, ultimately causing the deswelling of the microgel particle, as we observe experimentally. Similar behavior has been previously measured for other systems which deswell with temperature [122, 123, 124] or ionic concentration [121]; the absolute value of the entropy change increases as the variable triggering the deswelling increases, consistent with our data and thus supporting our hypothesis. To finally characterize the role of hydrostatic pressure, we compare it with the role of temperature by identifying (T, P) pairs that correspond to the same particle size, as shown in Fig.39. We find that, at low pressures and temperatures, there is an approximately linear relationship between these variables indicating that both magnitudes have a similar effect on the microgel size. However, at intermediate

values of pressure and temperature, a slight increase in temperature, from ∼309 to ∼312 K, requires a much larger increase in pressure, from ∼200 to ∼400 MPa, in order to change the microgel size by equal amounts. Particle deswelling thus proceeds slower when using pressure than it does when using temperature, suggesting that pressure may be a better external variable when precise tuning of the particle size and thus of the suspension volume fraction is desired.

CHAPTER V

PHASE AND NON-EQUILIBRIUM BEHAVIOR OF MICROGEL SUSPENSIONS IN THE PRESENCE OF HYDROSTATIC PRESSURE AND USING SMALL ANGLE NEUTRON SCATTERING

5.1 Introduction

As we clearly saw in Chapter 2, the softness of microgel particles affects their phase behavior. While for hard spheres, the maximum packing fraction is limited by the crystal close packing in fcc and hcp lattice, $\phi = 0.74$, microgel suspensions can be further concentrated to fill the all available space and even beyond that since they are able to shrink, deform and/or interpenetrate. This gives rise to a rich phase and non-equilibrium behavior.

For instance, ionic microgels made of NIPAM-Acc display a progressive shrinkage of the crystal region as the microgel swells through ionization of the polymer network, implying the system eventually transitions from a liquid to a glass. This happens with monodisperse samples and thus cannot be attributed to polydispersity [55]. Theoretical expectations suggest a richer phase behavior for suspensions of very soft charged microgels with formation of noncubic crystal structures at high enough ζ [58, 59].

Motivated by these results we will analyze in this Chapter the phase and non-equilibrium behavior of NIPAM-Acc microgels. We will use Small Angle Neutron Scattering (SANS), given that the particle size of our microgels change around 100 nm, and both hydrostatic pressure and temperature to tune the microgel size. We will

start by reviewing the fundamentals of small angle neutron scattering experiments in order to obtain a relationship between the scattered intensity and the structure of the system. As it turns out, the scattered intensity depends on the particularities of the individual particle, through the form factor, and on the correlations between different particles through the structure factor. As a result, to extract structural information from the measured scattered intensity we will need to know the particle form factor.

With this in mind, we will first determine the form factor of the microgel particles at different temperatures and hydrostatic pressures using SANS in dilute solutions. Interestingly, as a result of the intrinsic inhomogeneity of the microgel particles, the form factor cannot be described using the classical hard sphere model. Accounting for the core-shell structure of the particle is essential in order to properly describe the experimental results. We will use such a model and show it provides successful results with reasonable values of the free parameters involved

We will, then, study the phase behavior of the system. Visually, we identify the ζ ranges corresponding to liquid, crystal and glassy phases. Remarkably, the ζ ranges corresponding to these states agree well with what is found in hard spheres suspensions.

For the crystalline samples, we measure the scattered intensity with SANS, use the experimentally measured form factors and fit the experimental results to several lattice models. We obtain reasonable agreement with the data. However, due to the experimental resolution we cannot determine the particular crystal structure. We study the nucleation and growth of the crystals as well as their behavior under the influence of hydrostatic pressure to deswell the particles.

For the glass samples, we found unexpected structure factors. Similar unusual structure factors were obtained by others [144], who proposed particle deswelling under the own osmotic pressure of the suspension as the cause for such unexpected

results. By considering this possibility, these authors corrected the particle form factors and obtained structure factors described with hard sphere models. We interpret our results differently, based on what we have learned in Chapter 3, and proposed that polydispersity could cause the observed behavior. This is suggested by previous experiments with very polydisperse microgels, which despite their polydispersity were able to still form beautiful crystals [57]

We thus attempt to describe our experimental results in terms of a model structure factor for polydisperse spheres obtaining a moderate agreement. That could be taken as a hint for the role of this effect. More theoretical work is clearly needed in order to further explore the effects of polydispersity. Our interpretation, however, suggests that the softness of the particles allows the system to change its polydispersity for it to to mimic the phase behavior of colloidal hard spheres.

5.2 Experimental system and Techniques

5.2.1 Experimental system

We use microgel particles based on NIPAM copolymerized with acrylic acid (Acc) in water. The particles were synthesized by an emulsion polymerization method in which NIPAM monomer, Acrylic Acid (2 % molar ratio), methylenebis(acrylamide) cross-linker (5 % molar ratio) and sodium dodecyl sulfate surfactant (0.05 % weight ratio) were mixed in deionized water at 70^oC under an inert atmosphere with constant nitrogen bubbling. Potassium persulfate (0.06 % weight ratio) is used to initiate the reaction, which was allowed to proceed for 4h at the same temperature. After cooling the products, the particles were extensively dyalized against ultrapure water and finally, freeze-dried and redispersed in D_2O, which we will use as a solvent for the SANS experiments.

5.2.2 Small Angle Neutron Scattering

Scattering of neutrons has been widely used as a method to determine static and dynamic properties of very different systems taking advantage of the fact that neutrons only interact with atomic nuclei as opposed to electromagnetic radiation, which interacts mainly with the electronic cloud of the atoms. As a result, neutrons are able to penetrate deeper inside the sample and are mostly singly scattered, except at extremely high concentrations. This results from the small space occupied by the nuclei compared to the space occupied by the electron cloud of the atoms.

In any small angle neutron scattering experiment, a beam of collimated and fairly monochromatic radiation of flux, $I_0(\lambda)$, is directed at a sample, illuminating a small volume, V, which depends on the area of the beam, A_{beam} and the width of the sample, d. Even though, most of the radiation is transmitted, some is absorbed and some is scattered. If we place a detector of area, $A_{detector}$, at an angle θ and distance L from the sample, scattered radiation within a solid angle $d\Omega_d = A_{detector}/L^2$ will be collected. The flux of collected light, $I_s(\lambda, \theta)$, can be expressed as [145, 146]:

$$I_s(\lambda, \theta) = I_0(\lambda)\ d\Omega_d\ \epsilon\ Tr\ V(\frac{d\sigma}{d\Omega})_V \tag{80}$$

where ϵ is the efficiency of the detector, Tr is the transmission coefficient of the sample and $(\frac{d\sigma}{d\Omega})_V$ is the microscopic differential cross-section, which contains all the information about the shape, size, interactions and structural features of the scatterers. Whereas $I_0(\lambda)$, $d\Omega_d$ and ϵ depend on the source and the particular arrangement of the experimental set-up, T_r, V and $(\frac{d\sigma}{d\Omega})_V$ are sample dependent. Of these three contributions, only $(\frac{d\sigma}{d\Omega})_V$ depends on $\mathbf{q}$, thus containing the desired structural information.

Consider an incident neutron beam consisting of a collection of neutrons, each

taken as a wave packet of the form:

$$\Psi_i = A(x, y, z, t)e^{-i(\vec{k_i}\vec{r}-\omega t)} \tag{81}$$

where $\mathbf{k_i}$ is the wave vector with magnitude $|\mathbf{k_i}| = \frac{\mathbf{2\pi}}{\lambda_\mathbf{i}}$ and λ_i the wavelength, and $A(x, y, z, t)$ the amplitude of the wave which obeys the normalization condition $\int\int\int A(x, y, z, t)A^*(x, y, z, t)d^3r = 1$, which implies that the possibility of finding the packet in all the space is 1. Let us suppose that this wave travels in the z direction and encounters an atomic nucleus located at (x_0, y_0, z_0), producing an emerging wave packet that contains a scattered wavelet and an incident wavelet that remains unscattered. The form of the scattered wave follow from the considerations [147]:

- If the scattering is elastic, the magnitude of the wave vector remains unaltered, $|\vec{k_i}| = |\vec{k_s}| = k$.

- At distances larger than the characteristic scattering volume, the scattered wavelet is a spherical wave that propagates radially outward. The phase of this wave is $e^{-i(k\,z-\omega t)}$.

- The spreading in the wave packet is negligible and thus $A(x, y, z, t) = A(x, y, z - vt, 0)$.

- The amplitude of the scattered wave is proportional to the amplitude of the incident wave. Therefore, the amplitude of the scattered wave will be proportional to $A(x_0, y_0, z_0 + r - vt, 0)$, where r is the distance along z away from z_0, $v = \frac{\hbar k}{m}$, is the group velocity of the wave packet and $\hbar = h/(2\pi)$, with h the Planck's constant [148].

- The amplitude of the wave will have an angular dependence, due to interference, and will decrease with distance due to its spherical nature. Thus, the asymptotical approximation for the scattered wave is:

$$\Psi_s = \frac{f(\theta, \phi)}{r}A(x, y, z, t)e^{-i(\vec{k_s}\cdot\vec{r}-\omega t)} \tag{82}$$

with θ and ϕ the azimuthal and radial angles in spherical coordinates [149].

We define the probability of finding the scattered neutron in a solid angle $d\Omega$ as:

$$P(x_0, y_0, \Omega)d\Omega = d\Omega \int_0^\infty \Psi_s \Psi_s^* r^2 dr \tag{83}$$

where this probability should be constant in the cone subtending the solid angle $d\Omega$. Combining Eq.82 and 83 we obtain:

$$P(x_0, y_0, \Omega)d\Omega = d\Omega |f(\theta, \phi)|^2 \int_{-\infty}^\infty dz |A(x_0, y_0, z, 0)|^2 \tag{84}$$

with $z = z_0 + r - vt$. By defining the differential cross-section, $\frac{d\sigma}{d\Omega}$, as the probability of finding the scattered particle in a solid angle $d\Omega$ when one neutron is incident and collides with one scatterer, we can write:

$$P(\Omega)d\Omega = \frac{d\sigma}{d\Omega} d\Omega \tag{85}$$

By further considering that wave packet mainly lies along z, the normalization condition for the amplitude A can be written as the the integral in Eq. 97 and thus [145, 148]:

$$\frac{d\sigma}{d\Omega} = |f(\theta, \phi)|^2 \tag{86}$$

The problem we then need to solve is that of an incident wave packet interacting with an atomic nucleus through a potential which we will model as a delta function $V(\mathbf{r}) = V_a \delta(\mathbf{r} - \mathbf{r_a})$, with $\mathbf{r_a}$ the position of the nucleus. The time-dependent Schroedinger equation is:

$$i\hbar \frac{\partial}{\partial t} \Psi = [-\frac{\hbar^2}{2m} \nabla^2 + V(\vec{r})]\Psi \tag{87}$$

where $\Psi = \Psi_i + \Psi_s$ and m the mass of the neutron.

This equation can be written as:

$$i\hbar \frac{\partial}{\partial t} \Psi_s = (-\frac{\hbar^2}{2m} \nabla^2)\Psi_s + V(\vec{r})(\Psi_i + \Psi_s) \tag{88}$$

after realizing that the incident wave corresponds to a free particle before the collision; as a result Ψ_i follows Eq.87 with V=0.

Invoking the Born approximation [150], we assume that $|\Psi_i| \gg |\Psi_s|$ and thus:

$$i\hbar\frac{\partial}{\partial t}\Psi_s = (-\frac{\hbar^2}{2m}\nabla^2)\Psi_s + V(\vec{r})(\Psi_i) \tag{89}$$

This equation can be solved, resulting[148]:

$$\Psi_s = -\frac{mA(x_0,y_0,r,t)e^{i(\vec{k}_s\cdot\vec{r}-\omega t)}}{2\pi\hbar^2 r}\int\int\int d^3\vec{r}\,' V_a\delta(\vec{r}\,' - \vec{r}_a)e^{-i(\vec{k_s}-\vec{k_i})\cdot\vec{r}\,'} \tag{90}$$

We obtain and expression for $f(\theta,\phi)$ by comparing this equation with Eq.82:

$$f(\theta,\phi) = \frac{-m}{2\pi\hbar^2}\int\int\int d^3\vec{r}\,' V_a\delta(\vec{r}\,' - \vec{r}_a)e^{-i(\vec{k_s}-\vec{k_i})}\cdot\vec{r}\,' \tag{91}$$

Solving the integral, we obtain::

$$f(\theta,\phi) = \frac{-m}{2\pi\hbar^2}V_a = b \tag{92}$$

where we have assumed $V_a = -\frac{2\pi\hbar^2}{m}b$. Therefore the differential cross-section (Eq.86) can be written as:

$$\frac{d\sigma}{d\Omega} = b^2 \tag{93}$$

b defines the strength of the interaction between a neutron and a nucleus. Table 5.2.2 shows the values of b for different atomic nuclei. It is worth noting that some of the values of b are negative, indicating that as a result of the scattering, the resultant wave is out-of-phase with respect the the incident wave by π radians.

Let us now consider scattering from a collection of N nuclei, each characterized by its scattering amplitude, b_j with j=1,...,N. The wave scattered by nucleus j can be written as:

$$\Psi_{s,j}(\vec{r}) \sim \frac{b_j}{r}e^{i\vec{q}\vec{r}_j} \tag{94}$$

following Eq.90 and 92, with r_j is the distance between the scatterer and the detection point and $\mathbf{q} = \mathbf{k_s} - \mathbf{k_i}$ is the scattering wave vector. The proportionality constant is

Table 2: Scattering amplitudes for different atomic nuclei

Atomic Nucleus	b [fm]
H	-3.741
D	6.671
C	6.646
N	9.362
O	5.803
Na	3.580
Cl	9.577
S	2.847

the function $A(x, y, z)$, which only depends on the properties of the incident neutrons. For simplicity we will not carry along this prefactor. The total scattered wave at the detector is the superposition of all scattered waves:

$$\Psi(\vec{r}) = \sum_{j=1}^{N} \Psi_{s,j} = \sum_{j=1}^{N} \frac{b_j}{r_j} e^{i\vec{q}\cdot\vec{r}_j} \tag{95}$$

where we have taken into consideration that r_j is large compared with the distance between nuclei and, thus, $r_j = r$ for all the nuclei. Using that $\Psi_i(\mathbf{r})$, we can calculate the probability of having a scattered neutron at point r as:

$$< \Psi\Psi^* >= \frac{1}{r^2} < \sum_{j=1}^{N} b_j e^{i\vec{q}\cdot\vec{r}_j} \sum_{k=1}^{N} b_k e^{-i\vec{q}\cdot\vec{r}_k} > \tag{96}$$

and, therefore, the probability that a neutron is scattered within a solid angle $d\Omega$ is:

$$\frac{d\sigma}{d\Omega} =< \sum_{j=1}^{N} b_j e^{i\vec{q}\cdot\vec{r}_j} \sum_{k=1}^{N} b_k e^{-i\vec{q}\cdot\vec{r}_k} > \tag{97}$$

This expression can be rewritten as:

$$\frac{d\sigma}{d\Omega} =< \sum_{k=1}^{N} b_k^2 + \sum_{j} \sum_{k\neq j}^{N} b_k b_j e^{-i\vec{q}\cdot(\vec{r}_k - \vec{r}_j)} >= \tag{98}$$

$$N < b^2 > + < b >^2 < \sum_{j} \sum_{k\neq j}^{N} e^{-i\vec{q}\cdot(\vec{r}_k - \vec{r}_j)} >$$

where we have assumed that b_j and b_k are independent and, thus, uncorrelated. Using the statistical deviation in b, $\Delta b^2 =< (b - < b >)^2 >=< b^2 > - < b >^2$, Eq.98 can

be rewritten as:

$$\frac{d\sigma}{d\Omega} = N\Delta b^2 + < b >^2 \sum_{j,k=1}^{N} e^{-i\vec{q}\cdot(\vec{r}_k - \vec{r}_j)} \tag{99}$$

where the double sum on the right hand side of the the equation now runs from 1 to N for both indexes. Notice that the first term of the equation depends on the fluctuations in the value of b amongst nuclei irrespective of their particular position. This is what is called incoherent scattering; and it appears when there is a mixture of nuclei with different values of b. Incoherent scattering does not result from constructive interference and, thus, it does not contain any structural information about the distribution of nuclei. There are other possible sources of incoherent scattering. For example, due to coupling between the spin of the nuclei and the neutron spin. This is particularly important for the case for hydrogen explaining why most neutron scattering experiments are performed in deuterated rather than hydrogenated solvents [145, 151].

The $e^{-i\mathbf{q}\cdot(\mathbf{r_k}-\mathbf{r_j})}$ term in Eq.99 depends on the particular arrangement of the atoms and can give rise to constructive or destructive interference of the scattered waves. For this reason, it is usually referred to as the coherent scattering contribution; it is the sought for contribution to the differential cross section, as it allows the access of the structural information of the sample.

We will, thus, focus on:

$$(\frac{d\sigma}{d\Omega})_{coh} = < b >^2 < \sum_{j,k=1}^{N} e^{-i\vec{q}\cdot(\vec{r}_k - \vec{r}_j)} > \tag{100}$$

which holds for a system with one component. We can extend this expression to the continuum limit by defining a density function $n(\mathbf{r}) = \sum_{j=1}^{N} \delta(\mathbf{r} - \mathbf{r_j})$. Then:

$$\begin{aligned}(\frac{d\sigma}{d\Omega})_{coh} = < b >^2 < \int_V n(\vec{r}) e^{-i\vec{q}\cdot\vec{r}} \int_{V'} n(\vec{r}\,') e^{i\vec{q}\cdot\vec{r}\,'} > = \\ < b >^2 \int_V \int_{V'} e^{-i\vec{q}\cdot(\vec{r}-\vec{r}')} < n(\vec{r}) n(\vec{r}\,') >\end{aligned} \tag{101}$$

which can also be expressed as a function of the density fluctuations $\Delta n(\mathbf{r})$ [152]:

$$(\frac{d\sigma}{d\Omega})_{coh} = b^2 \int_V \int_{V'} e^{-i\vec{q}\cdot(\vec{r}-\vec{r}')} < \Delta n(\vec{r})\Delta n(\vec{r}') > \tag{102}$$

where we have substituted the symbol $< b >$ by b for simplicity. Note that both Eq.101 and Eq.102 reflect that the scattering arises from correlations between regions in the sample with different density. As a result, for an homogeneous sample $< \Delta n(\vec{r})\Delta n(\vec{r}') > \sim 0$ and $(\frac{d\sigma}{d\Omega})_{coh} \sim 0$.

Let us now consider the situation for a two-component system comprising N_1 nuclei of a specie 1 with scattering length b_1, and N_2 nuclei of specie 2 with scattering length b_2. Expression (100) can be generalized to:

$$\begin{aligned}(\frac{d\sigma}{d\Omega})_{coh} = b_1^2 < \sum_{i_1,j_1=1}^{N_1} e^{-i\vec{q}\cdot(\vec{r}_{i_1}-\vec{r}_{j_1})} > + b_2^2 < \sum_{i_2,j_2=1}^{N_2} e^{-i\vec{q}\cdot(\vec{r}_{i_2}-\vec{r}_{j_2})} > \\ + 2b_1b_2 < \sum_{i_1}^{N_1}\sum_{j_2}^{N_2} e^{-i\vec{q}(\vec{r}_{i_1}-\vec{r}_{j_2})} >\end{aligned} \tag{103}$$

which in the continuum limit becomes:

$$\begin{aligned}(\frac{d\sigma}{d\Omega})_{coh} =& b_1^2 \int_V d\vec{r} \int_{V'} d\vec{r}\,' < \Delta n_1(\vec{r})\Delta n_1(\vec{r}') > e^{-i\vec{q}(\vec{r}-\vec{r}')} + \\ & b_2^2 \int_V d\vec{r} \int_{V'} d\vec{r}\,' < \Delta n_2(\vec{r})\Delta n_2(\vec{r}') > e^{-i\vec{q}\cdot(\vec{r}-\vec{r}')} + \\ & 2b_1b_2 \int_V d\vec{r} \int_{V'} d\vec{r}' < \Delta n_1(\vec{r})\Delta n_2(\vec{r}') > e^{-i\vec{q}\cdot(\vec{r}-\vec{r}')}\end{aligned} \tag{104}$$

where we have used Eqs.101 and 102. This expression can be further simplified as:

$$(\frac{d\sigma}{d\Omega})_{coh} = b_1^2 F_{11}(\vec{q}) + b_2^2 F_{22}(\vec{q}) + 2b_1b_2F_{12}(\vec{q}) \tag{105}$$

where we have defined the partial structure factor:

$$F_{ab}(\vec{q}) = \int_V d\vec{r} \int_{V'} d\vec{r}\,' < \Delta n_a(\vec{r})\Delta n_b(\vec{r}') > e^{-i\vec{q}\cdot(\vec{r}-\vec{r}\,')} \tag{106}$$

Note that the three partial structure factors are not independent. Since the system is incompressible the total density is constant and:

$$\Delta n_1(\vec{r}) + \Delta n_2(\vec{r}) = 0 \tag{107}$$

expressing that if the density of specie 1 increases it is at the expense of decreasing the density of specie 2. Multiplying this expression by $\Delta n_1(\vec{r})e^{-i\mathbf{q}\cdot(\mathbf{r}-\mathbf{r}')}$ and integrating over the scattering volume we obtain:

$$F_{11}(\vec{q}) + F_{12}(\vec{q}) = 0 \tag{108}$$

alternatively, by multiplying by $\Delta n_2(\vec{r})e^{-i\mathbf{q}\cdot(\tilde{\mathbf{r}}-\tilde{\mathbf{r}}')}$ we obtain:

$$F_{22}(\vec{q}) + F_{12}(\vec{q}) = 0 \tag{109}$$

Introducing these expressions in Eq.105, we get that for a two component system:

$$(\frac{d\sigma}{d\Omega})_{coh} = (b_1 - b_2)^2 F_{11}(\vec{q}) = (b_1 - b_2)^2 F_{22}(\vec{q}) = -(b_1 - b_2)^2 F_{12}(\vec{q}) \tag{110}$$

which can be further generalized with a system of p+1 components [145]:

$$(\frac{d\sigma}{d\Omega})_{coh} = \sum_{i=1}^{p}(b_i - b_0)^2 F_{ii}(\vec{q}) + 2\sum_{i<j}(b_i - b_0)(b_j - b_0)F_{ij}(\vec{q}) \tag{111}$$

in which the specie $'0'$ is the one filling the vacancies to fulfill the incompressible condition; this specie is usually regarded as the solvent.

Let us now consider a system containing N macromolecules, each comprised of z segments, which we consider as point scatterers with scattering length, b. The partial structure factor for the system is:

$$F(\vec{q}) = \sum_{p=1}^{N}\sum_{q=1}^{N}\sum_{j=1}^{z}\sum_{k=1}^{z} < e^{-i\vec{q}(\vec{r}_{pj} - \vec{r}_{qk})} > \tag{112}$$

We can extract the terms in which p=q, which correspond to interference within segments belonging to the same macromolecule. There are N terms of this type and they are all identical. The other term will represent interference between pairs of segments in different macromolecules. There are $N(N-1)$ identical pairs of this type. Therefore:

$$F(\vec{q}) = N\sum_{i_1=1}^{z}\sum_{j_1=1}^{z} < e^{-i\vec{q}\cdot(\vec{r}_{i_1} - \vec{r}_{j_1})} > + N(N-1)\sum_{i_1=1}^{z}\sum_{j_2=1}^{z} < e^{-i\vec{q}\cdot(\vec{r}_{i_1} - \vec{r}_{j_2})} > \tag{113}$$

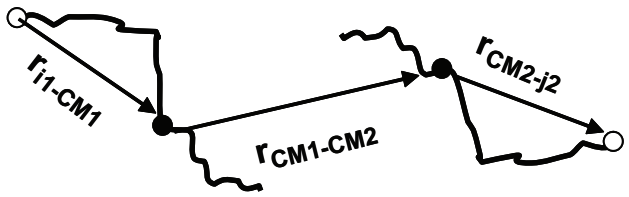

Figure 40: Schematic representation of the decomposition in Eq.117

By means of this rearrangement, we have separated the partial structure factor into one term that only depends on the particular properties of the macromolecules and another term that only depends on the distribution of the macromolecules. We note the first term as $P(\vec{q})$ and thus:

$$P(\vec{q}) = \frac{1}{z^2} \sum_{i_1=1}^{z} \sum_{j_1=1}^{z} < e^{-i\vec{q}\cdot(\vec{r}_{i_1} - \vec{r}_{j_1})} > \tag{114}$$

This is the form factor of the macromolecule and it only contains information about interference of scattered waves from segments in the same macromolecule. It is independent of the solution and contains information about the size and shape of the macromolecule. By contrast, the other term in Eq. 113 depends on the interference of scattered waves from segments in different macromolecules. This term, which we note $Q(\mathbf{q})$, contains the structural information for the solution:

$$Q(\vec{q}) = \frac{1}{z^2} \sum_{i_1=1}^{z} \sum_{j_2=1}^{z} < e^{-i\vec{q}\cdot(\vec{r}_{i_1} - \vec{r}_{j_2})} > \tag{115}$$

And, thus:

$$F(\vec{q}) = Nz^2 P(\vec{q}) + N(N-1)z^2 Q(\vec{q}) \tag{116}$$

We can still simplify the expression for $Q(\mathbf{q})$. From Fig.40, it is clear that:

$$\vec{r}_{i_1} - \vec{r}_{j_2} = \vec{r}_{i_1} - \vec{r}_{CM_1} + \vec{r}_{CM_1} - \vec{r}_{CM_2} + \vec{r}_{CM_2} - \vec{r}_{j_2} \tag{117}$$

with $\vec{r}_{CM_i}$ the position of the center of mass of the i-th macromolecule. Using this, Eq.115 becomes:

$$Q(\vec{q}) =< e^{-i\vec{q}\cdot(\vec{r}_{CM_1} - \vec{r}_{CM_2})} > \frac{1}{z^2} \sum_{i_1=1}^{z} \sum_{j_2=1}^{z} < e^{-i\vec{q}\cdot[\vec{r}_{CM_2} - \vec{r}_{j_2} - (\vec{r}_{CM_1} - \vec{r}_{i_1})]} >= \tag{118}$$

$$< e^{-i\vec{q}\cdot(\vec{r}_{CM_1} - \vec{r}_{CM_2})} > P(\vec{q})$$

Table 3: Values of b_0/v_s for selected solvents and polymers

Material	b_0/v_s $[\mu m^{-2}]$
Water	-56.1
Deuterated Water	634.2
Toluene	94.2
Polystyrene	142.3
Polyethylene Oxide (PEO)	64.1
Poly MethylMethacrylate (PMMA)	110.3
N-Isopropylacrilamide (NIPAM)	59.1

and Eq.116 can be finally written as:

$$F(\vec{q}) = Nz^2 P(\vec{q})[1 + (N-1) < e^{-i\vec{q}\cdot(\vec{r}_{CM_1} - \vec{r}_{CM_2})>}] = Nz^2 P(\vec{q}) S(\vec{q}) \tag{119}$$

where $S(\mathbf{q}) = [1 + (N-1) < e^{-i\mathbf{q}\cdot(\mathbf{r_{CM_1}} - \mathbf{r_{CM_2}})} >]$ is the structure factor of the system. For a binary mixture of macromolecules and a solvent, we then have (Eq.111):

$$(\frac{d\sigma}{d\Omega})_{coh} = (b_1 - b_0)^2 N z^2 P(\vec{q}) S(\vec{q}) \tag{120}$$

with species 1 the macromolecules and specie $'0'$ the solvent.

Given that each segment is treated as a singular scatterer by assuming its volume is identical to the volume of a solvent molecule, v_s, the volume of a single macromolecule can be written as $V_{mac} = zv_s$, since each macromolecule is made of of z segments. Since the scattering length of a macromolecule is $b_{mac} = zb_1$, then:

$$\frac{b_1}{v_s} = \frac{b_{mac}}{V_{mac}} \tag{121}$$

and thus:

$$(\frac{d\sigma}{d\Omega})_{coh} = v_s^2 b_v^2 N z^2 P(\vec{q}) S(\vec{q}) \tag{122}$$

where $b_v = \frac{b_{mac}}{V_{mac}} - \frac{b_0}{v_s}$ is the difference in the scattering length density between the macromolecule and the solvent. Table 5.2.2 shows the scattering length densities for some usual polymeric materials and solvents. The result for the coherent scattering

cross section in Eq.122 per unit volume. Thus,

$$(\frac{d\sigma}{d\Omega})_{coh}/V = (\frac{d\sigma}{d\Omega})_{coh,V} = b_v^2 \frac{N}{V} V_{mac}^2 P(\vec{q}) S(\vec{q}) \tag{123}$$

where we emphasize again that V_{mac} is the sum of volume of all segments in the macromolecule. Eq.123 shows that the differential cross-section per unit volume depends on the number density of macromolecules, on their volume, V_{mac}, on their shape and size through the particle form factor P($\mathbf{q}$) and on the correlation between them, through the structure factor S($\mathbf{q}$).

5.2.3 Experimental details

Measurements of SANS were performed using the SANS-I apparatus situated at SINQ in Paul Scherrer Institute in Switzerland. A schematic of the technique is shown in Fig.41. A beam of incoming thermal neutrons generated in a spallation source (E $\sim$ 25meV) [153] and cooled down through a large heavy water moderator, is guided through a mechanical monochromator filtering neutrons of certain wavelength with a resolution $\Delta\lambda/\lambda \sim 0.1$. The beam is collimated along a waveguide with lengths ranging from 1 to 18m and focused onto the sample cells, made of quartz and having a path length of 1 or 2 mm, using neutron lenses [154, 155] to reduce the uncertainty in the scattering angle. Therefore, $\Delta q/q \sim \Delta\lambda/\lambda$. The scattered neutrons are collected in a two-dimensional detector with 128 x 128 elements of 7.5 x 7.5 mm^2, which can be placed at a distance ranging from 1.4 to 20m away from the sample. In this way, we have access to three decades in scattering wavevector, from $5{\cdot}10^{-3}$ nm^{-1} to 5.4 nm^{-1}.

he scattered intensity needs to be corrected after measured:

- We correct for the dark counts of the detector by blocking the beam with a Cadmium sheet. This measurement also detects stray neutrons that do not go through the sample, such as cosmic radiation.

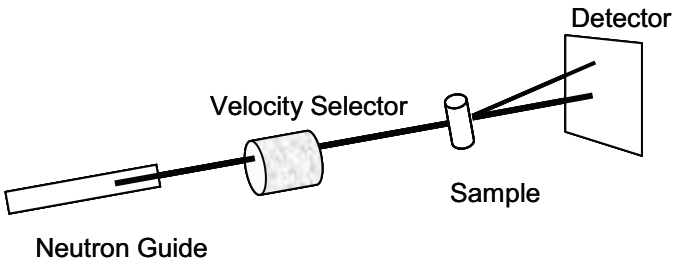

Figure 41: Schematic representation of a typical small angle neutron scattering layout.

- We calibrate the efficiency of each pixel of the detector by performing a measurement with water, which is a Rayleigh scatterer.
- We perform measurements of the solvent alone to account for its scattering.
- We also measure the scattering from the cells used in our experiments. We correct all other samples with this contribution.
- Finally, we measured the transmission through the samples and through the empty cell. We use this last measurement to determine the center of the beam and radial average the data with respect to it.

5.3 Experimental Results

5.3.1 System Characterization

As expected from previous results [137, 138, 139] and the behavior shown in Chapter 4 for a similar system, the particle size decreases with increasing temperature, as shown in Fig. 42a. The miscibility of NIPAM in the solvent decreases as temperature increases and, as a result, it is increasingly favorable for the system to promote solvent-solvent and polymer-polymer contacts over solvent-polymer contacts and the particles deswell to a deswollen size of 60nm. It is important to note that for our NIPAM particles the range of deswelling is considerably broadened in comparison with a pure NIPAM system. This is due to the presence of acrylic acid on the polymer network which affects the swelling behavior due to dissociation; this changes

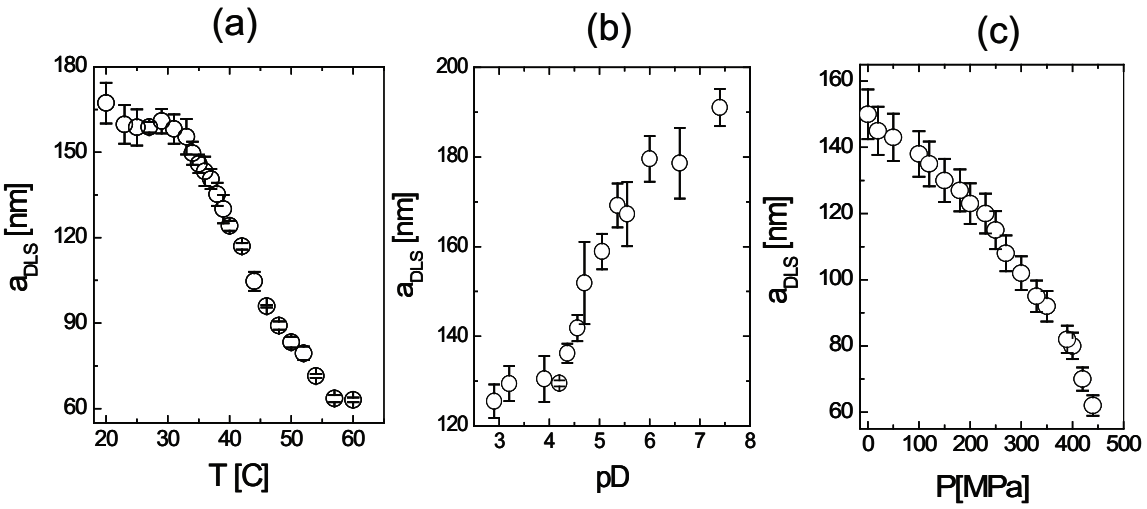

Figure 42: a) Radius a_{DLS} of pNIPAM-Acc microgels in D_2O as a function of a) temperature, T at pD=5.5, b) pD and c) hydrostatic pressure, P, measured by DLS. The particle deswells with both increasing T and P and with decreasing pD.

the network and affects the ionic distributions inside and outside the particles. This, in turn, affects the osmotic equilibrium of the particles causing additional swelling.

The particle size dependence with pD is shown in Fig.42b. Since the pK_a of polyacrylic acid is 5.6 [156], the system remains essentially uncharged at low values of pD resulting in a constant particle size. However, as the pD is increased, the ionization of the acrylic acid becomes increasingly important and the particle swells due to the ionic osmotic pressure exerted by the counterions. This is observed for pD > 4, which is in agreement with previous results [157, 158]. Since the size-temperature measurements were performed at pD=5.5, where the network is partially ionized, the deswelling transition becomes broader in temperature, consistent with previous results with charged gels [159, 160] and microgels [157, 158].

Hydrostatic pressure also induces particle deswelling [161], as shown in Fig.42c. A similarly broadened deswelling transition is observed in this case with a deswollen radius for large P of 60nm, consistent with the size measured at high temperature.

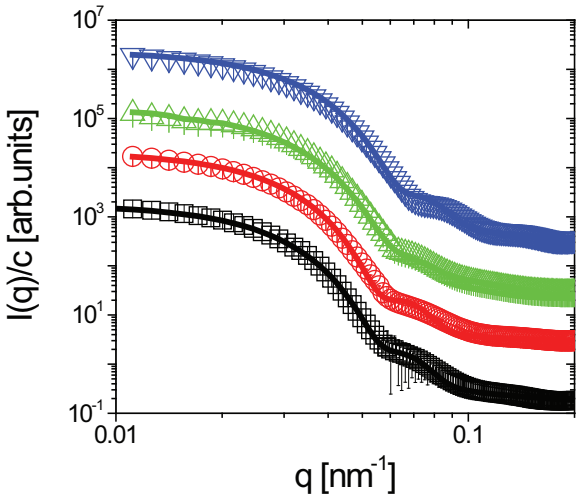

Figure 43: Experimental profiles for four different temperatures and their corresponding fits according to Eq.129: (□) $T = 25°C$ and $R_{av} = 83nm$, $\sigma = 21nm$, $\sigma_{pol} = 0.13$, $I_{chain}(0) = 2.0\ 10^{-4}$, $\xi = 10.4nm$; (○) $T = 27°C$ and $R_{av} = 82nm$, $\sigma = 21nm$, $\sigma_{pol} = 0.11$, $I_{chain}(0) = 9.0\ 10^{-5}$, $\xi = 10.2nm$; (△) $T = 30°C$ and $R_{av} = 77nm$, $\sigma = 23nm$, $\sigma_{pol} = 0.13$, $I_{chain}(0) = 5.9\ 10^{-4}$, $\xi = 9.8nm$; (▽) $T = 35°C$ and $R_{av} = 73nm$, $\sigma = 18nm$, $\sigma_{pol} = 0.12$, $I_{chain}(0) = 1.3\ 10^{-4}$, $\xi = 9.2nm$; The data is vertically shifted by a factor of 10 with increasing temperature.

5.3.2 Determination of the particle form factor

Since, in order to characterize the structural features of our samples, we must know the form factor, P(**q**), we determine the scattered intensity of a microgel dilute suspension, since in this situation $S(\mathbf{q}) \approx \mathbf{1}$. We find that the q-dependence of the scattered intensity is characterized by an initial decay at low q and by a shoulder at intermediate q, as shown in Fig.43 for different temperatures. At higher values of q, the intensity plateaus as a result of incoherent scattering arising from the spin coupling between the neutrons and the hydrogen atoms in the sample. We find similar results at different hydrostatic pressures, as shown in Fig.44. With increasing P, the form factor shifts to higher q, consistent with particle deswelling. The presence of a shoulder in the intermediate q-region as observed with temperature measurement, is however, hindered in this case by experimental noise due to insufficient counting time. The experimental profiles show the intrinsic structural richness of these particles. At high

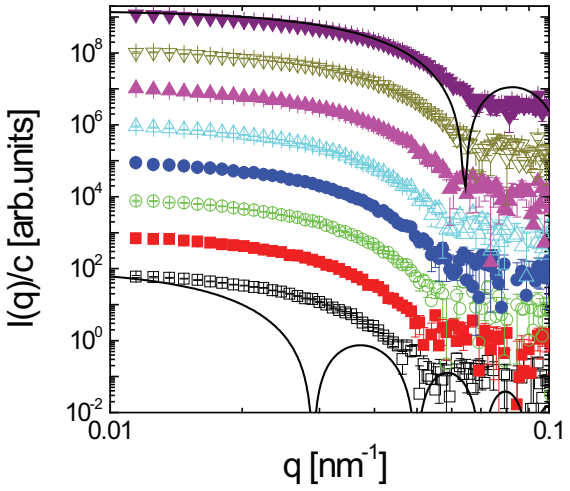

Figure 44: Experimental profiles for different hydrostatic pressure: (□) $P = 0$, (■) $P = 100$MPa, (○) $P = 150$MPa, (●) $P = 175$MPa, (△) $P = 200$MPa, (▲) $P = 250$MPa, (▽) $P = 300$MPa, (▼) $P = 350$ MPa. The data is vertically shifted by a factor of 10 with increasing hydrostatic pressure. The lines represent the expected form factor for hard spheres of radius $R = 145$ nm (lower line) and $R = 70$ nm (upper line)

pressures, the particles are fully deswollen and, thus, the particles are expected to behave essentially as hard spheres. Consistent with this, we fit our experimental curves at high P with the hard sphere form factor [72, 73, 145]:

$$P_1(q,a) = [\frac{3}{(qa)^3}(\sin qa - qa\cos qa)]^2 \tag{124}$$

resulting from Eq.114 considering that the particle is a homogeneous sphere of radius a. The model correctly captures the low-q region but exhibits a sharp minimum at larger q that we do not see experimentally. This disagreement results from polydispersity of the sample, to confirm this we consider a suspension with a distribution of particle sizes given by a Gaussian function:

$$D(a,\sigma_{pol}) = \frac{1}{\sqrt{2\pi}\sigma_{pol}a_{av}} e^{-[(a-a_{av})^2/(2\sigma_{pol}^2 a_{av}^2)]} \tag{125}$$

with a_{av} the average particle radius and σ_{pol} the particle polydispersity.

With this consideration, we fit the experimental data using:

$$P(q) = \sum_a D(a,\sigma_{pol})P_1(q,a) \tag{126}$$

leaving a_{av} and σ_{pol} as free parameters. The data is well described with $a_{av} = 70$nm and $\sigma_{pol} = 0.12$. Note that the value obtained for a_{av} agrees very well with the value measured by Dynamic Light Scattering. The fit also provides a value for the sample polydispersity of 12%, which is reasonable given the method employed in the particle synthesis [165].

At lower hydrostatic pressures, the hard sphere analogy no longer holds as shown in Fig.44 for P=0. This reflects the intrinsic inhomogeneity of the particle in its swollen state, when the network is filled with water. One source for this inhomogeneous distribution of solid may come from the uneven distribution of cross-link molecules in the synthesis process [105, 93, 114]; it decreases from the particle center towards its periphery. Therefore, a more sophisticated model to describe the experimental results is needed.

We consider a previously published model by Stieger et al [144, 162] consisting in modeling the microgel as a hard sphere core and a fuzzy polymer shell. In reciprocal space, the total form factor is the product of both contributions [162]:

$$P_1(q) = [\frac{3(\sin qa - qa\cos qa)}{(qa)^3} e^{-[(\sigma q)^2/2]}]^2 \tag{127}$$

where a is now the radius of the core and σ the width of the fuzzy region. A similar version of this model was proposed by Pedersen to account for the scattering of block copolymer micelles [163].

In addition, the particle is further considered inhomogeneous at smaller length-scales and an additional contribution to the form factor associated to internal chain correlations is incorporated [151]:

$$I_{chain}(q) = \frac{I_{chain}(0)}{1 + (\xi q)^2} \tag{128}$$

where $I_{chain}(0)$ is the intensity at zero q associated with this contribution and ξ is the mesh size of the network. This expression has been used to describe the structure of neutral gels [151] as well as the scattering of certain semidilute polyelectrolyte

Table 4: Values of the free parameters obtained from the fits shown in Fig. 45. a_{av} is the radius of the core, σ is the width of the fuzzy region of the particle, $a_{SANS} = a_{av} + 2\sigma$, a_{DLS} is the particle radius as determined by dynamic light scattering, σ_{pol} is the core polydispersity, $I_{chain}(0)$ is amplitude of the polymer chain correlations at zero q and ξ is the correlation length or mesh size of the network.

a_{av}	σ	a_{SANS}	a_{DLS}	σ_{pol}	$I_{chain}(0)$	ξ	χ^2
83nm	21nm	125nm	142nm	0.13	$2.2\ 10^{-3}$	52nm	10^{-3}
83nm	21nm	125nm	142nm	0.13	$2.0\ 10^{-4}$	10nm	10^{-3}

solutions [164]; thus, it can be considered as a reasonable approximation for the internal structure of our NIPAM/Acc microgels.

Finally, we incorporate polydispersity in the model. As a result:

$$P(q) = \sum_a D(a, \sigma_{pol}) P_1(q, a) + I_{chain}(q) + I_0 \tag{129}$$

where I_0 is a constant that accounts for the presence of incoherent scattering in the sample.

Using this model, we fit the experimental curves minimizing the statistical χ^2-distribution defined as $\chi^2 = [P(q)_{exp} - P_{th}(q)]^2$ [141], leaving as free parameters: a_{av}, σ_{pol}, σ, ξ and $I_{chain}(0)$. The model successfully captures the different features of the experimental profiles, as shown Fig.45 for T=25C and P=0. For this curve, we obtain $a_{av} = 83$nm and $\sigma = 21$ nm which gives a particle radius $a_{SANS} = a_{av} + 2\sigma = 124.4$nm that is similar but slightly smaller than the particle size determined by DLS. The origin of this discrepancy could rely on the presence of a very small, but non negligible, number of peripheral chains, which would only contribute to the hydrodynamic radius, thus rendering a_{DLS} slightly larger than a_{SANS} [162]. For the particle polydispersity we obtain $\sigma_{pol} = 0.13$ consistent with the result found before.

However, the value for the mesh size, $\xi = 52$nm, is unreasonably large given the particle size. This number can be estimated as the average distance between crosslink points:

$$\hat{\xi} = (N_p V_{1p} / N_{xlink})^{1/3} \tag{130}$$

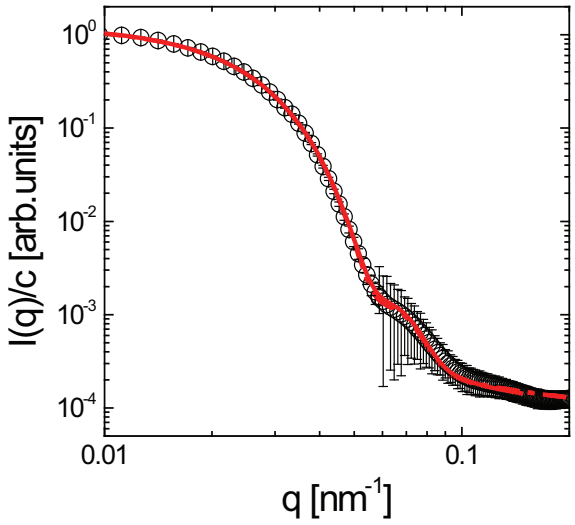

Figure 45: Intensity profile for $T = 25°\mathrm{C}$ and $P = 0$. The two fits to the data are essentially inappreciable and result in identical χ^2 values for the parameters shown in Table 5.3.2

with N_p the number of particles, V_{1p} the volume of one microgel and N_{xlink} the number of crosslink molecules. These quantities can be estimated from the synthesis resulting in, $\hat{\xi} \sim 5\mathrm{nm}$, which is an order of magnitude smaller than the value obtained in the fit. This disagreement can be traced back to the fitting procedure.

In Fig.46, we plot the value of the statistical χ^2 parameter for different values of $I_{chain}(0)$ and ξ for constant values of the other free parameters. As it can be seen, the selection of $I_{chain}(0)$ and ξ becomes degenerate since the parameter space contains many local minima of identical depth, which are shown as black points in Fig.46. Even if the value of χ^2 is similar for all of them, they correspond to very different values of $I_{chain}(0)$ and ξ. Sensible values can be obtained, however, if a careful spanning of the parameter space is achieved. To emphasize this, we show in Fig.45 two statistically equal fits with identical values of a_{av}, σ and σ_{pol} but with $\xi = 10.4\mathrm{nm}$ and $\xi = 52\mathrm{nm}$. Both fits are indistinguishable, but the lower value of the mesh size is in reasonable agreement with the expectations from the particle synthesis. Therefore, the selection of the best fit relies on both the value of χ^2 and on the known value of ξ. With this in

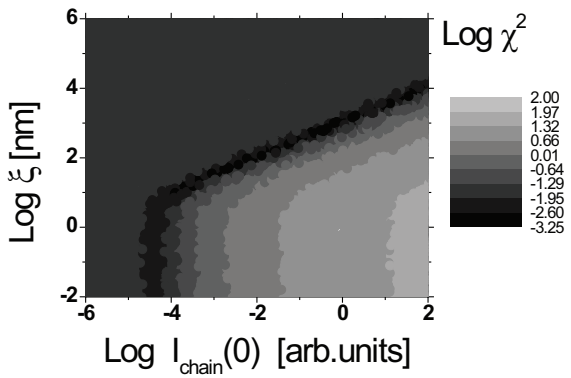

Figure 46: χ^2 as a function of $I_{chain}(0)$ and ξ, for the sample at $T = 25°C$ and $P = 0$.

mind, we can fit the experimental data at other temperatures, as shown by the solid lines in Fig.43.

To inquire about the similar role of temperature and hydrostatic pressure, we plot the experimental form factors at different temperatures and constant hydrostatic pressure together with those obtained at different hydrostatic pressure and constant temperature. This is shown in Fig.47. There is an excellent agreement between pairs of temperature and pressure, emphasizing the similar role played by both magnitudes in the physical behavior of microgel particles. This analogy can be used to describe the intermediate q-region on the hydrostatic pressure curves (Fig.44) where the lack of statistics did not allow a clear definition of the curves. Using this mapping, we determine the dependence with P, as shown in Fig.48. We find that a_{SANS} decreases with P in agreement with the light scattering data. As before, there is a slight discrepancy at lower pressure for swollen particles due to the presence of peripheral chains. This is confirmed by the approach of both SANS and DLS data at higher values of P, when the particle is increasingly deswollen and these chains are expected to have collapsed.

We can also inquire on the pressure dependence of the polymer mesh size, ξ. It decreases as the particle deswells, as showing in Fig.48b. Quantitatively, this decrease

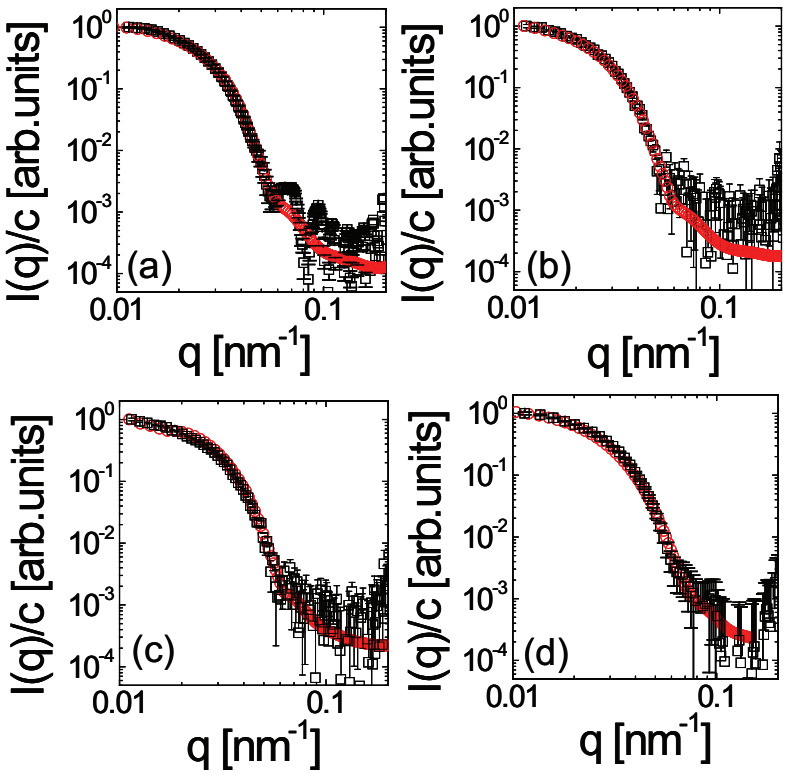

Figure 47: Analogy between temperature and hydrostatic pressure: (a) (○) $T = 25$°C, (□) $P = 0$; (b) (○) $T = 27$°C, (□) $P = 100$MPa; (c) (○) $T = 30$°C, (□) $P = 200$MPa; (d) (○) $T = 35$°C, (□) $P = 250$MPa.

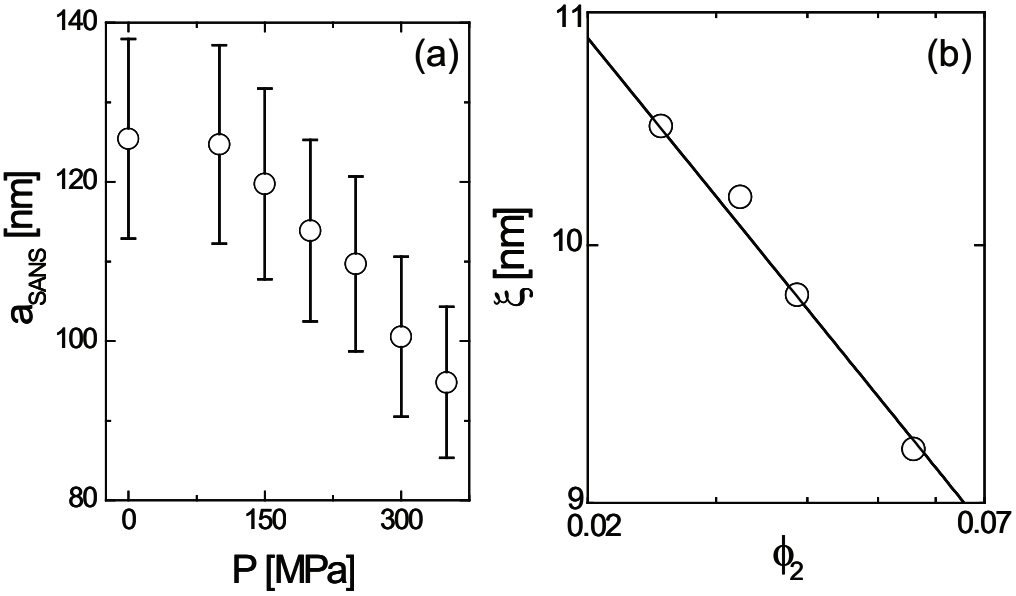

Figure 48: (a) a_{SANS} versus hydrostatic pressure. (b) ξ as a function of polymer volume fraction ϕ_2.

is related to the decrease in the quality of the solvent, which is the ultimate cause of deswelling for these particles. To quantify the change in ζ, we plot our results as a function of the polymer volume fraction within the particle, which we estimate considering that:

$$\frac{\phi_2}{\phi_{2,0}} = (\frac{a_{DLS,0}}{a_{DLS}})^3 \tag{131}$$

with $\phi_{2,0} = 0.8$ [48, 142, 161, 166] and $a_{DLS,0}$ are the polymer volume fraction and the particle size in the deswollen state. We find that $\xi \sim \phi_2^{-0.15}$, which is consistent with what is found in temperature deswelling experiments with similar microgels [144].

5.3.3 Determination of ζ from particle concentration: Viscosity Measurements

The determination of the volume fraction in microgel suspensions is more complicated than for hard sphere suspensions. We already defined the generalized volume fraction, ζ, as:

$$\zeta = \frac{N}{V} V_{1p}^{c->0} \tag{132}$$

where N/V is the number of particles per unit volume and $V_{1p}^{c->0}$ is the volume of one particle measured in dilute suspension. The number of particles in the system can be calculated as:

$$N = \frac{m_{pol}}{m_{pol,1p}} \tag{133}$$

where m_{pol} is the total mass of polymer and $m_{pol,1p}$ is the mass of polymer in one particle. The determination of the last quantity is what adds uncertainty to the calculation of ζ. We can express $m_{pol,1p}$ as:

$$m_{pol,1p} = \phi_{2,0}\rho_0 V_{1p}^0 \tag{134}$$

where $\phi_{2,0}$, ρ_0 and V_{1p}^0 are the polymer weight fraction, the density and the volume of the particle in the collapsed state, where there is no solvent in the particle. Determining $\phi_{2,0}$ is not an obvious task. At high temperature, pNIPAM particles are still known to contain a large amount of solvent [167, 168]. As a result, this deswollen size cannot be used as a measure of the collapsed size. For some microgels the size measured by transmission electron microscopy (TEM) provides a reasonable estimate of the collapsed size [142]. However, for NIPAM microgels, this does not apply; the particles still retain a size larger than its collapsed size even after removal of the solvent [167].

To overcome these limitations, we measure the viscosity for dilute solutions. It is well known that the relative viscosity of dilute solutions is related to the particle volume fraction through the Einstein expression with a correction by Batchelor [170, 171]:

$$\frac{\eta}{\eta_0} = 1 + 2.5\zeta + 5.9\zeta^2 \tag{135}$$

where η is the solution viscosity and η_0 the solvent viscosity. The combination of Eq.132,133 and 134 yields:

$$\zeta = \frac{\rho^{sol}}{\phi_{2,0}\rho_0}(\frac{R}{R_0})^3 c_{pol} = k c_{pol} \tag{136}$$

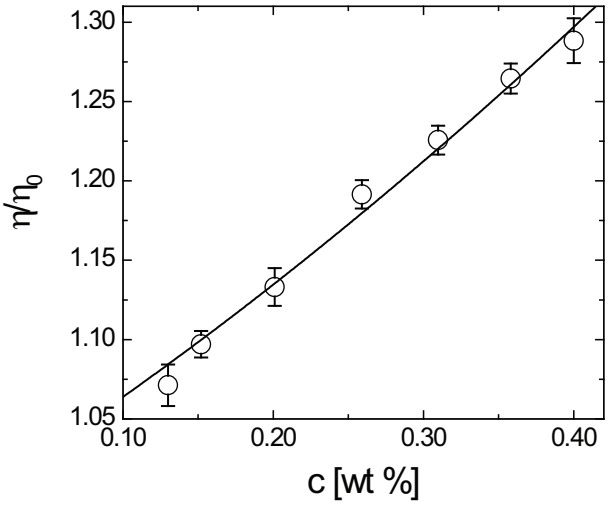

Figure 49: Relative viscosity of the pNIPAM-AAc microgels as a function of polymer concentration. The line represents the best fit to Eq.135

where c_{pol} is the polymer concentration, ρ^{sol} is the density of the solution and R the particle size. This equation can be used in Eq.135 to fit viscosity measurements as a function of polymer concentration. The only free parameter is k, which relates the polymer concentration with the volume fraction. The viscosity measurements are performed on diluted microgel solutions at pD=4.5, using a Cannon-Feske viscometer. It works by allowing the suspension to flow down through a cylindrical capillary into a lower reservoir. While the liquid falls, a Poseuille flow is established. Thus,

$$\frac{\Delta j}{\Delta t} = \frac{\pi R^4}{8\eta}\frac{|\Delta P|}{L} \tag{137}$$

where $\frac{\Delta j}{\Delta t}$ is the volume of fluid per unit of time flowing through a circular cross section of radius, R, in the presence of a pressure gradient $\frac{|\Delta P|}{L}$. By measuring the time it takes the fluid to travel a certain distance along the capillary and by using a previous calibration with a fluid of known viscosity to determine the prefactor relating time and viscosity, we quantify the viscosity dependence with polymer concentration, which we plot in Fig.49 for T=25 and P=0. The relative viscosity increases with polymer concentration, consistent with the increase in the particle volume fraction of the system. We fit the experimental points to Eq.135 combined with Eq.136 leaving k

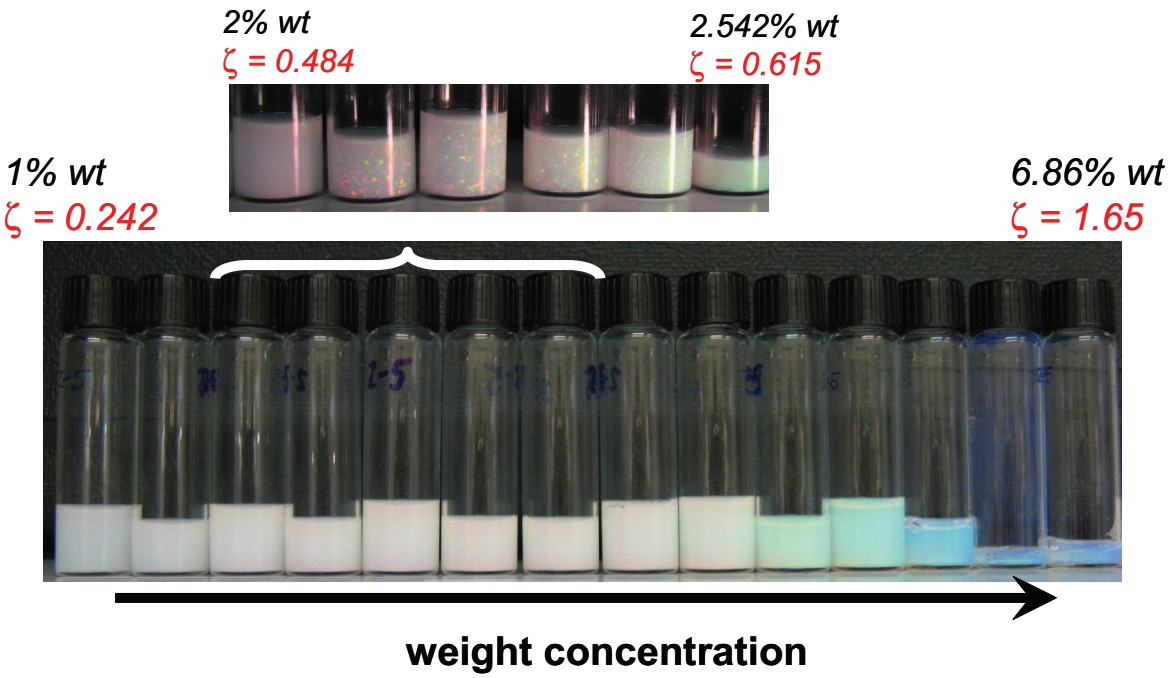

Figure 50: Phase Behavior of the pNIPAM-Acc system as a function of polymer concentration (or particle volume fraction). The phase diagram resembles that of hard spheres.

as free parameter, k. The fit yields a value of $k = 24.2 \pm 0.5$. By using this value, we can obtain $\phi_{2,o}$ from Eq.136 using $\rho^{sol} \approx 1$ g/cm^3 and $\rho_0 \approx \phi_{2,0}\rho^{pol} + (1-\phi_{2,0})\rho^{sol}$, with $\rho^{pol} \approx 1.27$ g/cm^3 the density of the polymer network [169]. We obtain $\phi_0 = 0.56$, which is similar but slightly smaller than what is previously reported for NIPAM-based systems [48, 142, 161, 166, 168]. Since the experiments were performed at pD=4.5, where the Acrylic acid network is partially ionized, we could expect the additional osmotic pressure resulting from this factor to give rise to a deswollen microgel size that is slightly larger than that of a neutral particle.

5.4 Phase Diagram

The conversion between polymer concentration and generalized volume fraction is done using Eq.136, with $k = 24.2$, as obtained from the fit to Eq.135. There is a clear resemblance between the phase behavior of this system and that of hard spheres. The system is liquid for $\zeta < 0.484$ and glassy for $\zeta > 0.615$, as shown in Fig.50. In between,

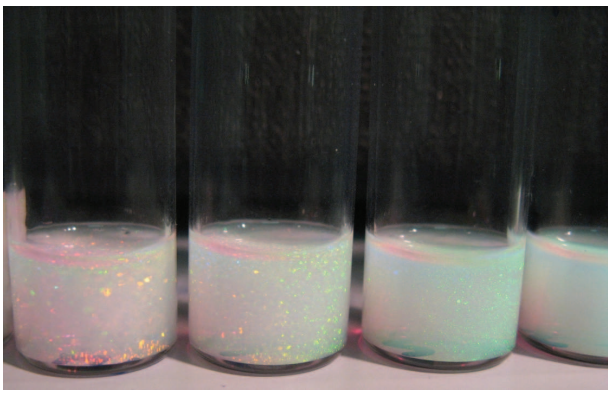

Figure 51: Close-up of several samples that form crystals. The volume fractions are, from left to right, $\zeta = 0.557$, $\zeta = 0.572$, $\zeta = 0.615$ and $\zeta = 0.638$. The size of the crystallites decreases with ζ.

the samples contain crystals which Bragg diffract the incident light giving rise to beautiful iridescence, as shown in Fig.51. For hard sphere suspensions, crystallization occurs at $\phi = 0.495$ and the glass transition happens at $\phi = 0.58$, in close agreement with what is found for this microgel suspension. We further address the structural properties of the system in the crystal and glassy phase by performing small angle neutron scattering experiments.

5.4.1 Crystals

Visual inspection of the crystal samples indicate that the size of the crystals decreases as ζ increases (Fig.51), consistent with previous observations in hard sphere suspensions [172], and reflecting that by increasing ζ the number of nucleation points in the sample increases, further resulting in the formation of more, but smaller crystals. The scattered intensity from these samples is characterized by a distinctive peak $q \approx 0.025$ nm^{-1}, as shown in Fig.52a. From $I(q)$, we obtain the structure factor after normalization with the model form factor described in Section 5.3.2; we use the parameters in the form factor model corresponding to T=25^{o}C and P=0, which were determined at low ζ. We obtain $S(q)$ using:

$$\frac{I(q)/c}{I(q)_{dilute}/c_{dilute}} \tag{138}$$

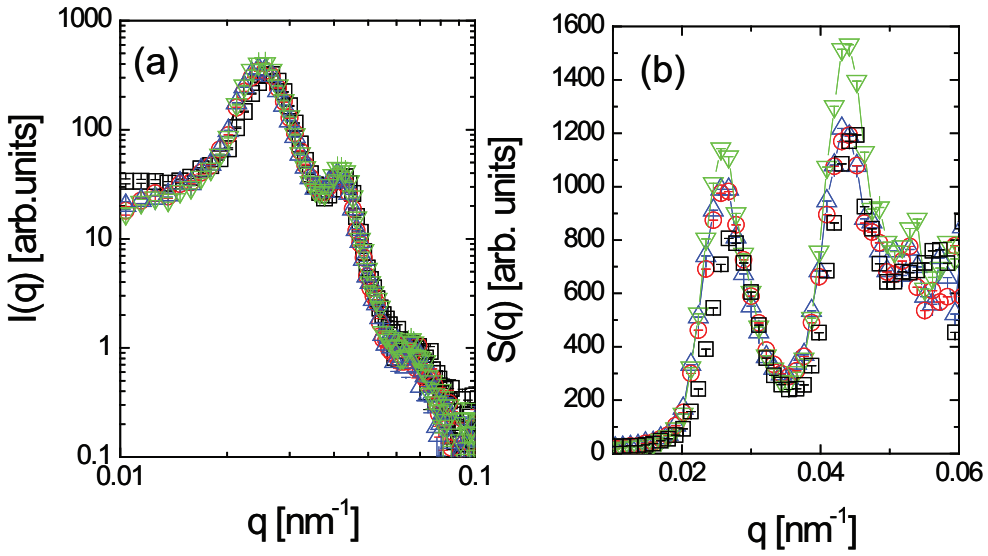

Figure 52: a) Intensity and b) Structure factor profiles for different crystalline samples: ($\triangle$) $\zeta = 0.516$, ($\circ$) $\zeta = 0.547$, ($\triangledown$) $\zeta = 0.558$, ($\square$) $\zeta = 0.572$

.

There are two very distinctive peaks in $S(q)$ for all samples, as shown in Fig.52(b). Note that the units in $S(q)$ are arbitrary units. This results from differences in the experimental set-up when measuring concentrated and dilute samples and from possible changes in the scattering contrast of the samples with ζ.

The first striking feature of the experimental $S(q)$ is the lack of sharp Bragg reflections. Instead, there are two broad peaks within the experimentally accesible q-range. This results from the limited q resolution of a SANS instrument, which mainly results from the wavelength spread of the neutrons. As a result, in order to describe the experimental data, we replace the structure factor of a polycrystal sample, exhibiting Bragg reflections at wavevectors fulfilling the Bragg condition, $q = q_{hkl}$, with q_{hkl}, the reciprocal lattice vector with Miller indexes (h, k, l) [173], by a model that associates a width equal to the q-resolution of the instrument, $\Delta q/q \approx 0.1$ to each Bragg peak. Therefore, each Bragg peak is replaced by a Gaussian function

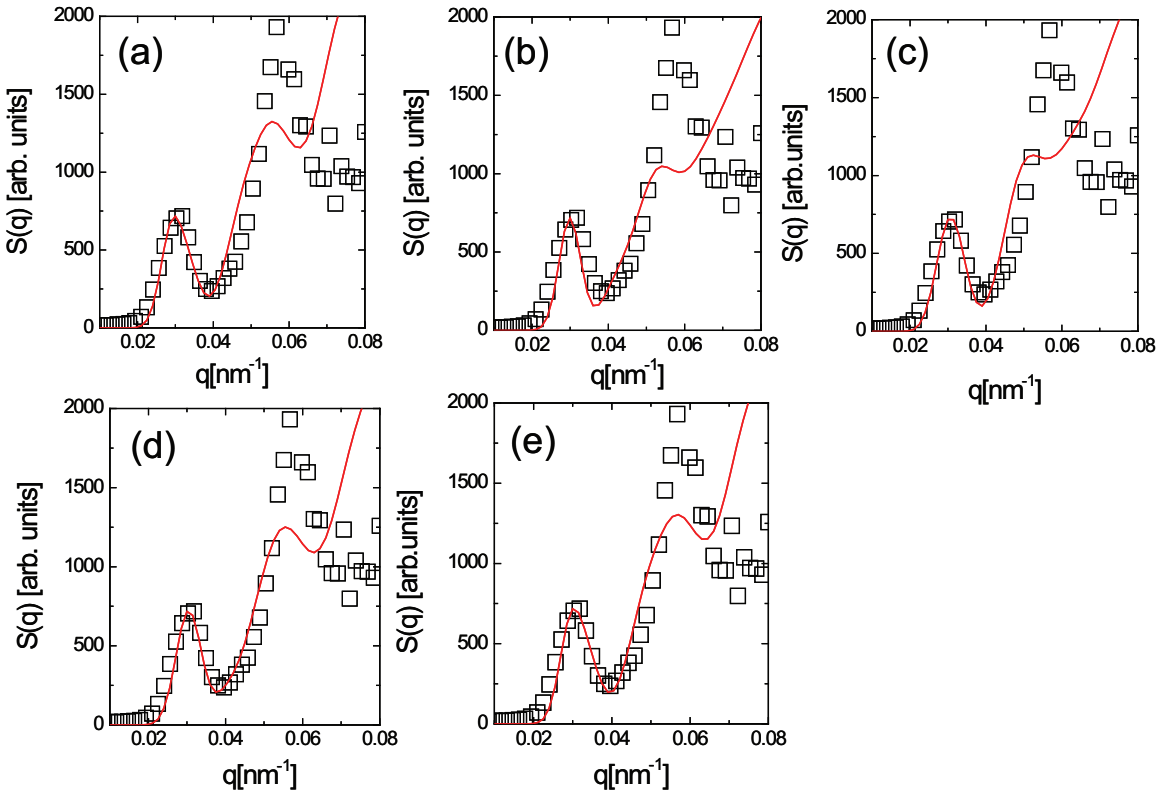

Figure 53: SANS measurement for $\zeta = 0.638$. The measurement is compared with fits for (a) fcc, (b) bcc, (c) A15, (d) hcp, and (e) rhcp structures represented by the solid lines.

centered at q_{hkl}. The structure factor then becomes:

$$S(q) = \sum_i e^{-\frac{(q-q_{hkl})}{\sqrt{2}\Delta q}} \tag{139}$$

We fit our experimental results using Eq.139 to several crystal structures: fcc, bcc, A15, hcp and rhcp. For all of them, we assume an underlying simple cubic lattice, with lattice constant, $\bar{l}$, and a corresponding basis. The fits are performed by selecting $\bar{l}$ so that the position and height of the first peak agrees with the experimental result. The rest of the curve follows thereafter without any further adjustments. The selected structures are common in colloidal systems. The bcc structure is observed at low volume fractions and for charged colloids [174, 175], while the fcc, the hcp and the rhcp are seen at high ϕ [177, 178]. We build the random close packing configurations by randomly mixing face centered cubic (fcc) and hexagonal close packing (hcp) lattices.

Table 5: Lattice parameter, $\bar{l}$, and nearest neighbor distances for several crystalline structures

	fcc	bcc	A15	hcp	rhcp
$\bar{l}$	410nm	320nm	520nm	290nm	$290nm$
nnd	$= \frac{\bar{l}}{\sqrt{2}} = 290\text{nm}$	$= \frac{\sqrt{3}\bar{l}}{2} = 277\text{nm}$	$= \sqrt{\frac{5}{16}}\bar{l} = 290\text{nm}$	$= \bar{l} = 290\text{nm}$	$= \bar{l} = 290\text{nm}$

The A15 structure, which is a bcc lattice with eight basis particles, is predicted to be the configuration minimizing the contact area between particles; it has been observed for dendritic polymers [176].

All fits of the experimental data are equally satisfactory, as can be seen in Fig.53 for the sample $\zeta = 0.638$ as a representative example. Furthermore, the values of $\bar{l}$ from the fits result in nearest neighbor distances which are all in agreement with the particle diameter measured in dilute suspension, $2a = 285\text{nm}$, as shown in Table 5.4.1. This agreement supports the lack of deswelling at these ζ, consistent with the results in Chapter 3.

In addition, it emphasizes the reasonableness of the form factor of the particles at the high ζ values corresponding to crystallization, which assumes that the particles do not appreciably change with respect to dilute conditions. The deviation between the experiment and the model at high q most likely results from deviations in the form factor measured at high ζ compared to the form factor measure at low ζ. In addition, the limited resolution in q prevents elucidation of the crystal structure [179]. Contrast matching experiments are under way in order to directly measure $P(q)$ at high ζ.

5.4.1.1 Crystal Formation

In order to address the kinetics of crystallization, we melt the previously formed crystals by vigorously shaking the sample and measure $I(q)$ as a function of time,

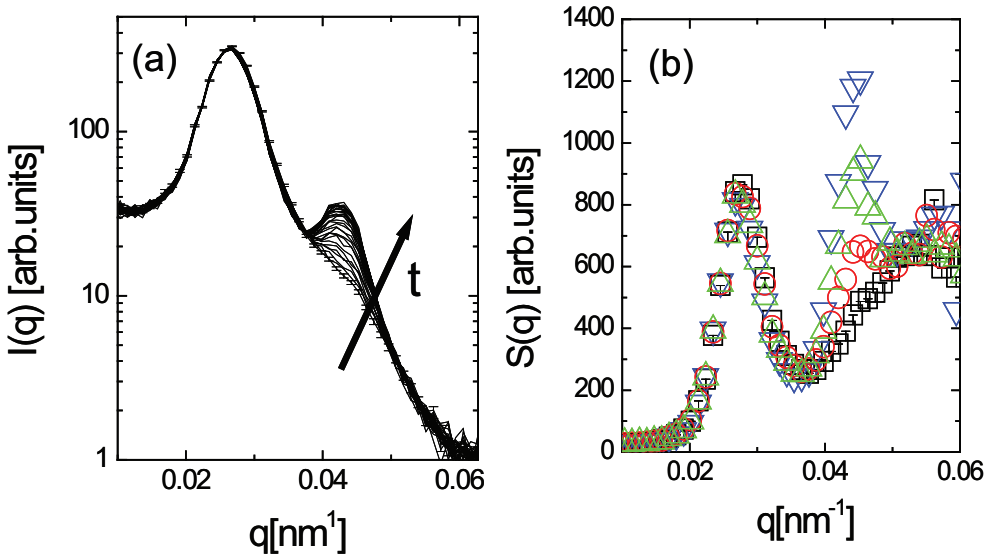

Figure 54: a) Time evolution of the Intensity profiles and b) Selected Structure Factor profiles at several times for the crystalline sample at $\zeta = 0.572$.

as shown in Fig.54a for the sample at $\zeta = 0.572$. Surprinsingly, the first peak in $I(q)$ remains unaltered in time, while the secondary peak appears and subsequently grows at $q \approx 0.042$ nm^{-1}, as shown in Fig.54a. From $I(q)$ we use the form factor model for the particles to obtain the structure factor, which we show Fig.54b for several representative times. Consistent with the $I(q)$ data, the first peak located at $q \approx 0.025$ nm^{-1}, remains unaltered, while the second peak appears and grows in height.

The position of the first peak correspond to a characteristic distance of $\bar{d} = \frac{2\,\pi}{q_{peak}} =$ 250nm, which is in excellent agreement with the mean interparticle distance at the expected ζ, $\bar{d} \approx (N/V)^{-1/3} = (\frac{\zeta}{V_{1p}})^{-1/3} = 270$nm. As a result, this peak is located at a q corresponding to the $S(q)$ of the colloidal liquid for the same ζ. The first peak in the $S(q)$ of the crystal will grow on top of this peak. The lack of displacement of this peak could reflect that the sample has not fully crystallized yet and contains a large fraction of colloidal liquid. This liquid contributes to the observed $S(q)$ and prevents the observation of the crystal contributions to it. Presumably, at longer

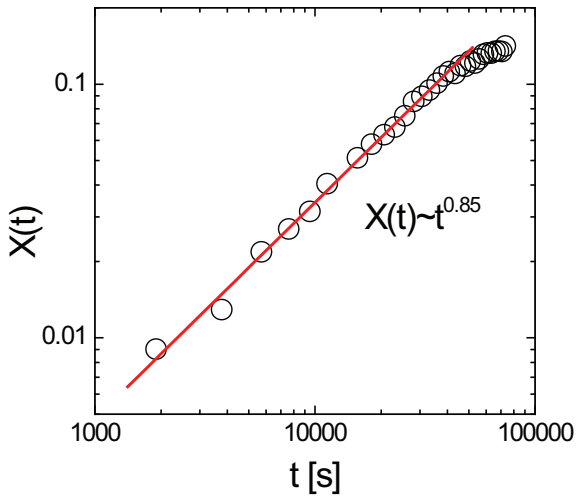

Figure 55: Crystallinity Degree, X(t), as a function of time. X(t) follows a power law with exponent ~ 0.85.

times, this peak would grow, when the crystal contribution to the peak overrides the contribution from the colloidal liquid.

By contrast, since the second peak is located at a q between the first and the second peak of the $S(q)$ of the liquid, the presence of even a small fraction of crystal causes its appearance and its subsequent growth. The crystallization kinetics can, thus, be followed by monitoring the evolution of this peak with time. We calculate the degree os crystallinity in the sample, defined as the area under the peak in the structure factor as [172]:

$$X(t) = \int_{peak} S(q)dq \tag{140}$$

We find that $X(t)$ grows with time following a power-law behavior, $X(t) \sim t^{\alpha}$, as shown in Fig.55. At long times, however, the growth levels off. A similar power law behavior was reported for a suspension of hard spheres at $\zeta = 0.572$ with $\alpha \approx 1.1$.

5.4.1.2 Pressure effects

We have quantified the effect of hydrostatic pressure over the structural properties of a crystal by measuring the scattered intensity as a function of q for different values of P for a sample of $\zeta = 0.638$. With increasing P, the scattered intensity increases

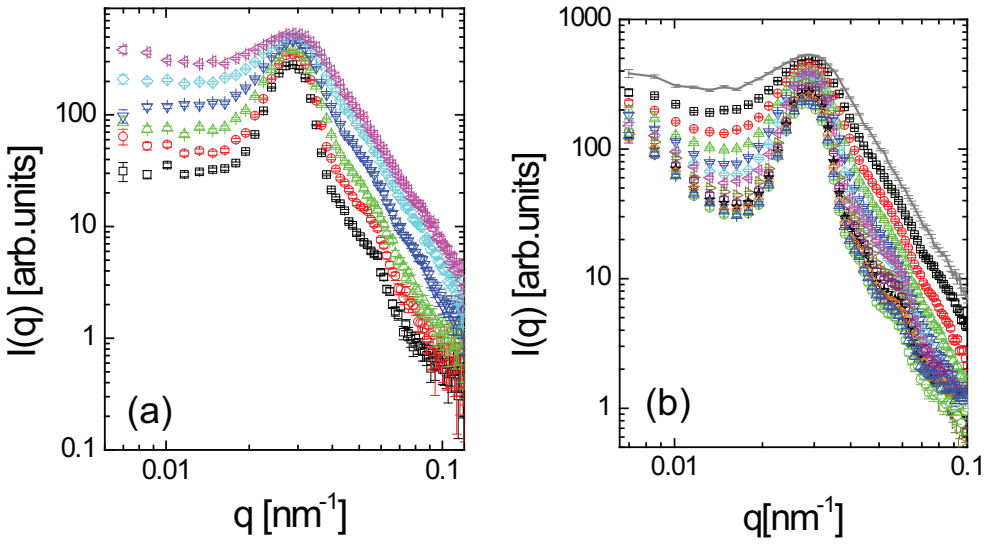

Figure 56: Intensity profile for different hydrostatic pressures: a) Increasing pressure (□) $P = 0$, (○) $P = 100$MPa, (△) $P = 150$MPa, (▽) $P = 200$MPa, (◇) $P = 200$MPa, (◁) $P = 300$MPa; b) Decreasing pressure: (○) $P = 0$, (△) $P = 25$MPa, (○) $P = 50$MPa, (⋆) $P = 75$MPa, (○) $P = 100$MPa, (▷) $P = 125$MPa, (◁) $P = 150$MPa, (◇) $P = 175$MPa, (▽) $P = 200$MPa, (△) $P = 225$MPa, (○) $P = 250$MPa, (□) $P = 275$MPa, (–) $P = 300$MPa

in value as a result of the larger contrast of the high P-deswollen particles compared to the low-P swollen particles. In addition, while at low P, there is a shoulder at $q \approx 0.06\text{nm}^{-1}$, at higher pressure, $I(q)$ decays monotonically with q in this q-region, as shown in Fig.56a. This also results from the pressure induced deswelling, which lowers ζ, washing away the structural features of the crystal and eventually, at high P, melting the crystal into a liquid phase.

We performed additional experiments by lowering the pressure from 300MPa to 0, as shown in Fig.56. Similar results were obtained, as shown in Fig.57 for P=0 and P=100MPa, as representative examples.

From $I(q)$, we obtain the structure factor, $S(q)$, using the form factor model at the corresponding hydrostatic pressure. Consistent with our previous results, there is a peak at $q \approx 0.033$ nm^{-1}, which essentially remains unaltered until eventually disappearing at P=300MPa, and there is a second peak at larger q which shifts to

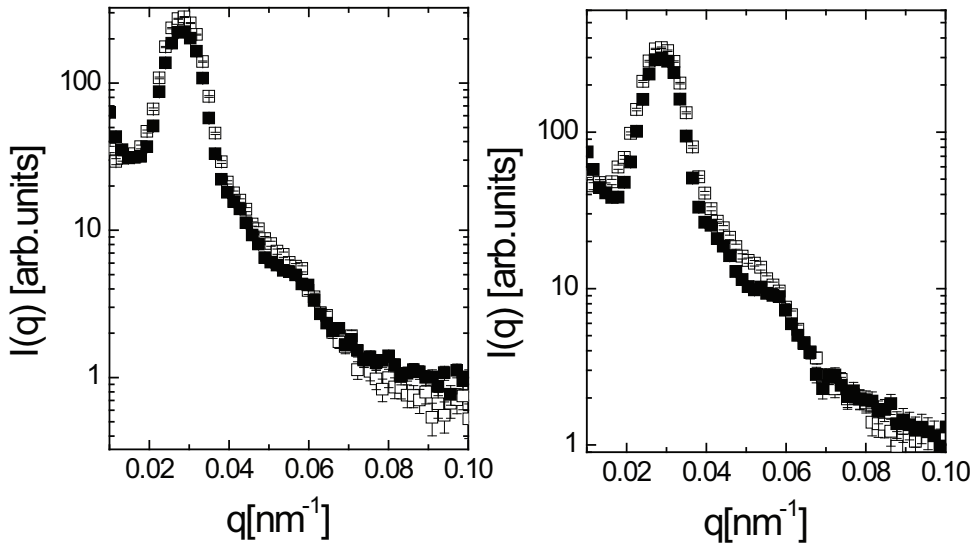

Figure 57: Intensity profiles for P=0 before (□) and after (■) increasing the hydrostatic pressure for a)P=0 and b) P=100 MPa.

higher q as the hydrostatic pressure is increased. The second peak in this crystal sample is located at larger q compared to other crystal samples at lower ζ for reasons we do not fully understand yet. We note that we confirmed the presence of crystals in the pressure cell where the SANS experiments were done, visually to rule out the lack of crystallization in the sample when performing these experiments. Remarkably, this peak is located at $q \approx 2\pi/a$, where we would approximately expect the second peak of the colloidal liquid at this ζ. To quantify the shift in q of the peak, we fit the region around the peak to a Gaussian function and plot the center of the Gaussian as a function of ζ. We find it decreases as the particle shrinks with increasing pressure. The position of the peak remains essentially constant as ζ decreases up to $\zeta \approx 0.49$, where it appreciably displaces to higher q, as shown in Fig.59. We note that the crossover ζ approximately corresponds to the ζ value where melting is expected (Fig.50). Below this ζ, the system is expected to be a liquid. We thus, calculate the expected evolution of the second peak in the structure factor of hard spheres as the volume fraction decreases by changing the particle size while keeping the particle

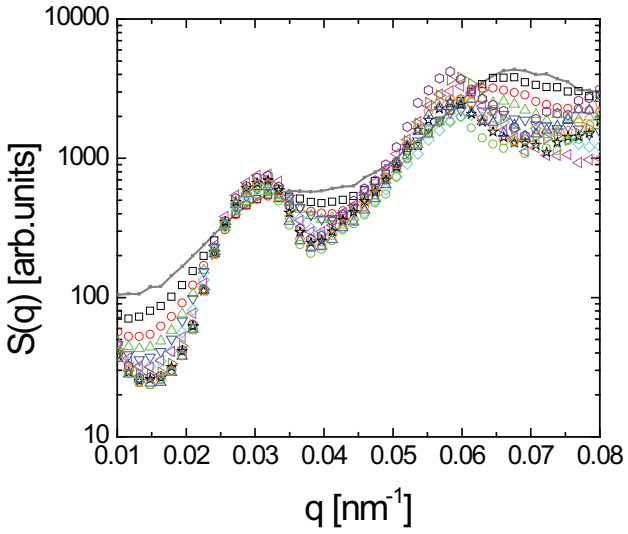

Figure 58: Structure factor profiles for different hydrostatic pressures: (○) $P = 0$, (△) $P = 25$MPa, (○) $P = 50$MPa, (⋆) $P = 75$MPa, (○) $P = 100$MPa, (▷) $P = 125$MPa, (◁) $P = 150$MPa, (◇) $P = 175$MPa, (▽) $P = 200$MPa, (△) $P = 225$MPa, (○) $P = 250$MPa, (□) $P = 275$MPa, (–) $P = 300$MPa

concentration constant. We model the hard sphere structure factor using a Percus-Yevick approximation [180] that allows an analytical expression for $S(q)$:

$$S(q) = \frac{1}{1 + 24\zeta G/qa} \tag{141}$$

where G = PY1+PY2 + PY3, with:

$PY1 = \alpha[\sin(qa) - qa\cos(qa)]/(qa)^2$,

$PY2 = \beta[2qa\sin(qa) + [2 - (qa)^2]\cos(qa) - 2]/(qa)^3$,

$PY3 = \gamma[-(qa)^4\cos(qa) + 4[(3(qa)^2 - 6)cos(qa) + [(qa)^3 - 6qa]\sin(qa) + 6]]/(qa)^5$,

and with,

$\alpha = [(1 + 2\zeta)^2]/(1 - \zeta)^4$, $\beta = -6\zeta[(1 + \zeta/2)^2]/(1 - \zeta)^4$ and $\gamma = \zeta\alpha/2$.

This model quantitatively captures the second peak we observe in our experiments, as shown in Fig.59, emphasizing the analogies between our system of microgels and the corresponding hard sphere system.

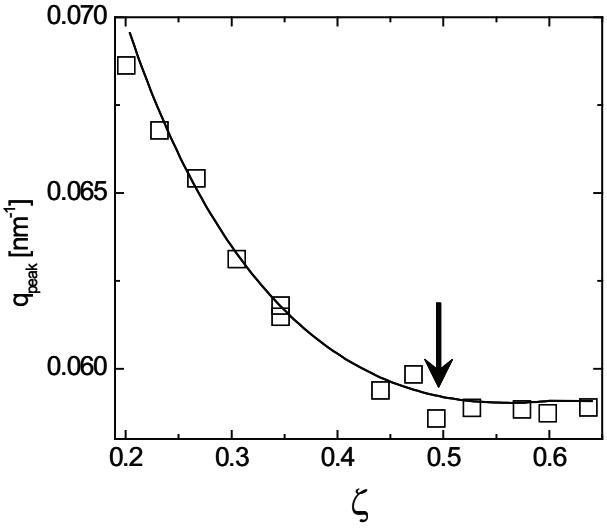

Figure 59: Evolution of the second peak position in Fig.58 as a function of volume fraction. The solid line represents the expected evolution for hard spheres. The arrow represents ζ of melting in the phase behavior.

5.4.2 Glassy Samples

We now turn our attention to samples with $\zeta > 0.63$. From $I(q)$, shown in Fig.60a, we obtain $S(q)$ by using the form factor model at the corresponding pressure measure in dilute suspension. As before, the structure factor has a peak at $q \approx 0.033$ nm^{-1}, which remains approximately constant with pressure and a second peak at higher q, which displaces to the right as P increases, as shown in Fig.60b. Remarkably, the height of this peak is significantly larger than the height of the first peak. This is very unusual for samples with liquid-like order, like our glassy samples. Similar results are also seen with other NIPAM suspensions [144]. Recently, this unexpected behavior has been observed in emulsions at volume fractions above ϕ_{rcp} [181, 182]. Simulations with polydisperse particles also reveal a similar behavior [183]. The more ill-defined nearest neighbor distance in polydisperse samples compared to monodisperse samples, results in a structure factor with a first peak having a smaller height than the second peak. From our analysis of the particle form factor, we estimated a polydispersity in the radius of the core of $\sigma_{pol} \approx 0.11 - 0.13$. Thus, our samples have a non-negligible

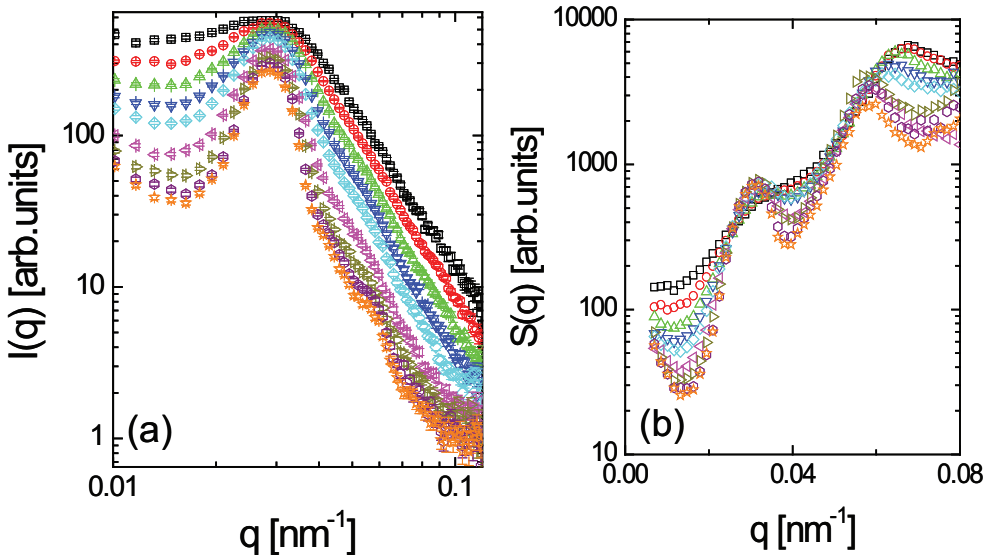

Figure 60: a) Intensity and b) Structure factor profiles for different hydrostatic pressures: ($\star$) $P = 0$, ($\circ$) $P = 50$MPa, ($\triangleright$) $P = 100$MPa, ($\triangleleft$) $P = 150$MPa, ($\Diamond$) $P = 200$MPa, ($\triangledown$) $P = 225$MPa, ($\triangle$) $P = 250$MPa, ($\circ$) $P = 275$MPa, ($\square$) $P = 300$MPa

polydispersity which could be playing a role in our observations. To estimate the structure factor of polydisperse samples, we use the model of Gnoza and Yasutomi [184], which is based on the monodisperse Percus-Yevick model for hard spheres and a polydispersity described by the Schulz distribution:

$$N(a) = a^z/[z(z+1/a_{av})]e^{-a(z+1)/a_{av}} \tag{142}$$

with a_{av} the mean average radius. This distribution is very similar to a Gaussian distribution with a corresponding polydispersity given by the polydispersity index $\frac{1}{1+z}$. The effects of polydispersity are exemplified for $\zeta = 0.77$ and a average particle size of $a_{av} = 118nm$ in Fig.61. As the polydispersity increases, the height of the first peak in $S(q)$ with a concomitant increase of its width. Note that the presence of polydispersity allows tighter packing of particles and thus the achievement of volume fractions higher than ϕ_{rcp} [184].

Using this model, we fit the experimental structure factor at P=0, leaving as free parameters the particle size and the polydispersity index, setting the volume

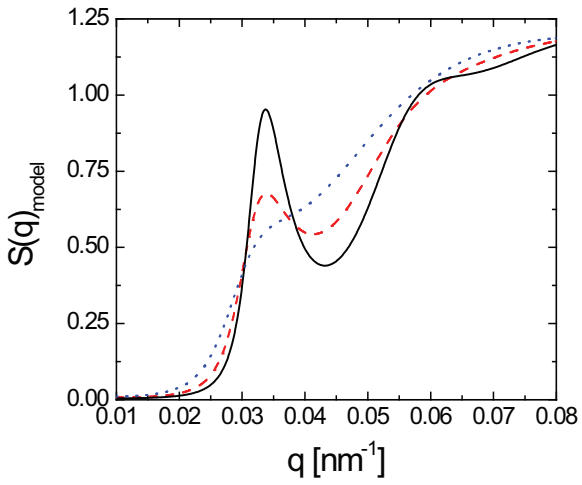

Figure 61: Structure factor obtained from the model for polydisperse $S(q)$. We keep constant $\zeta = 0.77$ and R = 118 nm and change the polydispersity: 0.18 (solid line), 0.22 (dashed line) and 0.28 (dotted line).

fraction of the system at the experimental value of $\zeta = 0.68$ and and dividing $S(q)$ by a constant factor to match the height of the first peak. Although we are able to describe the the initial part of the structure factor, there is not a good overall agreement betwenn the model and the experiment, as shown in Fig.62. Despite this, the values for the average particle size is 135 nm, which agrees with the value measured in dilute suspension and the value for the polydispersity is $\sigma_{pol,model} = 0.25$ which is considerably higher than the value obtained in dilute suspension. This could indicate that for very concentrated microgel suspensions, the soft character of the particles could reflect in an overall polidispersity increase due to particle deformation. As a result, the particle form factor used to obtain $S(q)$ at this high ζ, must be corrected to account for the larger polydispersity. Given that the particle size obtained in SANS resulted from the core and the fuzzy shell, the overall polydispersity of the suspension must result from the polydispersity in both these quantities. Since $a_{SANS} = a_{av} + 2\sigma$, the total polydispersity of the particles, $\sigma_{pol,aSANS}$, is obtained from the polydispersity in the core σ_{pol} and the polydispersity in the width of the fuzzy region $\sigma_{pol,\sigma}$ [141]:

$$\sigma_{pol,aSANS} a_{SANS} = \sqrt{(\sigma_{pol} a_{av})^2 + 4(\sigma_{pol,\sigma}\sigma)^2} \tag{143}$$

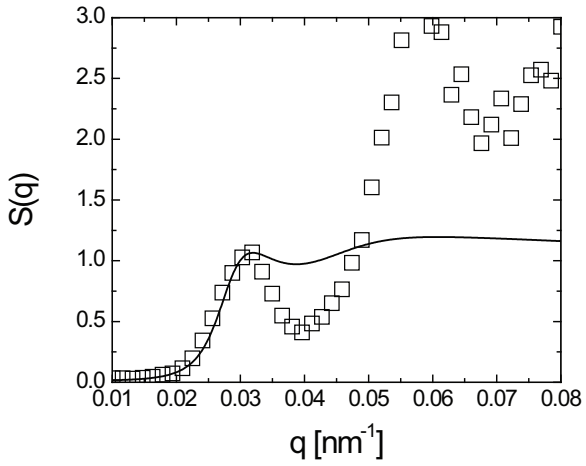

Figure 62: Normalized structure factor and theoretical expectation for $\zeta = 0.68$, R=125nm.

In this calculation, we assume that a_{av} and σ both follow Gaussian distributions. With this in mind, we recalculate the $S(q)$ using a form factor with a polydisperse core and a polydisperse fuzzy region such that the total polydispersity is given by Eq.143 and is equal to the polydispersity we use in the model of $S(q)$. The results for various combinations of σ_{pol} and $\sigma_{pol,\sigma}$ for the experiment at P=0 are shown in Fig.63, together with the expectations of the polydisperse model of hard spheres. We emphasize that in all cases, $\sigma_{pol,aSANS}$ is equal to the polydispersity value used in the theoretical estimation of $S(q)$.

The more consistent way of calculating $S(q)$ from the experimental data results in appreciable differences particularly in the q-range corresponding to the second peak of $S(q)$, as shown in Fig.63. However, we are far from a successful description of the experimental results yet. A better description is required in order to clearly show that the unexpected features of $S(q)$ result from polydispersity.

Similar data analysis and theoretical fits for the other pressures are shown in Fig.64. While the agreement between the experimental results and the model seems to improve as P increases, the values of polydispersity needed to describe the curves increases as well, which we would expect to behave differently.

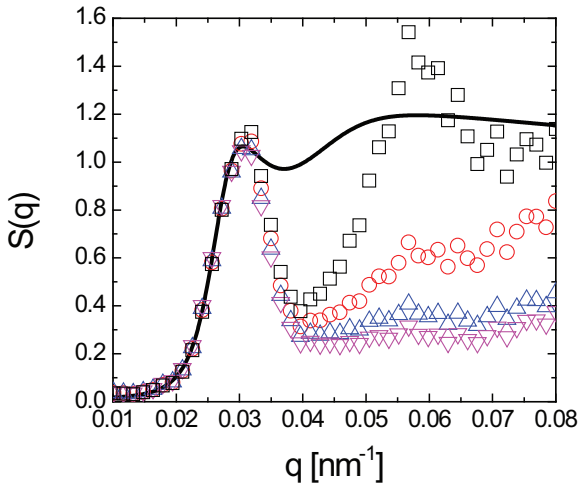

Figure 63: Structure factor for $\zeta = 0.68$ at P=0 and total polydispersity, $\sigma_{pol,aSANS} = 0.25$, obtained using Eq.143: (□) $\sigma_{pol} = 0.15$, $\sigma_{pol,\sigma} = 0.67$; (□) $\sigma_{pol} = 0.22$, $\sigma_{pol,\sigma} = 0.6$; (○) $\sigma_{pol} = 0.28$, $\sigma_{pol,\sigma} = 0.5$; (△) $\sigma_{pol} = 0.35$, $\sigma_{pol,\sigma} = 0.28$. The solid line represent the prediction of the model.

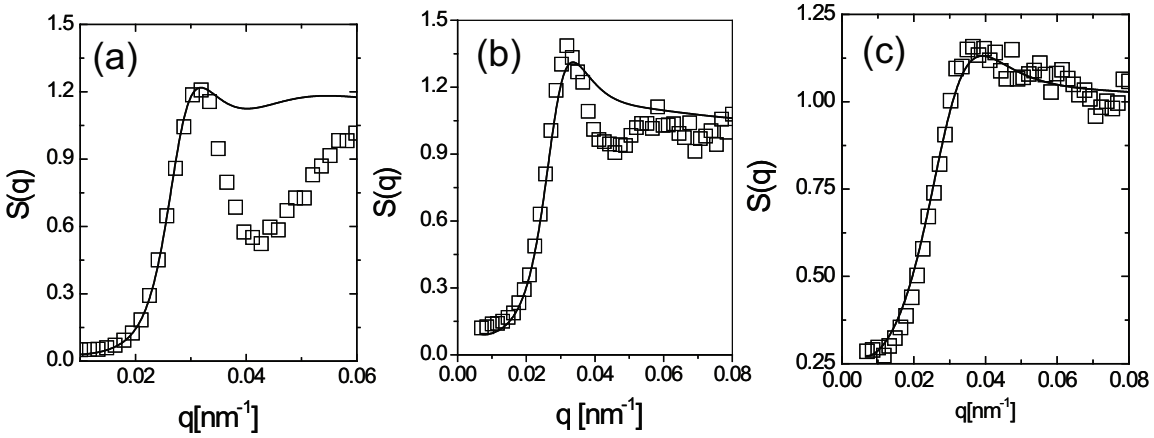

Figure 64: Structure factor and best theoretical expectation for a) P=100MPa: $\sigma_{pol,aSANS} = 0.27$, $\sigma_{pol} = 0.22$ and $\sigma_{pol,\sigma} = 0.67$; b) P=200MPa: $\sigma_{pol,aSANS} = 0.29$, $\sigma_{pol} = 0.3$ and $\sigma_{pol,\sigma} = 0.61$; c) P=300MPa: $\sigma_{pol,aSANS} = 0.3$, $\sigma_{pol} = 0.35$ and $\sigma_{pol,\sigma} = 0.6$.

5.4.3 Summary and Overview

In this Chapter, we have analyzed the phase behavior of PNIPAM-Acc microgel particles using SANS. From the form factor analysis, we concluded that the samples were polydisperse, with a polydispersity of $\sim 12\%$. However, the samples exhibit formation of crystal phases. Interestingly, the ζ range where crystals are observed is close to the corresponding range in hard sphere suspensions. This could suggest that polydispersity changes with ζ: The entropic penalty associated to this change is compensated from the entropic gain associated to the suspension; the particles change their preferred swelling equilibrium size to adjust the polydispersity so that they can crystallize and exhibit hard sphere suspension behavior. We note that similar behavior was observed before, where microgel suspensions with polydispersities of even 14% were observed to crystallize into beautiful opals [185, 186].

At larger ζ, the system exhibits glassy phases with unusual structure factors that do not resemble those of hard sphere suspension. Similar results have been observed in the past and interpreted by assuming particle deswelling at volume fractions as low as $\phi \approx 0.3$ [144]. A result of this assumption is that the form factor measured in dilute conditions cannot be used to describe the microgel particle in a concentrated suspension. While it is likely that the form factor in dilute and concentrated suspensions is different due to particle deformation and certainly due to shrinking above $\zeta = 1$, our results in Chapter 3 suggest that deswelling at lower ζ does not occur. Moreover, recent sedimentation experiments with NIPAM microgels are in line with this conclusion [187]. Based on this fact, we interpret the unusual $S(q)$, obtained by normalizing with the particle form factor measured in dilute suspension, using a polydisperse hard sphere model that successfully describes the $S(q)$ of very concentrated polydisperse emulsions. We exemplify the results using one of the structure factors obtained in [144]. By fitting these data to the polydisperse hard sphere model, we obtain a polydispersity of $\sigma = 0.19$. The overall agreement between the model and

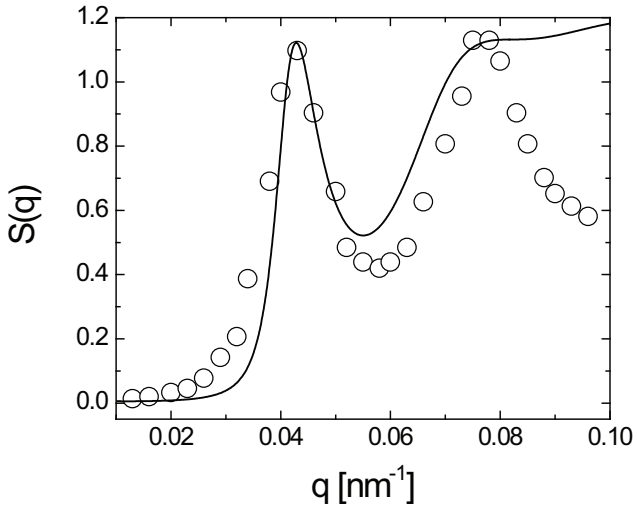

Figure 65: Comparison of the model with a published *strange* structure factor from [144]. The experimental parameters are $\phi = 0.65$ and a = 84nm and the model parameters are $\zeta = 0.71$, $a_{av} = 91$nm and polydispersity of 0.19.

the data is good; the model correctly captures the presence of the two peaks and the fact that the height of the second peak is similar to the height of the first peak. However, it fails to reproduce the decay of $S(q)$ at large q, as shown in Fig.65; this could very well reflect the deformation of the particles, emphasizing that a better form factor is needed to obtain $S(q)$ from $I(q)$. The fit corresponds to a volume fraction and average particle radius of $\zeta = 0.71$ and $a_{av} = 91$nm, which should be compared with the values 0.65 and 84 nm provided for the data [144]. This comparison shows that polydispersity can indeed affect the phase behavior and structural properties of microgel suspensions. The corresponding results for our microgel samples, however, show a more dramatic difference between the model and the experimental data. This prevents definite conclusions about this effect in our samples. More work is currently underway in order to better understand the discrepancies between our data and the polydisperse hard sphere model.

CHAPTER VI

CONCLUSIONS

From this Thesis we can extract the following conclusions:

- The viscosity and structural relaxation time of very slightly cross-linked microgels display a *strong* approach to the glass, in the form of an Arrhenius behavior with ζ, for all experimentally accessible ζ. This is clearly different from hard sphere behavior.

- The almost linear dependence of the viscosity and the structural relaxation time suggests that the local elasticity of the system remains constant as ζ increases. This has analogies in molecular glass formers: While the relaxation of *fragile* glass formers involves many particles, the relaxation of *strong* glass formers, like silica, is thought of as being local. Our results suggest that the local elasticity is what governs the relaxation of *strong* glass formers.

- The local elasticity involved in the structural relaxation of these microgel suspensions, which is constant with ζ, can be understood as resulting from the interpenetration of the outer polyelectrolyte chains of the particles. This interpenetration then determines the fragility of our microgel suspension. Our results suggest that this could also be the case for other microgel systems.

- The osmotic pressure of microgel suspensions becomes equal to the particle bulk modulus around $\zeta = 1$. This implies that particle deswelling cannot take place for smaller values of ζ. Given that this microgel suspension exhibits a liquid-to-glass transition at $\zeta = 1$, we conclude that particle deswelling cannot take place at volume fractions below the liquid-to-solid transition of a microgel

suspension.

- The elastic modulus, the osmotic pressure and the compressional modulus of the solution all exhibit a similar ζ-dependence, when normalized by the particle bulk modulus. They all increase for $\zeta < 1$ and remain essentially constant for $\zeta \geq 1$. This is analogous to what it is observed in emulsions. However, unlike emulsions, the compressional modulus of the solution is several orders of magnitude larger than the elastic modulus of the system. This reflects the difference between shear or compression in a packed microgel suspension. By modeling the microgel as a set of springs, we conclude that, whereas all the springs participate in a compression, only those in the periphery of the particles participate against a shear deformation. This gives rise to the large difference in the corresponding moduli that is observed for microgel suspensions.

- Hydrostatic pressure is an effective means to deswell poly(N-isopropylacrylamide) microgel particles. Increasing the external pressure decreases the mixing of the polymer with the solvent causing a decrease in the particle size; this is similar to temperature-induced deswelling. However, shrinking with pressure occurs in a more gradual way as compared with temperature.

- The analogy between hydrostatic pressure and temperature can be extended to the particle form factor. As a result, both quantities modify the mixing of the polymer, induce similar deswelling and similar structural changes in the microgel particles.

- The form factor of pNIPAM-Acc microgels can be described as a compact core with a fuzzy surface and with internal inhomogeneities associated with the polyelectrolyte chains.

- Our interpretation for the phase behavior of pNIPAM-Acc packed suspensions

relies on polydispersity changes, which are possible due to the intrinsic particle softness. This happens in a way such that the overall phase behavior resembles that of hard sphere suspensions.

REFERENCES

[1] P.G. de Gennes, Nobel Prize acceptance speech, 1991

[2] S. Croll, Prog. Org. Coat. 44, **131** (2002).

[3] A. D. Dinsmore, M. F. Hsu, M. G. Nikolaides et al, Science **298**, 1006 (2002).

[4] ed: E. Dickinson, *Food emulsions and foams*, Royal society chemistry, Cambridge, 1999.

[5] F. Caruso, Chem. A **6**, 413 (2000).

[6] M. Yoon, J.A. Chang, Y. Kim et al, J. Phys. Chem. B **105**, 2539 (2001).

[7] Frank Caruso, *Colloid and Colloidal Assembly: Synthesis, Modification, Organization and Utilization*, Wiley, New York, United States, 2004.

[8] Lucretius, *On the nature of things*, Penguin, London, United Kingdom, 2007.

[9] ed. J.J. Bennett *The Miscellaneous Botanical Works of Robert Brown*, 1, 463-486, Roy Soc. London, (1866).

[10] A.Einstein, *Investigations on the Theory of Brownian Movement* Dover, New York, USA, 1956

[11] M. Smoluchowski, Annalen der Physik, **21**, 756 (1908).

[12] G.D.R.Midi, Eur.Phys.J.E, t**14**, 341, (2004).

[13] J.M.Ottino, D.V.Khakhar, Ann.Rev. Fluid. Mech, **32**, 55, (2000).

[14] U.Gasser, E.R.Weeks, A.Schofield et al, Science, **292**, 258, (2001).

[15] K.N.Pham, A.M.Puertas, J.Bergenholtz et al, Science, **296**, 104, (2002).

[16] P.Schall, I.Cohen, D.A.Weitz et al, Science, **305**, 1944, (2004).

[17] A.M.Alsayed, M.F.Islam, J.Zhang et al, Science, **309**, 1207, (2005).

[18] E.R.Weeks, J.C.Crocker, A.C.Levitt et al, Science, **287**, 627, (2000).

[19] T.Eckert, E.Bartsch, Phys. Rev. Lett., **89**, 125701, (2002).

[20] J.Mattsson, H.M.Wyss, A.Fernandez-Nieves et al., Nature, **462**, 83, (2009).

[21] A.Vrij, E.A.Nieuwenhuis, H.M.Fiknaut, Faraday Discussions, **65**, 101, (1978).

[22] P.N.Pusey, W.van Megen, Nature, **320**, 340, (1986).

[23] E.B.Sirota, H.D.Ouyang, S.K.Sinha et al, Phys. Rev. Lett., **62**, 1524, (1989).

[24] W.K.Kegel, A.van Blaaderen, Science, **287**, 290, (2000).

[25] J.G.Berryman, Phys. Rev. A, **27**, 1053, (1983).

[26] P.Bolhuis, D.Frenkel, J. Chem. Phys, **106**, 666, (1997).

[27] Y.Monovoukas, A.P.Gast, J.Coll. Interface Sci., **128**, 533, (1989).

[28] A.P.Hynninen. M.Dijkstra, R.van Roij, Phys. Rev. E, **69**, 06407, (2004).

[29] M.E.Leunissen, C.G.Christova CG, A.P.Hynninen et al., Nature, **437**, 235, (2005).

[30] D.A.Weitz, M.Oliveria, Phys. Rev. Lett., **52**, 1433, (1984).

[31] P.J.Lu, E.Zaccarelli, F.Ciulla et al, Nature, **453**, 499, (2009).

[32] A.E.Bailey, W.C.K.Poon, R.J.Christianson et al., Phys. Rev. Lett., **99**, 205701, (2007).

[33] A.Loxley, B.Vincent, Colloid Polym. Sci., **275**, 1108, (1997)

[34] I.J.Suarez, A.Fernandez-Nieves, M.Marquez, J. Phys. Chem. B, **110**, 25729, (2006).

[35] S.Nayak, L.ALyon, Angew. Chem. Int. Ed., **44**, 7686, (2005).

[36] M.Das, H.Zhang, E.Kumacheva, Annu. Rev. Mater. Res., **36**, 117, (2006).

[37] A.Fernandez-Barbero, I.J.Suarez, B.Sierra-Martin et al, Adv. Colloid Interface Sci., **147**, 88, (2009).

[38] J.Siepmann, N.A. Peppas, Adv. Drug Delivery Rev., **48**, 139, (2001).

[39] S.V.Vinogradov, T.K. Bronich, A.V.Kabanov, Adv. Drug Delivery Rev., **54**, 135, (2002).

[40] G.E.Morris, B. Vincent,M.J.Snowden, J. Colloid Interface Sci., **190**, 198, (1997).

[41] K.Kajiwara, S.B.Rossmurphy, Nature, **355**, 208, (1992).

[42] J.Gao, Z.B. Hu, Langmuir, **18**, 1360, (2002).

[43] A.J.Wagers, R.T.Sherwood, J.L.Christensen et al, Science, **297**, 2256, (2002).

[44] D.J.Beebe, J.S.Moore, J.M.Bauer et al, Nature, **404**, 588, (2000).

[45] J.C.Lamphere, M.Zweigle, Patent US4172066, 1979; M.J.Snowden, B.Vincent, J.C.Morgan, Patent GB 226 2117A, 1993.

[46] G.Chauveteau, N.Kohler, Soc. Pet. Eng. J., **24**, 361, (1984).

[47] P.J.Flory, *Principles of Polymer Chemistry*, Cornell University Press, London, United Kingdom, 1953.

[48] B. R. Saunders, B. Vincent, J. Chem. Soc.-Faraday Trans. **92**, 3385 (1996).

[49] B. R. Saunders, H. M. Crowther, B. Vincent, Macromolecules, **30**, 482 (1997).

[50] J. L. Barrat, J. F. Joanny, P. Pincus, J. Phys. II, **2**, 1531 (1992).

[51] P.Mohanty, W.Richtering, J.Phys.Chem.B, **112**, 14692, (2008).

[52] E.H.Purnomo, D.van den Ende, S.A.Vanapalli et al, Phys. Rev. Lett, **101**, 238301, (2008).

[53] M.Cloitre, R.Borrega, F.Monti et al, Phys. Rev. Lett, **90**, 068303, (2003).

[54] U.Gasser, B.Sierra-Martin, A.Fernandez-Nieves, Phys. Rev. E, **79**, 051403, (2009).

[55] Z.Y.Meng, J.K.Cho, S.Debord, et al, J.Phys. Chem. B, **111**, 6992, (2009).

[56] Y.L.Han, Y.Shokef, A.M.Alsayed et al, Nature, **456**, 898, (2008).

[57] A.S.Iyer, L.A.Lyon, Angew.Chem. Int. Ed., **48**, 4562, (2009).

[58] D.Gottwald, C.N.Likos, G.Kahl, Phys. Rev. Lett., **92**, 068301, (2004).

[59] D.Gottwald, C.N.Likos, G.Kahl, J.Chem. Phys., **122**, 074903, (2005).

[60] J.R.Seth, M.Cloitre, R.T.Bonnecaze, J.Rheol., **50**, 353, (2006).

[61] T.G.Mason, J.Bibette, D.A.Weitz, Phys. Rev. Lett., **75**, 2051, (1995).

[62] W.van Megen, P.N.Pusey, Phys.Rev.A, **43**, 5429, (1991).

[63] T.G.Mason, D.A.Weitz, Phys.Rev.Lett., **75**, 2770, (1995).

[64] W.K.Kegel, A.van Blaaderen, Science, **287**, 290, (2000).

[65] C.A.Angell, K.L.Ngai, G.B.McKenna et al, J.Appl.Phys., **88**, 3113, (2000).

[66] R.Bohmer, K.L.Ngai, C.A.Angell et al, J.Chem. Phys, **99**, 4201, (1993).

[67] Z.Cheng, J.Zhu, P.M.Chaikin et al, Phys. Rev. E, **65**, 041405, (2002).

[68] T.Hellweg, C.D.Dewhurst, E.Bruckner et al, Coll. Pol. Sci., **278**, 972, (2000).

[69] E.Bartsch, M.Antonietti, W.Schupp et al, J.Chem. Phys., **97**, 3950, (1992).

[70] H.Senff, W.Richtering, J.Chem.Phys., **111**, 1705, (1999).

[71] C.A.Angell, K.Ueno, Nature, **462**, 45, (2009)

[72] J.G.K.Dhont, *An Introduction to the Dynamics of Colloids*, Elsevier, Amsterdam, (1996).

[73] B.J.Berne, R.Pecora, *Dynamic Light Scattering: With Applications to Chemistry, Biology, and Physics*, Dover Publications, London, (2000).

[74] Due to this wavelength dependence, scattering of sunlight from molecules in the atmosphere is more intense at smaller wavelengths. Since the human eye is most sensitive to blue, it is because of this that we perceive the sky as blue[75].

[75] G.S.Smith, Am. J. Phys., **73**, 590, (2005).

[76] J.D.Jackson, *C*lassical Electrodynamics, J.Wiley-Sons, New Jersey, USA, (1999).

[77] I. Teraoka, *Polymer Solutions: An Introduction to Physical Properties*, John Wiley-Sons, Inc., 2002.

[78] D.A.McQuarrie, *S*tatistical Mechanics, Harper-Row, New York, USA, (1976).

[79] K.Schaetzl, J.Mod.Opt., **38**, 1849, (1991)

[80] C.Urban, *D*evelopment of Fiber Optic Based Dynamic Light scattering for a Characterization of Turbid Suspensions, Ph.D dissertation, (1999).

[81] R.G.Larson, *T*he structure and rheology of complex fluids, Oxford University Press, New York, USA, (1999).

[82] C.W.Macosko, *R*heology: Principles, measurements and pplications, Wiley-WCH, New York, USA, (1994).

[83] H. M. Wyss, K. Miyazaki, J. Mattsson et al, Phys. Rev. Lett., **98**, 238303, (2007).

[84] See *http://www.anton-paar.com/001/en/Web/Document/download/2760?clng=en* for additional information.

[85] A.Fernandez-Nieves, A.Fernandez-Barbero, B.Vincent et al, Macromolecules, **33**, 2114, (2000).

[86] J.F.Brady, G.Bossis, J.Fluid Mech., **155**, 105, (1985).

[87] P.B.Visscher, D.M.Heyes, J.Chem.Phys., **101**, 6096, (1994).

[88] B.J.Ackerson, P.N.Pusey, Phys. Rev. Lett., **61**, 1033, (1988).

[89] A. Einstein, Ann. Phys., **19**, 289, (1906).

[90] I.M.Krieger, T.J.Dougherty, Trans. Soc. Rheo., **3**, 137, (1959).

[91] H.A.Barnes, J.F.Hutton, K.Walters, *An Introduction to Rheology*, Elsevier, Amsterdam, Netherlands, (1989).

[92] A.Fernandez-Nieves, A.Fernandez-Barbero, B.Vincent et al, J.Chem.Phys., **119**, 10383, (2003).

[93] T.G.Mason, M.Y.Lin, Phys. Rev. E, **71**, 040801, (2005).

[94] B.M.Erwin, M.Cloitre, M.Gauthier et al, Soft Matter, **6**, 2825, (2010).

[95] In order to calculate n_{x-link}, we will use that the concentration of solids after the synthesis is $c_s = 1\%$ and the amount of cross-linker per total content of solid added in the system is $c_x = 0.2\%$. Thus, the ratio $\frac{c_s[solidweight/totalweight]\cdot c_x[x-linkerweight/solidweight]\cdot N_a}{M_{w,DVB}}$ will give the number density of cross-linker molecules if all the system were filled by particles, ζ=1. Since, in the synthesis conditions, the particles are fully deswollen we need to correct by a factor $\frac{V_{1p}}{V_{1p}^0}$ with V_{1p}^0 is the volume of the particle in the deswollen state and V_{1p} the volume of the particle in the swollen state, to account for the right ζ. Provided that $\frac{V_{1p}}{V_{1p}^0} \approx 125$, we obtain $n_{x-link} \approx 1.1 \cdot 10^{25}$ m^{-3}.

[96] S.L.Shenoy, W.D.Bates, H.L.Frisch et al, Polymer, **46**, 3372, (2005).

[97] R.Burtovyy, I.Luzinov, Langmuir, **24**, 5903, (2008).

[98] S.P.Obukhov, M.Rubinstein, R.H.Colby, Macromolecules, **27**, 3191, (1994).

[99] M.Rubinstein, R.Colby, A.V. Dobrynin et al, Macromolecules, **29**, 398, (1996).

[100] T.G.Mason, M.D.Lacasse, G.S.Grest et al, Phys. Rev. E, **56**, 3150, (1997).

[101] S.M.Hashmi, E.R.Dufresne, Soft Matter, **5**, 3682, (2009).

[102] P.A.Fitzgerald, D.Dupin, S.P.Armes et al., Soft Matter, **3**, 580, (2007).

[103] N.Raz, J.K.Li, L.K.Fidds et al., Macromolecules, **43**, 7277, (2010).

[104] H.M.Wyss, T.Franke, E.Mele et al., Soft Matter, **6**, 4550, (2010).

[105] X.Wu, R.H.Pelton, A.E.Hamielec et al, Colloid Polym. Sci. **272**, 467, (1994).

[106] C.Bonnet-Gonnet, L.Belloni, B.Cabane, Langmuir, **10**, 4012, (1994).

[107] H.Vink. Eur. Polym. J., **7**, 1411, (1971).

[108] D.M.Le Neveu, R.P.Rand, V.A.Parsegian, Nature, **259**, 601, (1976).

[109] C.E.Ioan, T.Aberle, W.Burchard, Macromolecules, **34**, 326, (2001).

[110] A. F. Routh, A.Fernandez-Nieves, M.Bradley et al., J. Phys. Chem. B **110**, 12721 (2006).

[111] C.P.Lindsey, G.D.Patterson, J. Chem. Phys., **73**, 3348, (1980).

[112] J.Bergenholtz, J.F.Brady, M.Vicic, J. Fluid. Mech., **456**, 239, (2002).

[113] For $\zeta < 1$, K is constant and it equals the values obtained in Fig.29. However, for $\zeta > 1$, we assume that the particle deswells isotropically and, thus, the deswelling takes places following the behavior observed in Fig.29. We perform a power-law fit, $\Pi_{ext} \sim V^{-\alpha}$, on the data in Fig.29 and obtain $\alpha_{0.5\%} = 2$ and $\alpha_{1.3\%} = 2.5$ respectively. Using Eq.45, we conclude that K$\sim V^{-\alpha}$ for $\zeta > 1$. Since $\zeta \approx 1/V$, we finally obtain K$\sim \zeta^{\alpha}$.

[114] A.Fernandez-Nieves, F.J. de las Nieves, A. Fernandez-Barbero, J.Chem. Phys., **120**, 374, (2004).

[115] R.H.Pelton, P.Chibante, Coll. Surf., **20**, 247, (1986).

[116] C.Nakamoto, T.Kitada, E.Kato, Polymer Gels and Networks, **4**, 17, (1996).

[117] E.Kato, J. Chem. Phys., **106**, 3792, (1997).

[118] E.Kato, J. Chem. Phys., **113**, 1310, (2000).

[119] C.Nakamoto, T.Motonaga, M.Shibayama et al,Macromolecules, **34**, 911, (2001).

[120] M.Shibayama, K.Isono, S.Okabe et al, Macromolecules, **37**, 2909, (2004).

[121] T.Lopez-Leon, A.Fernandez-Nieves, Phys. Rev. E, **75**, 011801, (2007).

[122] V.T.Pinkrah, A.E.Beezer, B.Chowdry et al, Langmuir, **20**, 8531, (2004).

[123] V.T.Pinkrah, A.E.Beezer, B.Z.Chowdrey et al, Coll. Surf. A, **262**, 76, (2005).

[124] V.Y.Grinberg, A.S.Dubovik, D.V. Kuznetsov et al, Macromolecules, **33**, 8685, (2000).

[125] M. Rubinstein, R. H. Colby, *Polymer Physics*, Oxford University Press, USA, 2003.

[126] M. Shibayama, T. Tanaka, *Volume Phase Transition and Related Phenomena in Polymer Gels in Responsive Gels, Volume Transitions I*, Advances in Polymer Science. Vol. 109 edited by K. Dusek, Springer Verlag, 1993.

[127] E. Kokufuta, *Transitions in Polyelectrolyte Gels in Physical Chemistry of Polyelectrolytes*, edited by T. Radeva , Taylor-Francis Ltd., 2001.

[128] M. W. Zemansky, R. H. Dittman, *Heat and Thermodynamics*, McGraw-Hill, 1996.

[129] W. C. D. Whetham, *Matter And Change*, Cambridge, United Kingdom, 1924.

[130] P.G.de Gennes, *Scaling Concepts in Polymer Physics*, Cornell Unviersity Press, 1991.

[131] P. J. Flory, J. Rehner, J. Chem. Phys., **11**, 512 (1943).

[132] P. J. Flory, J. Rehner, J. Chem. Phys., **11**, 521 (1943).

[133] J.W.Kim, A.S.Utada, A.Fernandez-Nieves et al, Angew.Chem.Int. Ed, **46**, 1819, (2007).

[134] G.Huang, Z.B.Hu, Macromolecules, **40**, 3749, (2007).

[135] J.Kohlbrecher, A.Bollhalder, R.Vavrin et al, Rev. Sci. Instr., **78**, 6, (2007).

[136] S.Cova, M.Ghioni, A.Lotito et al, J.Modern Opt.,**51**, 1267, (2004).

[137] B.Sierra-Martin, Y. Choi, M.S.Romero-Cano et al, Macromolecules, **38**, 10782, (2005).

[138] W.McPhee, K.C.Tam, R.J.Pelton, J. Colloid Interface Sci., **156**, 24, (1993).

[139] I.Varga, T.Gilanyi, R.Meszaros et al,J. Phys. Chem. B, **105**, 9071, (2001).

[140] S.Hirotsu, Phase Transitions, **47**, 125, (1994).

[141] M.G.Bulmer *Principles of Statistic* Dover Publications, New York, USA (1979).

[142] A.Fernandez-Barbero, A.Fernandez-Nieves, I.Grillo et al, Phys. Rev. E, **66**, 051803, (2002).

[143] S.Janssen, D.Schwahn, K. Mortensen et al, Macromolecules, **37**, 2909, (2004).

[144] M.Stieger, J.S.Pedersen, P.Linder et al, Langmuir, **20**, 7283, (2004).

[145] J.S.Higgins, H.C.Benoit, *Polymers and Neutron Scattering*, Oxford Science Publications, New York, USA (1996).

[146] R.A. Pethrick, J.V. Dawkins (Eds.), *Modern Techniques for Polymer Characterization*, John Wiley-Sons, New York (1999).

[147] R.K.Hobbie, American Journal of Physics, **40**, 857, (1962).

[148] S.Gasiorowicz, *Quantum Physics*, John Wiley-Sons, New York, (1974).

[149] M.R.Speigel, J.Liu, L.Abellanas, *Mathematical Handbook of Formulas and Tables*, McGraw Hill, (1999).

[150] E.Hecht, *Optics*, Addison Wesley, (2001).

[151] M.Shibayama, T.Tanaka, C.C.Han, J. Chem. Phys., **97**, 6829, (1992).

[152] In this conversion we neglect a term of the form $\bar{n}^2$, with $\bar{n}$ the average density on the sample. This term does not contribute to the structural features of the sample [145].

[153] G.L.Squires, *Introduction to the Theory of Thermal Neutron Scattering*, Dover Publications, London, (1997).

[154] M.R.Eskildsen, P.L.Gammel, E.D.Isaacs et al, Nature (London), **391**, 563, (1998).

[155] S.M.Choi,J.G.Barker, C.J.Glinjka et al, Appl. Crystallogr. **33**, 793, (2000).

[156] F.Ikkai, T.Suzuki, T.Karino et al, Macromolecules, **40**, 1140, (2007).

[157] K.Kratz, T.Hellweg and W.Eimer, Polymer, **42**, 6631, (2001).

[158] M.J.Snowden, B.Z.Chowdhry, B.Vincent et al, J. Chem. Society: Faraday Transactions, **92**, 5013, (1996).

[159] H.Kawasaki, S.Sasaki, H.J.Maeda, J.Phys. Chem. B, **101**, 4184, (1997).

[160] H.Kawasaki, S.Sasaki, H.J.Maeda, J.Phys. Chem. B, **101**, 5089, (1997).

[161] J.J.Lietor-Santos, B.Sierra-Martin, R.Vavrin et al, Macromolecules, **42**, 6225, (2009).

[162] M.Stieger, W.Richtering, J.S.Pedersen et al, J.Chem.Phys, **120**, 6197, (2004).

[163] J.S.Pedersen, C.Svanenborg, K.Almdal et al, Macromolecules, **36**, 416, (2003).

[164] V.N.Prabhu, M.Muthukumar, G.D.Wignall et al, Polymer, **42**, 8935, (2001).

[165] C.D.Jones, L.A.Lyon, Macromolecules, **33**, 8301, (2000).

[166] R.H.Pelton, Adv. Colloid Interface Sci., **85**, 1, (2000).

[167] H.M.Crowther, B.Vincent, Coll. Polym. Sci., **276**, 46, (1998).

[168] M.Rassmussen, A.F.Routh, B.Vincent, Langmuir, **20**, 3536, (2004).

[169] M.Andersson, S.L.Maunu, J Polym. Sci. Part B: Polym. Phys.,**44**, 3305, (2006)

[170] G.K.Batchelor, J. Fluid Mechanics, **83**, 97, (1997).

[171] J.F.Brady, M.Vicic, J.Rheol, **39**, 545, (1995).

[172] J.L.Harland, W. Van Megen, Phys. Rev. E, **55**, 3054, (1997).

[173] C.Kittel, *An Introduction to Solid State Physics*, John Wiley-Sons, New York, (2004).

[174] J.H.Chu, I.Lin, Physica A, **205**, 183, (1994).

[175] M.J.Stevens, M.L.Falk, M.O.Robbins, J.Chem.Phys., **104**, 5209, (1996).

[176] V. S. K. Balagurusamy, G. Ungar, V. Percec et al, J. Am. Chem. Soc., **119**, 1539 (1997).

[177] S. Hendricks and E. Teller, J. Chem. Phys., **10**, 147, (1942).

[178] P. N. Pusey, W. van Megen, P. Bartlett et al., Phys. Rev. Lett., **63**, 2753, (1989).

[179] C. Dewhurst, Meas. Sci. Technol. **19**, 1, (2008).

[180] M.S.Wertheim, Phys. Rev. Lett., **10**, 321, (1963).

[181] T.G.Mason, S.M.Graves, J.N.Wiling et al, J.Phys.Chem. B, **110**, 22097, (2006).

[182] F.Scheffold, T.G.Mason, J.Phys: Condensed Matter, **21**, 332102, (2009).

[183] D.Frenkel, J.Chem. Phys., **84**, 4625, (1986).

[184] M.Ginoza, M.Yasutomi, J. Phys. Soc. Japan, **68**, 2292, (1999).

[185] J.D.Debord, S.Eustis, S.B.Debord et al, Adv. Mat., **14**, 658, (2002).

[186] L.A. Lyon, J.D.Debord, S.B.Debord et al, J. Phys. Chem. B, **108**, 19099, (2004).

[187] K.N.Nordstrom, E.Verneuil, W.G.Ellenbroek et al., Phys.Rev.E, **82**, 041403, (2010).

VITA

The author of this thesis was born on 13th of August of 1980 in Madrid, Spain. He attended primary and high school in Granada, Spain and graduated in 1998. He obtained his B.Sc in Physics in the University of Granada in July, 2003 and collaborated with the Transient Electrodynamics group in the Applied Physics Department from 2001 to 2003. In September 2003, he started his doctoral studies under the supervision of Prof. Alberto Fernandez-Nieves. In September 2005 he obtained a M.Sc in the University of Granada in the program 'Science and Technology of Colloids and Interfaces' and later, on December 2005, he obtained another M.Sc in the program 'Applied Physics, Seismology and Renewable Energies' in the University of Almeria. He was a visiting student in the group of David A. Weitz in Harvard University in the period 2006-2007 and, in January 2008, he moved to the recently created 'Soft Condensed Matter Lab' in Georgia Institute of Technology to pursue a Ph.D degree. His research is always been focused on experimental soft condensed matter physics involving the study of these systems using imaging processing, microscopy, radiation scattering, electrophoresis and rheology and, has produced, so far, 8 publications in peer-reviewed journals and 10 contributed talks in international conferences and workshops.